

University of Nevada, Reno

**Design and Development of Climbing Robotic Systems for  
Automated Inspection of Steel Structures and Bridges**

A dissertation submitted in partial fulfillment of the  
requirements for the degree of Doctor of Philosophy in  
Computer Science and Engineering

by  
Son Thanh Nguyen

Hung Manh La/Dissertation Advisor

May 2023



THE GRADUATE SCHOOL

We recommend that the dissertation  
prepared under our supervision by

**SON THANH NGUYEN**

Entitled

**Design and Development of Climbing Robot Systems for Automated Inspection  
of Steel Structures and Bridges**

be accepted in partial fulfillment of the  
requirements for the degree of

DOCTOR OF PHILOSOPHY

Hung La, Ph. D., Advisor

Sushil Louis, Ph. D., Committee Member

Monica Nicolescu, Ph. D., Committee Member

Christos Papachristos, Ph. D., Committee Member

Mohamed A. Moustafa, Ph. D., Graduate School Representative

Markus Kimmelmeier, Ph. D., Dean, Graduate School

May 2023

# *Abstract*

by Son Thanh Nguyen

Steel structures are indispensable parts of modern civilization, with typical civil infrastructures including bridges, wind turbines, electric towers, oil rigs, ships, and submarines, all made of steel. These structures require frequent maintenance to ensure safety and longevity. Steel bridges are the most challenging architectures due to their complexity and height. Most inspections are conducted manually by professional human inspectors with special devices to inspect visible damages and defects on or inside these structures. However, this procedure is usually highly time-consuming, costly, and risky. Automated solutions are desired to address this problem. However, arduous engineering is delaying progress. A complete system needs to deal with three main problems: (1) locomotive performance for the high complexity of steel bridges, including differential curvatures, transitions between beams, and obstacles; (2) data collection capability, inclusive of visible and invisible damages, in-depth information such as vibration, coat, and material thickness, etc.; and (3) working conditions made up of gust winds.

To achieve such a complete system, this dissertation presents novel developments of inspection-climbing robots. Five different robot versions are designed to find the simplest and most effective configuration as well as control manner. Our approach started with (1) a transformable tank-like robot integrated with a haptic device and

two natural-inspired locomotions, (2) a roller chain-like robot, (3) a hybrid worming-mobile robot, (4) a multi-directional bicycle robot, and (5) an omni-directional climbing Robot, identified as the most potential solution for automated steel bridge inspection. For each robotic development, detailed mechanical analysis frameworks are presented. Both lab tests and field deployments of these robotic systems have been conducted to validate the proposed designs.

# *Acknowledgements*

I would like to express my gratitude towards my committee members, including Dr. Hung La, Dr. Sushil Louis, Dr. Monica Nicolescu, Dr. Christos Papachristos, and Dr. Mohamed A. Moustafa for their guidance and support throughout my research. Special thanks go to my supervisor, Dr. Hung La, for providing me with the opportunity and valuable advice to complete my research in the Advance Robotics and Automation Lab (ARA). I also acknowledge my lab-mates, Cadence Mosley, Anh Quyen Pham, and Chuong Le, for their help with the research. I am also grateful to my friends and family for their support during this time. Finally, special thanks go to Brian in the manufacturing lab for always being available to provide assistance.

This material is based in part upon work supported by: the U.S. National Science Foundation (NSF) under grants NSF-CAREER: 1846513 and NSF-PFI-TT: 1919127, and the U.S. Department of Transportation, Office of the Assistant Secretary for Research and Technology (USDOT/OST-R) under Grant No. 69A3551747126 through INSPIRE University Transportation Center.

# Contents

<b>Abstract</b>	<b>i</b>
<b>Acknowledgements</b>	<b>iii</b>
<b>List of Figures</b>	<b>vii</b>
<b>1 Introduction</b>	<b>1</b>
1.1 Motivation . . . . .	1
1.2 Previous Works . . . . .	5
1.3 Contribution . . . . .	9
1.4 Dissertation Organization . . . . .	12
<b>2 Transformable Tank-based Robot with A Haptic Device</b>	<b>13</b>
2.1 Overall Design . . . . .	14
2.2 Mechanical Design and Analysis . . . . .	18
2.2.1 Robot transformation kinematics . . . . .	22
2.2.2 Sliding Failure Investigation . . . . .	25
2.2.3 Turn-over Failure Investigation . . . . .	28
2.2.4 Magnetic Force Analysis on Curved Surfaces . . . . .	29
2.2.5 Motor Torque Analysis . . . . .	30
2.3 Robot Deployment . . . . .	33
2.3.1 Adhesive Force Measurement . . . . .	34
2.3.1.1 Static condition . . . . .	34
2.3.1.2 Dynamic condition . . . . .	35
2.3.2 Robot field deployment . . . . .	37
2.4 Conclusion . . . . .	44
<b>3 Roller Chain-like Robot</b>	<b>46</b>
3.1 Overall Design . . . . .	47
3.2 Magnetic Force Analysis . . . . .	49
3.3 Motor Torque Analysis . . . . .	52

3.4	Experiment results . . . . .	53
3.5	Conclusion . . . . .	56
<b>4</b>	<b>Hybrid Mobile-Worming Robot</b>	<b>57</b>
4.1	Overall Design . . . . .	58
4.2	Mechanical Design and Analysis . . . . .	62
4.2.1	Transformation Analysis . . . . .	63
4.2.2	Turn Over and Sliding Friction Analysis . . . . .	65
4.3	Robot Deployment . . . . .	68
4.4	Conclusion . . . . .	71
<b>5</b>	<b>Multi-directional Bicycle Robot</b>	<b>72</b>
5.1	Overall Design . . . . .	73
5.2	Mechanical Design and Analysis . . . . .	77
5.2.1	Robot Transformation Analysis . . . . .	77
5.2.1.1	Kinematic Analysis . . . . .	79
5.2.1.2	Force . . . . .	79
5.2.2	Robot Maneuverability Analysis . . . . .	80
5.2.2.1	Adhesive Force . . . . .	80
5.2.2.2	Extreme Locomotive Situations . . . . .	82
5.2.2.3	Steering . . . . .	83
5.2.2.4	Horizontal Traversing . . . . .	84
5.2.3	Sensor Deployment Mechanism Analysis . . . . .	85
5.2.3.1	ACE Analysis . . . . .	86
5.2.3.2	BDE Analysis . . . . .	87
5.2.3.3	Servo Crank Analysis . . . . .	87
5.2.4	Wheel Tire and Couplant Pumping . . . . .	89
5.2.4.1	Wheel Tire Design . . . . .	89
5.2.4.2	Couplant Pumping . . . . .	90
5.3	Magnetic Force Analysis . . . . .	90
5.3.1	Static condition . . . . .	91
5.3.2	Dynamic condition . . . . .	92
5.4	Robot Deployment . . . . .	94
5.4.1	Laboratory Tests . . . . .	94
5.4.2	Field Tests . . . . .	98
5.5	Conclusions . . . . .	102
<b>6</b>	<b>Onni-directional Climbing Robot</b>	<b>103</b>
6.1	Overall System . . . . .	104
6.2	Mechanical Design and Analysis . . . . .	106
6.2.1	Robot Maneuverability Analysis . . . . .	107

6.2.2	Ring System Analysis . . . . .	110
6.3	Magnetic Force Analysis . . . . .	115
6.4	Experimental Evaluation . . . . .	117
6.5	Conclusions . . . . .	121
<b>7</b>	<b>Conclusion &amp; Future Work</b>	<b>122</b>
7.1	Conclusion . . . . .	122
7.2	Future Work . . . . .	123
<b>8</b>	<b>Publication</b>	<b>125</b>
	<b>Bibliography</b>	<b>128</b>



# List of Figures

1.1	Typical steel structures: a) Sea-crossing steel bridges. b) Offshore oil rigs. c) Ship shells. d) Oil tanks and pipelines. (Source: Google images)	2
1.2	A collapsed section of the Interstate 5 bridge over the Skagit River is seen in an aerial view Friday, May 24, 2013, in Mt. Vernon, Wash. (Source: Google images)	3
1.3	Current practice of steel bridge inspection: rope certified bridge engineers inspecting the Golden Gate bridge, San Francisco, California, source: NBC April 2018. Detail available here: <a href="http://www.nbcbayarea.com/news/local/inspections-continue-at-golden-gate-bridge_bay-area/67243/">www.nbcbayarea.com/news/local/inspections-continue-at-golden-gate-bridge_bay-area/67243/</a>	4
1.4	Robots utilize air pressure as an adhesive force to climb on structures.	6
1.5	Robots use suction with vacuum force to adhere to surfaces.	7
1.6	Robots make use of friction to climb on cylindrical objects.	7
1.7	Elios 2, a commercial drone for visual inspection.	8
1.8	(Left) Skydio 2 with auto exploring function for structures inspection. (Right) Development of this drone for a bridge inspection	8
1.9	Overall approach for steel bridge inspection robots.	9
1.10	The notable steel structure climbing robots.	10
2.1	Steel climbing robotic system. (Left) a simulated robotic arm on the ground station for remote control. (Middle) the side view of the robot. (Right) the front view of the robot. The robot is equipped with both camera and an Eddy current sensor for visual and non-destructive evaluation of the steel structure.	14
2.2	System interface: Operator controls robot remotely from the ground station via radio links. Xbee modules manage to send robot locomotion commands and receive data from the sensor. A 5-DOF manipulator holding Eddy current sensor's probe is controlled by a haptic device while a keypad handles robot movement. Visual and sensor data are live on a PC screen.	15

2.3	Roller chain with integrated Hall sensor and IR distance sensors. The IR sensor is served as feedback of the PID control to regulate the reciprocating mechanism automatically on different contour surfaces. The detail of the PID control function is described in Subsection 2.2.1 and Figure. 2.11. . . . .	16
2.4	(Left) Industrial Eddy current sensor Nortec 600; (Right) sensor probe for data collection. . . . .	17
2.5	a) kinematic structure of 5-DOF arm; b) executive arm integrating on the robot; c) controlling arm for user operation in manual mode. . . .	17
2.6	Reciprocating mechanism for robot transformation and specifications of the robot's design (unit in mm). . . . .	19
2.7	Pull force over air gap of $10mm \times 10mm$ magnet cylinder. . . . .	21
2.8	Reciprocating mechanism for robot transformation on different surfaces: flat, negative curve, and positive curve. . . . .	22
2.9	Reciprocating mechanism: $a = 33.7mm$ , $XY = 32mm$ , and $\gamma = degree$ . . . . .	23
2.10	Kinematics of the robot transforming mechanism: $b = 72mm$ , $b_1 = 45mm$ , $f = 11mm$ , and $e = 55mm$ . . . . .	24
2.11	Examples of different cases when the robot moves from flat to curved steel surface: (Left) positively curved surface; (Right) negative curved surface. A PID controller will be activated to keep the distance of two sensors D1 and D2 equally. . . . .	25
2.12	a) Sliding failure; b) Turn-over failure; (c) Moment calculation at point $O$ . . . . .	26
2.13	a) Climbing on top inclined surface; b) Climbing underneath inclined surface. . . . .	26
2.14	a) Robot moves on top of inclined surface; b) Robot moves on bottom of inclined surface. . . . .	31
2.15	Transformation mechanism with 7 joints to create climbing flexibility of the robot. . . . .	32
2.16	Experimental setup for magnetic force measurement. . . . .	35
2.17	Magnetic force measurements on coated and non-coated flat steel surface. . . . .	35
2.18	Magnetic force measurements on a curved steel surface with diameters (D) ranging from $100mm$ to $900mm$ . . . . .	36
2.19	Adhesive force measurement in dynamic condition on a non-coated flat surface (robot moves from right to left images) . . . . .	36
2.20	(Left) testing result on flat surfaces, (right) testing result on coated curving surfaces (cylinder tubes) . . . . .	37
2.21	Adhesive and climbing test on a thick paint-coated steel structure: flat surface. . . . .	38
2.22	Adhesive and climbing test on a thin paint-coated steel structure: cylinder shape $D=100mm$ . . . . .	38

2.23	Adhesive and climbing test on a thin paint-coated steel structure: cylinder shapes $D=250\text{mm}$ . . . . .	39
2.24	Adhesive and climbing test on a thick paint-coated steel bridge: a flat surface. . . . .	39
2.25	Adhesive and climbing test on a rusty paint-coated steel bridge: flat structure with bolts/nuts. . . . .	39
2.26	Images stitching result: (Top) 7 individual images taken by the robot climbing on a bridge in Figure 2.25; (Middle) Stitching image result from those 7 individual images; (Bottom) Closer look (zoom-in) at some areas, which has a serious rusty condition with holes on the surface.	40
2.27	Crack surveying process. Visual data is acquired by camera 1 (top-right image). The operator controls Eddy current sensor's probe remotely by a haptic system (control arm: bottom-left image) with a closer view from camera 2 (bottom-right image). Eddy current sensor measures the depth of crack (top-left image), more detail in Fig. 2.28 . . . . .	41
2.28	a) Probe path; b) line 4 data; c) line 3 data; d) line 2 data; e) line 1 data. . . . .	42
2.29	a) Image of an inspected area with cracks on it; b) Fatigue crack map from Eddy current sensor showing defect areas with red/yellow color, corresponding well with the crack areas on the image. . . . .	43
3.1	Overall design of a robot for steel bridge inspection tasks. . . . .	47
3.2	Robot kinematics. . . . .	47
3.3	Robot turns left. . . . .	48
3.4	Magnet states before approaching steel surfaces. . . . .	49
3.5	Robot's locomotion on different surface curvatures.(a) Robot is on flat surface.(b) Robot transfers between two surfaces.(c) Robot transfers to another surface with obstacle.(d) Robot moves on curving surface.(e) Robot moves on cylindrical surface.(f) Robot moves on circumferential direction of cylindrical object . . . . .	50
3.6	a) Robot attaches vertically to surface; b) Robot attaches horizontally to surface. . . . .	51
3.7	Robot shape in limitations a) $h$ max; b) $h$ min. . . . .	51
3.8	Magnet block position analysis. . . . .	52
3.9	Magnet block position analysis. . . . .	53
3.10	Adhesion force on flat surfaces. . . . .	54
3.11	Adhesion force on curving surfaces with different radius. . . . .	54
3.12	Robot test on an I-shape beam. . . . .	55
3.13	Robot test on a cylindrical beam. . . . .	55
3.14	Robot test on a curved surface. . . . .	56
4.1	Overall design of robot. . . . .	58

4.2	Robot function (a) Mobile mode; (b) Transforming mode, or worm mode.	59
4.3	The robots foot with flexible magnet array. . . . .	60
4.4	(a) The robot on flat surface; (b) The robot passing nuts; (c) The robot on a curving surface. . . . .	61
4.5	The robot body - 6 DOF robot arm. . . . .	61
4.6	Transformation process: (a) The robot in mobile mode; (b) The robot makes the magnet array touch on the 1st foot and looks for new a new surface with the other; (c) The 2nd foot touches a new surface and moves the rest of the robot there; (d) The robot switches back to mobile mode on the new surface. . . . .	62
4.7	Extended statics diagram. . . . .	63
4.8	Turn over/adhesion diagram. . . . .	66
4.9	The robot tests on a steel structure indoors. . . . .	69
4.10	Deployment of the robot on a steel structure. . . . .	70
4.11	Mobile mode example on bridge. . . . .	70
5.1	(Left) The front and back view of the robot. (Right) The 3D design model of the robot. . . . .	74
5.2	The design concept shows the maneuverability of our robot with active joints colored green (for the front joint) and blue (for the rear joint). Two independent steering actuators allow the robot to enable bicycle-like moving modes (a) when only the front steering unit is activated and (b) when only the rear steering unit is activated to change direction on narrow surfaces. (c) Two steering units are activated simultaneously; the robot can move sideways. (d) The mix of bicycle and multi-directional modes. On horizontal traversing, the bicycle shape is weak in maintaining adhesive torque. This mode improves this disadvantage with wheel paralleling configuration but is still able to turn. . . . .	75
5.3	The free joint (orange) in the middle of the robot's body helps its wheels to better adhere to uneven surfaces, e.g., a) two flat curvatures, b) positive curvatures, c) negative curvatures. . . . .	76
5.4	Our design allows the distance between the two wheels to be adjustable with two revolute joints. The robot can pass corners without activating the two joints in normal conditions (a), and (b). However, the robot can adjust the wheels' distance (the two joints are activated, hence colored purple) to be small to pass a thin edge (c) or big to pass an acute corner (d). . . . .	76
5.5	Robot configuration when traveling in an extreme situation (horizontal traverse on a cylindrical structure). a) the robot in high risk of losing adhesive force in normal bicycle mode, b) the robot is in fourth mode Figure 5.2d that significantly improves adhesive torque to keep the robot safe in this situation. . . . .	77

5.6	The robot's shape when applying reciprocating mechanisms. a) in normal conditions, b) when passing thin edges, and c) when passing acute internal corners. The sensor and deploying mechanism position do not affect to transforming function. It also enables the sensor always be perpendicular to measuring surfaces even if they are curved. . . .	78
5.7	The reciprocating mechanism's kinematic. . . . .	78
5.8	Force analysis of the reciprocating mechanism. . . . .	80
5.9	A situation where the adhesive force is minimal, resulting in a high chance of falling over. In this case, the adhesive force of the front wheel is significantly reduced when the robot hits an edge. . . . .	81
5.10	When the robot passes an internal corner between two perpendicular surfaces, the robot's load increases significantly. . . . .	83
5.11	An experiment is conducted to investigate the load on a steering servo motor. A dynamo meter is mounted on one wheel's edge (point $L$ ) to measure the load. The distance from $L$ to the rotating point $X_2$ is $r$ (the wheel's radius). a) Side view. b) Top view. . . . .	83
5.12	a) robot shape is in conventional bicycle mode b) robot transforms into the mixed mode to improve safety factor in extreme situations . . . .	84
5.13	The four-bar mechanism. A flexible part (TPU) acts as a soft contact between the probe and surfaces. An angle lock is added to create a range of free movement of the probe when approaching uneven surfaces.	85
5.14	The four-bar mechanism's kinematic. . . . .	86
5.15	The kinematic of the four-bar mechanism (AGHK) with HK is the servo arm. . . . .	87
5.16	The design of rubber tires. a) One strip tire, b) Two separated strips tire. . . . .	88
5.17	High viscosity couplant is stored in a syringe tank. A mini peristaltic pump with a silicone tube is utilized to release the couplant. . . . .	89
5.18	a) The test on a flat 4cm thick surface b) The test on a 10 cm diameter tube with 5mm thickness. Several tests on cylindrical structures were also conducted with diameters ranging from 20cm to 90 cm c) the test on a 90-degree internal corner, when the wheel bears additional force from a transiting surface d) The test on an edge of an external corner.	91
5.19	Adhesive forces measurements of a non-coated magnetic wheel on steel surfaces. . . . .	92
5.20	a) Magnetic force measurement in an internal corner b) Magnetic force measurement in an external corner . . . . .	93
5.21	Experimental setup for magnetic force measurement when robot moving.	93
5.22	Robot passes 90 degrees internal and external corners. . . . .	95
5.23	The robot travels along a rectangular structure. The robot gets sliding failure when transiting to another surface. By switching to multi-directional mode, the robot overcomes this situation easily. . . . .	95

5.24	Thanks to free joint Figure. 5.3 makes the robot body flexible. Wheels fully adhere to any surface curvatures. Robot locomotion tests on a cylindrical structure. . . . .	95
5.25	A 20mm-thick steel plate is used for the thin edge test. The robot's wheel distance (RWD) is 40mm in normal conditions. The transforming mechanism is activated to allow RWD as close as 15mm. So, the robot now can pass the edge. . . . .	96
5.26	A 60-degree acute corner is shown in this test. Because of the robot's shape, the front wheel cannot hit the acute corner in normal conditions. The transforming mechanism controls RWD as big as 100mm which enables the front wheel can touch the second surface of the acute corner to smoothly overcome it. . . . .	96
5.27	A complex structure setup for indoor experiments. It includes cylindrical, I-shape, U-shape, and rectangular steel frames. The robot can travel to almost any location except for discontinuous transitions and narrow spaces for robot size. . . . .	97
5.28	A demonstration of measuring the thickness of a steel surface. The couplant nozzle is controllable to move up and down. First, the nozzle is adjusted to fully touch the surface to make sure the gel/couplant will stick well without falling off in cases: a) the robot is vertical and b) upside down. Second, the gel is pumped 0.4 milliliters. Next, the nozzle moves up 0.5 cm to give space for the transducer. The transducer deploys 3 times to get an average value. If measurements are not good by giving N/A, the gel is added more to improve the contact with the surface. . . . .	98
5.29	The tests are on (a) a square tube structure and (b) a cylindrical structure. The robot travels and stops to collect thickness data in interesting areas. Robot positions and data are matched and monitored in real time in a 3D environment. The robot path represents in white color. Steel thickness measuring positions are red dots. Thickness data (numbers in green color) is shown in inch units. . . . .	99
5.30	The robot operates on a cylindrical steel bridge on the campus of the University of Nevada, Reno. . . . .	100
5.31	Robot deployment on a bridge on Highway-80 located in Lovelock city, NV, USA. The robot traverses upside down on the main I-shape beam; the Robot passes an edge of the I-shape beam; the Robot moves upside down on a T-shape member, and the robot travels stably on a bridge water draining tube. . . . .	100
5.32	Robot smoothly traverses an edge of I-shape beam on the deployment on Highway-80 . . . . .	101

5.33	Robot deployment and data collection on a bridge on Highway I-75 in Georgia, USA. Robot positions and steel thickness data are synchronized in real-time. The robot path represents in white color. Steel thickness measuring positions are red dots. Thickness data (numbers in green color) is shown in inch units. . . . .	101
6.1	3D model of the robot. There are four magnetic wheels driven by four moving motors. The flexibility of omnidirectional function is by four independent steering units. The robot body is flexible to fully adhere to any surface by an agile-free joint that links two halves of the robot body. The ring system for sensor/module deployment is placed in the middle of the robot body. This position is ideal for deployment on any surface even curved contours. This also protects sensors/modules and is in conflict with locomotion functions. The robot is equipped with an onboard computer and a 3D camera for visual defect detection and mapping. The ultrasonic sensor is integrated for physical exams to measure material and coat thicknesses. . . . .	105
6.2	Robot is named Cab. It is 9 kg weight and an additional 2 kg load. Robots can provide both visual and physical inspections with available space sensors. In this design, the robot is integrated ultrasonic sensor module to measure the material thickness and gel pumping mechanism.	106
6.3	The advanced locomotion performance of the robot is illustrated. a) and c) the robot is in mode 1. It navigates in Ackerman configuration on simple contours or passing internal corners. b) Mode 2, when the robot needs to spin around, steering units change their shape to allow this motion, it is useful in limited space. d) In mode 3, when passing obstacles such as thin edges (reinforce bar of structures) robot heading transforms 90 degrees compared to mode 1. front and back wheels are close together with an 8mm distance. . . . .	107
6.4	When the robot is spinning in place, the instantaneous center of rotation (ICR) is located at the center of the robot's body. . . . .	109
6.5	When the robot is in mode 3 and passes a 10mm edge, it experiences the minimum attractive force to the steel structure. . . . .	110
6.6	The Ring mechanism is a hybrid planetary gear system that is specifically designed for selecting sensors/modules and deploying them. . .	111
6.7	The symmetrically reciprocating mechanism kinematic. . . . .	112
6.8	The center gears of the Ring mechanism, Gear 1 and 2, are placed on opposite sides and are driven by two actuators. The next round of gears consists of six Moon gears, named M1, M2, M3 on one side, and M4, M5, M6 on the other side. The Moon gears on each side rotate in the same direction. The Moon gears are connected to planetary gears or arms named P1 to P6. The P1-2, P3-4, and P5-6 gear pairs control the deployment of sensors or modules. . . . .	113

6.9	When Gear 1 and Gear 2 are rotating in the same direction, the whole Ring mechanism will rotate and allow for the selection of which module/sensor to deploy. In this design, three options are provided, as shown in Figure 6.9. . . . .	113
6.10	When gears 1 and 2 spin in opposite directions to each other, their moon gears M1, M2, and M3 rotate in one direction while M4, M5, and M6 rotate in the opposite direction. Planetary gear pairs P1-2, P3-4, and P5-6 act as reciprocating links to control the positions of the module/sensor for deployment or standby. To achieve soft contact with the surface, the sub-links are made with elastic materials, as shown in Figure 6.6. . . . .	114
6.11	Magnetic force measurement in different working conditions. a) flat surface b) external corner c) internal corner . . . . .	116
6.12	a) Magnetic force measurement in a flat surface b) Magnetic force measurement in a 90cm diameter curved surface c) Magnetic force measurement in an internal corner d) Magnetic force measurement in an external corner . . . . .	117
6.13	Robot locomotion, a) b) Mode 1: Robot mobility is Ackerman (car-like) mechanism. c) Mode 2: The robot turns around the spot. It is useful to change direction in a narrow space. d) Mode 3: The robot changes its head to move sideways. In this mode, the front and back wheels' distance is close to 8mm which function to pass obstacles and thin edges. . . . .	118
6.14	Robot traverses on mode 1. . . . .	118
6.15	Robot does side-way movement in mode 3. . . . .	119
6.16	Ring system operation to measure material thickness. a) Gel pumping is deployed to enhance contact between the transducer and the surface. b) Ultrasonic transducer is deployed. . . . .	120



# Chapter 1

## Introduction

### 1.1 Motivation

Steel structures, including bridges, wind turbines, electric towers, oil-related constructions, ships, submarines, etc are integral to modern civilization. Maintenance of these structures is essential to ensure their safety and longevity. However, the majority of maintenance tasks are still performed manually by humans, which is a costly and high-risk process. For example, inspectors must climb up and hang on cables to inspect remote areas of bridges (Fig. 1.1a) or offshore oil rigs (Fig. 1.1b), which can be extremely hazardous. Even the inspection of less complicated structures such as wind turbines, ship shells (Fig. 1.1c), and gas/oil tanks/piles (Fig. 1.1d) is a significant challenge due to their large scales.

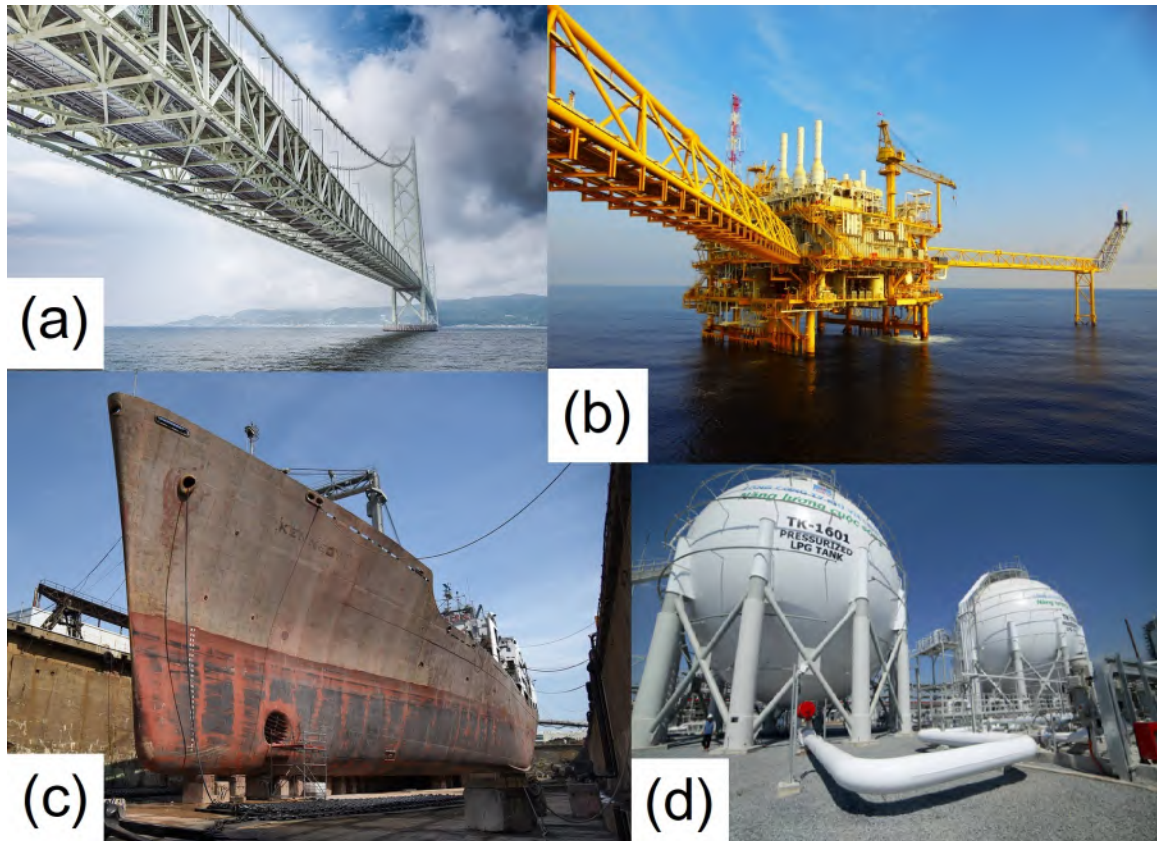


FIGURE 1.1: Typical steel structures: a) Sea-crossing steel bridges. b) Offshore oil rigs. c) Ship shells. d) Oil tanks and pipelines. (Source: Google images)

Steel bridges are among the most complex structures, and as such, their inspection and maintenance pose significant challenges. In the United States alone, nearly one-third of the 607,380 bridges are steel bridges, according to the Federal Highway Administration [1]. The National Bridge Inventory (NBI) [1] further reveals that 25 percents of these steel bridges are either deficient or functionally obsolete, indicating a growing threat to transportation safety. Recent bridge collapses, such as the I-5 Skagit River Bridge collapse in 2013 [2] (Fig. 1.2), underscore the need for more frequent inspections.

The growing number of bridge collapses has had a significant impact on the safety of



FIGURE 1.2: A collapsed section of the Interstate 5 bridge over the Skagit River is seen in an aerial view Friday, May 24, 2013, in Mt. Vernon, Wash. (Source: Google images)

travelers. The current inspection practices for these bridges mainly involve visual and manual evaluations. Often, inspectors have to climb up and hang on cables to inspect the nearly inaccessible structures of bridges [3]. They physically review the status of each steel member by tapping a hammer on the steel to collect impact echo waves for fatigue crack inspection [4], or visually look at all surfaces of the steel members to detect shallow surface cracks. For example, the Golden Gate Bridge, a landmark of the Bay Area in San Francisco, California, is manually inspected by a team of 12 rope-certified bridge engineers [3], who have to climb and hang on the high steel structures

to perform inspections. These jobs tend to be very time-consuming and dangerous, resulting in a shortage of people willing and capable of doing them. This shortage in supply means that the demand for adequate inspection and maintenance of these bridges is not being met [1, 5]. Therefore, there is a societal need for alternative solutions because the current methods are not able to satisfy the growing demand for safe, cost-effective, and accurate inspection. Automated solutions are desired to address this problem. However, arduous engineering is delaying our progress.



FIGURE 1.3: Current practice of steel bridge inspection: rope certified bridge engineers inspecting the Golden Gate bridge, San Francisco, California, source: NBC April 2018. Detail available here: [www.nbcbayarea.com/news/local/inspections-continue-at-golden-gate-bridge\\_bay-area/67243/](http://www.nbcbayarea.com/news/local/inspections-continue-at-golden-gate-bridge_bay-area/67243/)

This dissertation desires to address the problem through two main approaches: first, creating novel robotic locomotion from natural inspiration; second, analyzing robotic



systems applied for infrastructures with simple curvatures then combining advantages of single robot type or improving them.

## 1.2 Previous Works

As an effort to automate the inspection process, there has been a variety of implementations of climbing robots for inspection [6–14]. A notable development of steel climbing robots is summarized in Figure 1.10.

A roller chain, integrated permanent magnet robot was reported in [15]. A legged robot that can transition across structure members for steel bridge inspection was developed [16]. The robot uses permanent magnets integrated with each foot to allow it to hang from a steel bar. In another case, a magnetic wheeled robot, which can carry magneto resistive sensor array for detecting corrosion and cracks, was developed [17]. Similarly, several climbing permanent magnet-robots [18–26] were designed to carry non-destructive evaluation (NDE) devices to detect corrosion, weld defects, and cracks, and these robots can be applied for inspecting steel structures and bridges. Other efforts have been shown for the development of climbing robots for power plant inspection [27] and bridge cable inspection [28].

Additionally, significant development of climbing robots for steel structure and bridge inspection has been reported in [9, 29–41]. Furthermore, with industry involvement, a surface adapting tank-like robot with untouched permanent magnet mechanism was

developed by Inuktun company for steel structure inspection using the camera for visual observation [42].

In addition to using permanent magnets, the electromagnet was also used to develop a climbing robot. For instance, electromagnet was embedded in a spider robot's legs [43] to utilize the climbing ability of the creature on complex structures.

Apart from steel bridge inspection, the great effort for automating concrete bridge deck inspection and evaluation has been reported in [44–65]. The leading work in the automated concrete bridge deck inspection is the Robotics Assisted Bridge Inspection Tool (RABIT<sup>TM</sup>), which was developed by the Rutgers University's Center for Advanced Infrastructure and Transportation. RABIT was integrated with multiple NDE sensors including ground penetrating radar, electrical resistivity, impact echo, ultra surface wave, and high-resolution cameras [45, 66? –70]. RABIT can move autonomously on the bridge deck to collect visual and NDE data by using the Extended Kalman Filter (EKF)-based localization and the artificial potential field-based motion planning [48, 71]. Other significant robotic developments for bridge deck inspection and evaluation can be found in [72–77].



FIGURE 1.4: Robots utilize air pressure as an adhesive force to climb on structures.

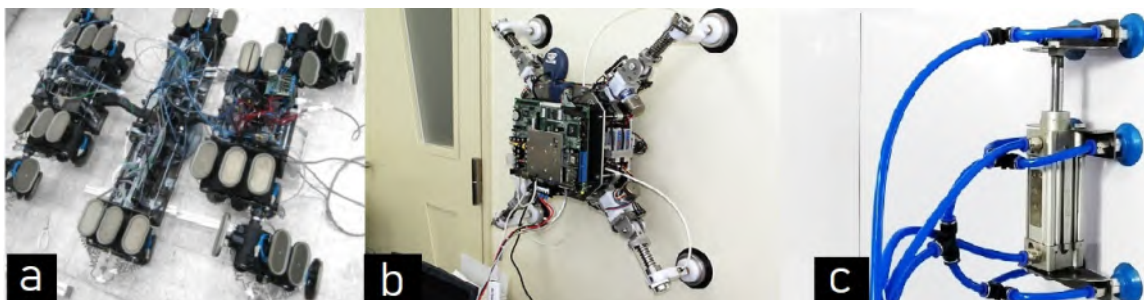


FIGURE 1.5: Robots use suction with vacuum force to adhere to surfaces.

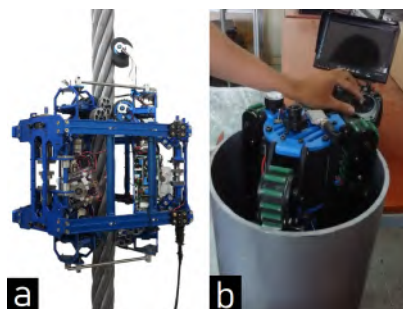


FIGURE 1.6: Robots make use of friction to climb on cylindrical objects.

Imitation of mobility of climbing creatures is another approach. A spider-like robot with electromagnets on its feet was reported [78], and a legged robot was developed [16]. An inchworm-like robot [35] was an efficient design and creative, which has been tested on the Sydney bridge, Australia. This robot excels in its ability to transfer smoothly  $360^\circ$  to other surfaces. It is equipped with a camera and a lidar for structure 3D mapping.

Aerial robots, with no constraints in terms of structural geometry for locomotion, provide a great means for visual inspection tasks, especially with the cutting-edge image processing technology available today. Various research in this area has been conducted, with some of the latest developments making drone control significantly safer even in confined spaces [79–81]. One innovation created a quadcopter design



FIGURE 1.7: Elios 2, a commercial drone for visual inspection.

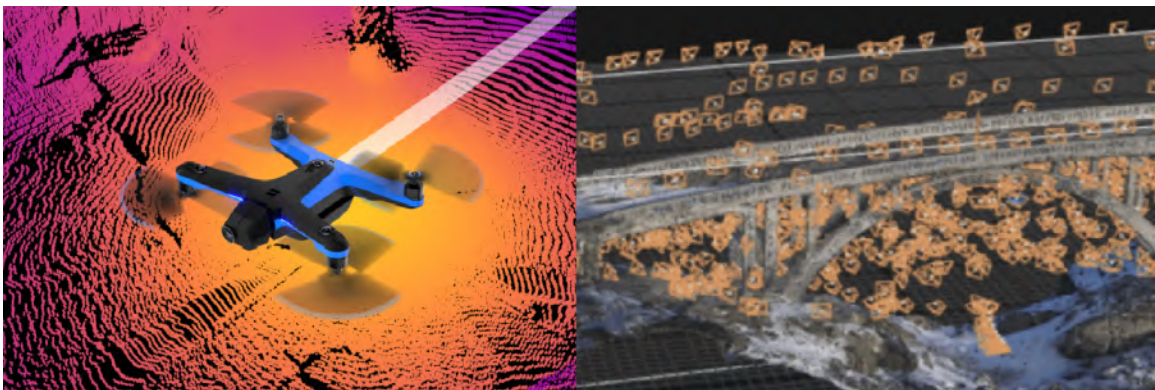


FIGURE 1.8: (Left) Skydio 2 with auto exploring function for structures inspection.  
(Right) Development of this drone for a bridge inspection

with a clip that can hold onto a bridge's beams to stay stationary during inspections without wasting flying energy [82]. The existing structural inspection methods are described on a chart in Fig. 1.9.

In summary, current approaches for bridge inspection have several disadvantages. Mobile robots are limited to simple curvatures and have limited climbing ability. Limbed robots have potential, but require significant control development before they become feasible. Drones are a good option because they do not face locomotive issues like mobile robots, but gusty winds can be a stability problem for outdoor and



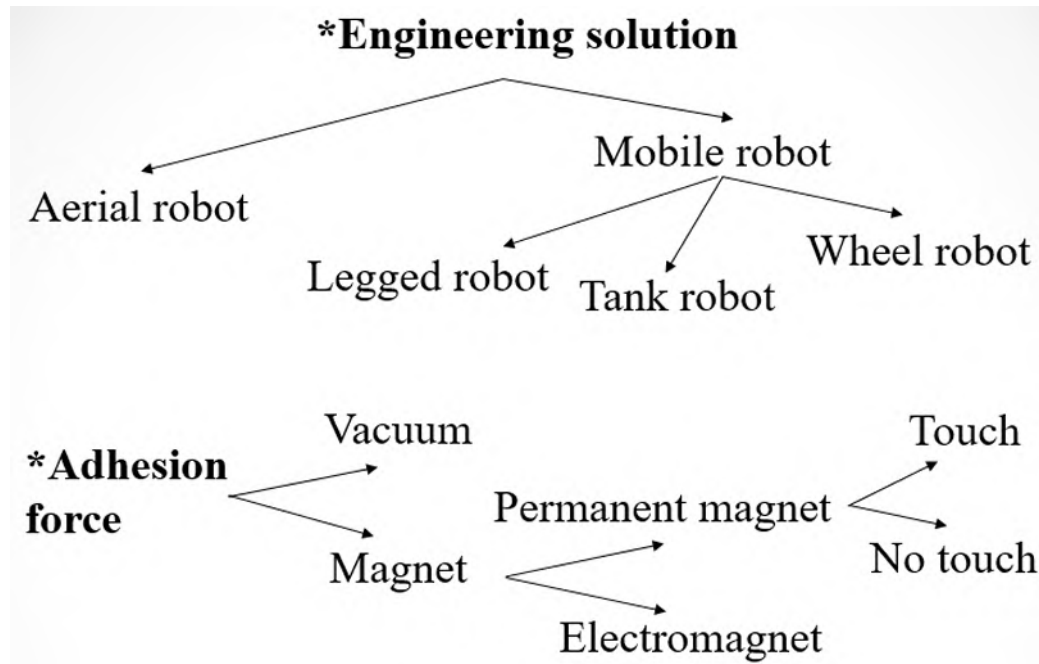


FIGURE 1.9: Overall approach for steel bridge inspection robots.

high constructions such as bridges. Additionally, integrating multiple sensing devices presents a challenge for load and design. There have been proposals for hybrid flying-mobile robots, but designing a whole new system is a significant engineering challenge.

### 1.3 Contribution

This dissertation presents the development of several generations of climbing robots aimed at finding an optimal, simple, and feasible engineering solution for inspecting complex steel structures and bridges.

The proposed approach was guided by three important boundary conditions: dealing with gust wind, handling the high complexity of steel structures, and ensuring data







Robot	Type of Locomotion	Detail	Climbing Ability		Adhesion Method	
Mecanum-wheel Robot [Kamdar2015]	4-mecanum wheels	681 × 559 × 323 mm 34 kg 0.64 m/min	Flat Concave Convex Cylinder	x  x	Permanent Magnet (untouched)	
	Tank-like Robot [Versatrax100-Inuktun]	2 roller chains	376 x 220 x 115 mm 4.5 kg 0.15 m/s	Flat Concave Convex Cylinder	x x	Permanent Magnet (untouched)
	4-Wheels robot [Wang_ICA2014]	4 magnetic wheels (flexible frame) 3 kg 0.32 m/s	352 × 215 × 155 mm	Flat Concave Convex Cylinder	x x x	Permanent Magnet
	2-Wheels robot [Eich_MED2015]	2 magnetic wheels 380 x 280 x 150 mm 0,67 kg 0.5 m/s	Flat Concave Convex Cylinder	x x x	Permanent Magnet	
	Inch-worm robot [Ward2016]	7-DOF-Inch worm 220 x 240 x 150 mm 18 kg 0.2 m/s	Flat Concave Convex Cylinder	x	Permanent Magnet	
	Spider robot [Genki Sato2017]	6 limbs-spider 600 x 600 x 250 mm 12 kg 0.2 m/min	Flat Concave Convex Cylinder	x	Electromagnet	
						

FIGURE 1.10: The notable steel structure climbing robots.

collection capability.

The development process involved the following robots:

1. Transformable tank-like robot with a haptic-based manipulator 2. Roller chain-like robot 3. Hybrid worming-mobile robot 4. Multi-directional bicycle robot 5. Omni-directional Climbing Robot, identified as the most potential solution for automated steel bridge inspection. The contributions of this dissertation are summarized as follows:

- Novel design and development of a transformable tank-like robot with an integrated haptic-based manipulator
- Mechanical analysis framework of the transformable tank-like robot
- Lab test and field deployment of the transformable tank-like robot
- Novel design and development of a roller chain-like robot
- Kinematic and mechanical analysis framework of the roller chain-like robot
- Lab test and field deployment of the roller chain-like robot
- Novel design and development of a hybrid worming-mobile robot
- Mechanical analysis framework of the hybrid worming-mobile robot
- Lab test and field deployment of the hybrid worming-mobile robot
- Novel design and development of a multi-directional bicycle robot
- Mechanical analysis framework of the multi-directional bicycle robot
- Lab test and field deployment of the multi-directional bicycle robot
- Novel design and development of the Omni-directional Climbing Robot
- Mechanical analysis framework of the Omni-directional Climbing Robot
- Lab test and field deployment of the Omni-directional Climbing Robot

Through both lab tests

and field deployments, the proposed robots were shown to perform well under different conditions, validating the intended designs and verifying mechanical analysis.

## **1.4 Dissertation Organization**

The organization of the remainder of this dissertation is as follows. In Chapter 2, a transformable tank-line robot integrated with a haptic device is introduced. Chapter 3 goes over the roller chain-like robot. Chapter 4 details the hybrid worming-mobile robot. Chapter 5 presents the multi-directional bicycle robot. Chapter 6 details the most potential solution for steel structures inspection, the Onmi-directional Climbing Robot. Lastly, Chapter 7 covers the conclusion and future development.

## Chapter 2

# Transformable Tank-based Robot with A Haptic Device

This chapter presents a practical climbing robotic system to provide an efficient solution for steel bridge inspection. The robot can adapt to a wide range of different types of bridge surfaces (flat, curving, rough) and carry sufficient measurement devices including cameras and an Eddy current sensor. The proposed small tank-like robot with a reciprocating mechanism features various deformable 3D configurations, which can allow it to transition among steel structure members for efficient inspection. The robot utilizing adhesive force generated by permanent magnets is able to adhere well to steel structures while moving. The roller-chain design allows the robot to overcome obstacles including nuts, bolts, and convex and concave corners. To demonstrate the robot's working principle, it has been deployed for climbing

on more than 20 steel bridges. Video of this deployment can be seen in this link:  
[https://ara.cse.unr.edu/?page\\_id=11](https://ara.cse.unr.edu/?page_id=11)

## 2.1 Overall Design

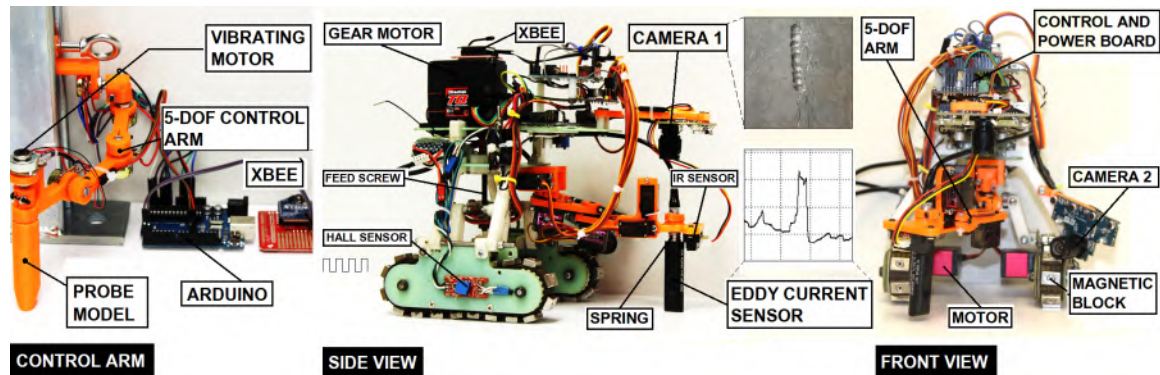


FIGURE 2.1: Steel climbing robotic system. (Left) a simulated robotic arm on the ground station for remote control. (Middle) the side view of the robot. (Right) the front view of the robot. The robot is equipped with both camera and an Eddy current sensor for visual and non-destructive evaluation of the steel structure.

The overall design concept of a tank-like climbing robot is shown in Figure 2.2 and the implementation of this design is shown in Figure 2.1. The roller chains embedded with permanent magnets for adhesive force creation enable the robot to adhere to steel surfaces without consuming any power. The control architecture of the robot consists of low-level and high-level controllers. The low-level controller handles tasks including (i) converting velocity and heading commands from the high-level controller to Pulse Width Modulation (PWM) data to drive motors, and (ii) reading data from multiple sensors for navigation purposes. The high-level controller is embedded in an onboard computer to enable data processing and ground station communication.

Both controllers fuse sensor data to provide desired linear velocity and heading for the robot and acquire data from advanced sensors. Furthermore, the high-level controller sends data wirelessly to a ground station for processing and logging.

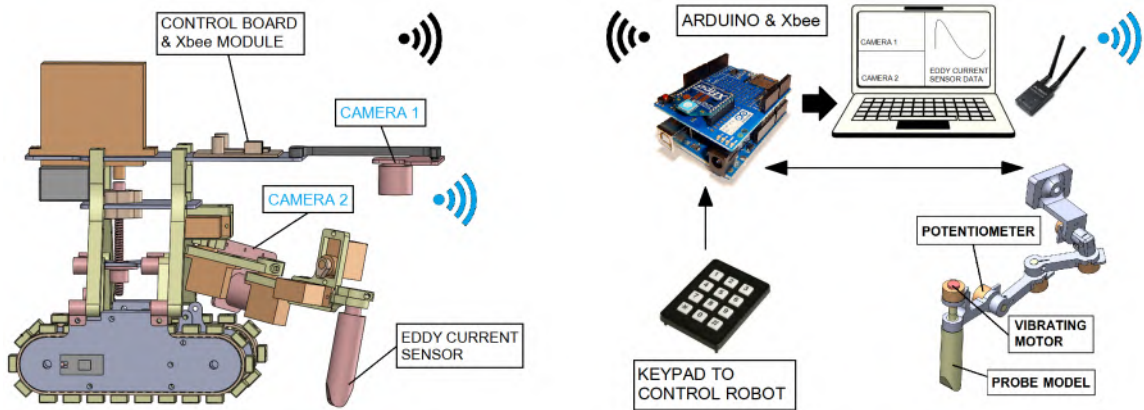


FIGURE 2.2: System interface: Operator controls robot remotely from the ground station via radio links. Xbee modules manage to send robot locomotion commands and receive data from the sensor. A 5-DOF manipulator holding Eddy current sensor's probe is controlled by a haptic device while a keypad handles robot movement. Visual and sensor data are live on a PC screen.

The robot is equipped with various sensors for navigation as well as steel structure evaluation. There are two video cameras: one for capturing images of inspected surfaces, and the other one for guiding navigation of the robotic arm. There are two 5 DOF robotic arms: one on the robot for navigating the Eddy current sensor probe, and the other one for the operator/inspector, who can observe the camera's visual feedback and then control this arm for manual operation purposes. The robot uses an IR sensor mounted on top of the manipulator to give the feedback to operator by triggering a tiny vibrating motor on the Haptic device. The robot has two roller chains, and each roller chain is integrated with two hall-effect sensors, which provide velocity feedback for the PID speed controller. Figure 2.3 illustrates the sensor's

mounting for each roller chain as we use two hall-effect sensors, which are mounted next to each other and close to the robot's roller.

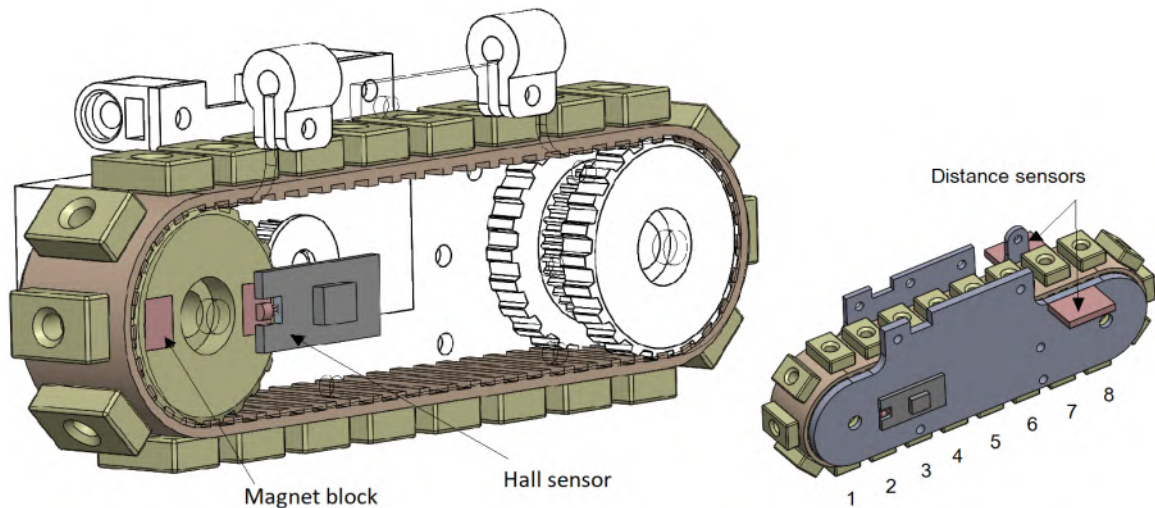


FIGURE 2.3: Roller chain with integrated Hall sensor and IR distance sensors. The IR sensor is served as feedback of the PID control to regulate the reciprocating mechanism automatically on different contour surfaces. The detail of the PID control function is described in Subsection 2.2.1 and Figure. 2.11.

Since the magnet block inside each roller chain will move when the robot moves, we can extract the velocity and traveling distance of each roller chain after combining the data from these two hall-effect sensors. Additionally, an Inertial Measurement Unit (IMU) is used for the robot's localization. Moreover, to avoid falling off, the robot has IR (Infrared Radiation) sensors mounted on the robot to detect if a surface underneath exists.

For fatigue crack detection on steel structure, the Eddy current sensor's probe (Nortec 600) as shown in Figure 2.4 is integrated with the robot. A mini 5-DOF robotic arm (Figure 4.5a) is designed to hold and move the Eddy sensor's probe for data collection as demonstrated in Figure 4.5b.





FIGURE 2.4: (Left) Industrial Eddy current sensor Nortec 600; (Right) sensor probe for data collection.

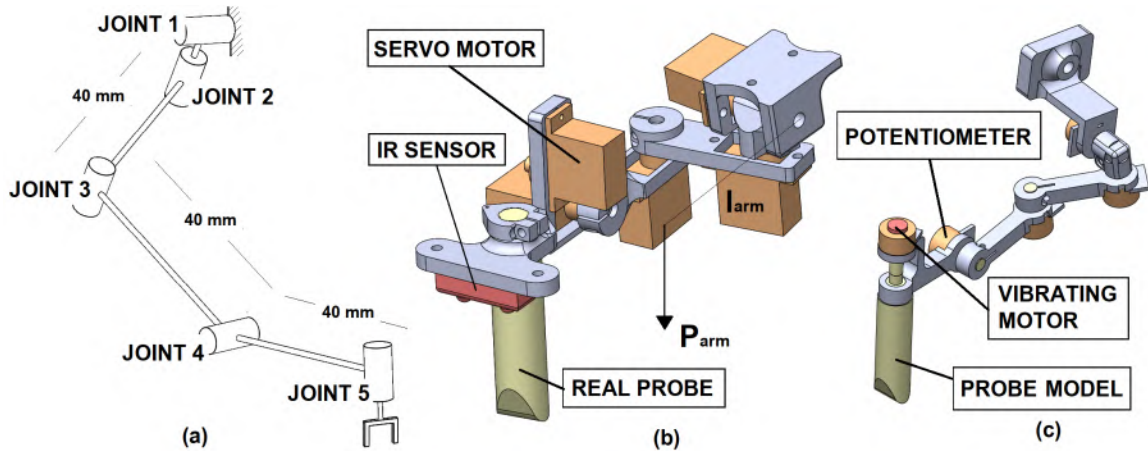


FIGURE 2.5: a) kinematic structure of 5-DOF arm; b) executive arm integrating on the robot; c) controlling arm for user operation in manual mode.

The maximum moment on joint 1 in Figure 4.5a is described as

$$M_{arm} = P_{arm} * l_{arm}, \quad (2.1)$$

where  $P_{arm} = 0.3kg$  is the total weight of the manipulator's arm,  $l_{arm} = 6cm$  is the distance from the center of manipulator mass to joint 1, so  $M_{arm} = 0.18N.m$ . Five

motors used are 0.25 N.m-torque-mini servos, which satisfy equation (2.1).

On the ground station, the operator observes visual feedback from the camera and then controls a simulated arm (same scale as the one integrated with the robot) by holding and moving a probe model. The moving control signal is wirelessly sent via the Xbee module to control the arm of the robot. Five joint angles are obtained by potentiometers (Figure 4.5c) and then processed before sending required control angles to servo motors. An IR sensor is mounted on the Eddy current sensor's probe to determine whether the probe approaches the steel surface or not. When the distance from the IR sensor to the surface meets a calibrated number (45mm), a signal will be sent back to the ground station to trigger a tiny vibrating motor on the simulated arm to enable Eddy data collection. Additionally, a pressure spring is placed between the probe and the robotic arm to improve the sensor's approach. This design helps the sensor's probe to efficiently collect Eddy current data on complex surfaces such as weld, rough or curving.

## 2.2 Mechanical Design and Analysis

A tank-like robot mechanism design is proposed to take advantage of the flexibility in maneuvering. Two motors are used to drive two roller chains, and another motor is used to drive the transformation of the robot to approach different contour surfaces.

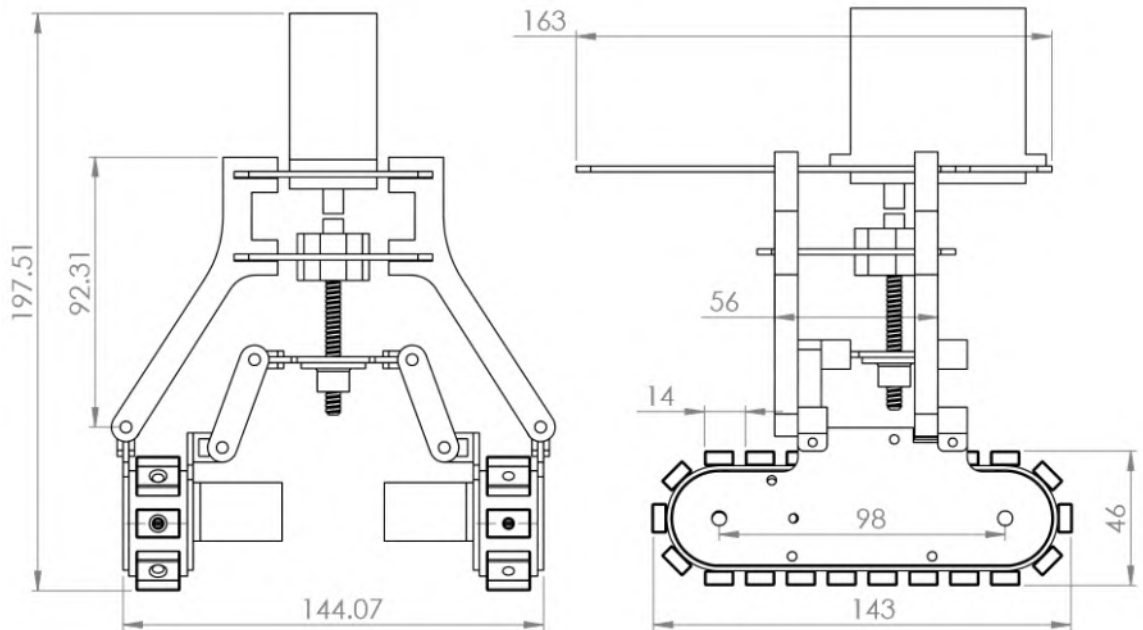


FIGURE 2.6: Reciprocating mechanism for robot transformation and specifications of the robot's design (unit in mm).

The robot's parameters are shown in Table 2.1 while the motor's parameters are listed in Table 2.2.

TABLE 2.1: Robot Parameters.

<b>Length</b>	163 mm
<b>Width</b>	145 mm
<b>Height</b>	198 mm
<b>Weight</b>	3 kg
<b>Drive</b>	2 motorized roller-chains and 1 motorized transformation

Regarding magnetic force, denote that  $F_{mi}$  is the magnetic force created by each magnet block as shown in Figure 2.3. At each moment there are a maximum of 8 magnet blocks in the chain contacting the steel surface. Hence, we have the magnetic force created by each robot's roller chain as  $\sum F_{m_j} (j = 1 : 8)$ . Since the robot has two

TABLE 2.2: Motor Parameters.

	<b>Moving motors</b>	<b>Transforming motor</b>
<b>Torque</b>	1.2 N.m (2S Li-Po)	3.2 N.m
<b>Speed</b>	0.12 sec/ 60 (2S Li-Po)	0.15 sec/ 60 (2S Li-Po)
<b>Length</b>	40.13 mm	60.5 mm
<b>Width</b>	20.83 mm	30.4 mm
<b>Height</b>	39.62 mm	45.6 mm
<b>Weight</b>	71 g	156 g
<b>Voltage</b>	6-8.5V (2S Li-Po battery)	6-8.5V (2S Li-Po battery)

TABLE 2.3: Pull Force ( $P^F$ ) Over Air Gap of  $15\text{mm} \times 10\text{mm} \times 5\text{mm}$  magnet block N35.

Distance (mm)	Pull Force $P^F$ (Newton - N)		
	Magnet to steel plate	Between two steel plates	Magnet to mag- net
0	39.7	73.1	39.7
1	17.1	29.8	22
2	10.1	17	15.3
3	6.4	10.5	11.1
4	4.3	6.9	8.4
5	2.9	4.6	6.4
6	2	3.2	5
7	1.5	2.2	4
8	1.1	1.6	3.2
9	0.8	1.1	2.5
10	0.6	0.8	2.1

roller chains, the total magnetic adhesive force,  $F_m$ , created by these two roller-chains is:

$$F_m = 2 * \sum F_{m_j} (j = 1 : 8). \quad (2.2)$$

A roller chain is designed to carry 22 Neodymium magnet blocks with poles on flat

ends as presented in Figure 2.1-front view. With each motion, there will be a maximum of 8 magnet blocks contacting the flat steel surface. According to [83], if there is a gap between magnet blocks and steel frame, the pull force is significantly affected. The characteristics of the used magnets ( $15\text{mm}$  length  $\times 10\text{mm}$  width  $\times 5\text{mm}$  thickness magnet block) are described in Table 2.3 and pull force over air gap is shown in Figure 2.7.

Roller chains are designed to enable the robot to overcome several real climbing scenarios including transitioning among surfaces with different inclination levels ( $0 - 90$  degree change in orientation) or getting rid of being stuck. A reciprocating mechanism has been added in order to transform the robot to adapt to different contour surfaces as shown in Figure 2.8. The specifications of the robot's design are shown in Figure 2.6.

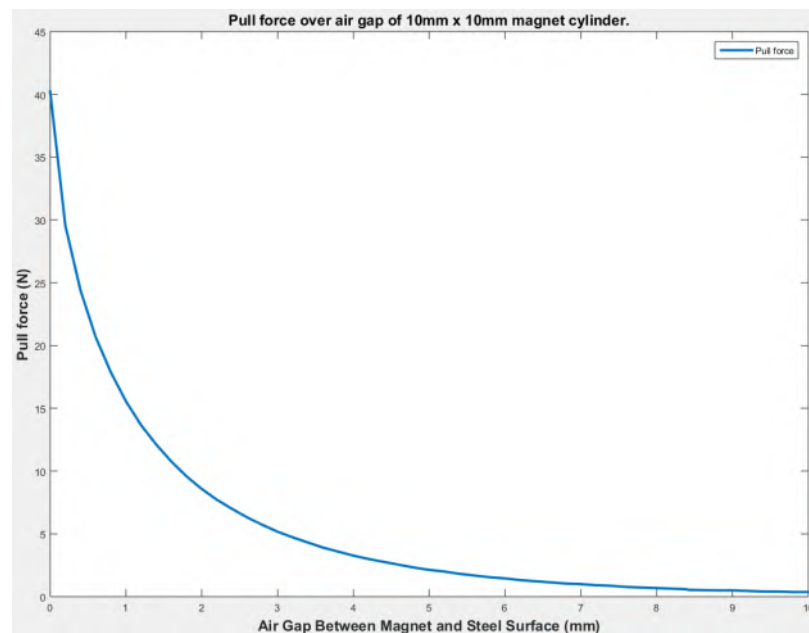


FIGURE 2.7: Pull force over air gap of  $10\text{mm} \times 10\text{mm}$  magnet cylinder.

## 2.2.1 Robot transformation kinematics

TABLE 2.4: Kinematics Parameters.

<b>b</b>	72 mm
<b>b1</b>	45 mm
<b>f</b>	11 mm
<b>e</b>	55 mm
<b>a</b>	33.7 mm
<b>XY</b>	32 mm
$\gamma$	12 degree

Kinematics analysis of the reciprocating mechanism is to calculate the radius of the steel cylinder ( $x$ ), that the robot can climb on. Table. 2.4 shows kinematic parameters while Figure 2.8 presents the kinematics of the robot, and Figure 2.9 illustrates a general architecture of the robot's reciprocating mechanism.

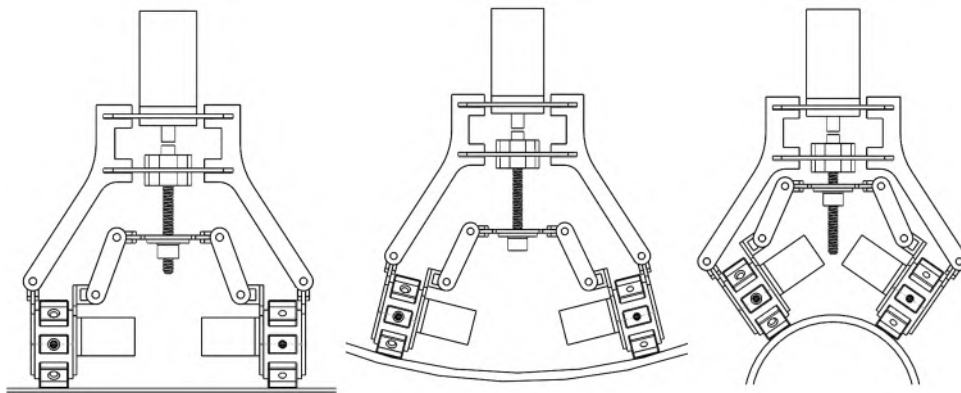


FIGURE 2.8: Reciprocating mechanism for robot transformation on different surfaces: flat, negative curve, and positive curve.

$$\text{From Figure 2.10: } x = IC - CR, \text{ in which, } IC = \frac{CF}{\cos \beta} = \frac{OF - OC}{\cos \beta} = \frac{b - \frac{f}{\cos \alpha}}{\cos \beta} = \frac{b}{\cos \beta} - \frac{f}{\cos \alpha \cos \beta};$$

$$CR = e - BC = e - f \tan \alpha \text{ with } \alpha + \beta = 90 \text{ degree;}$$

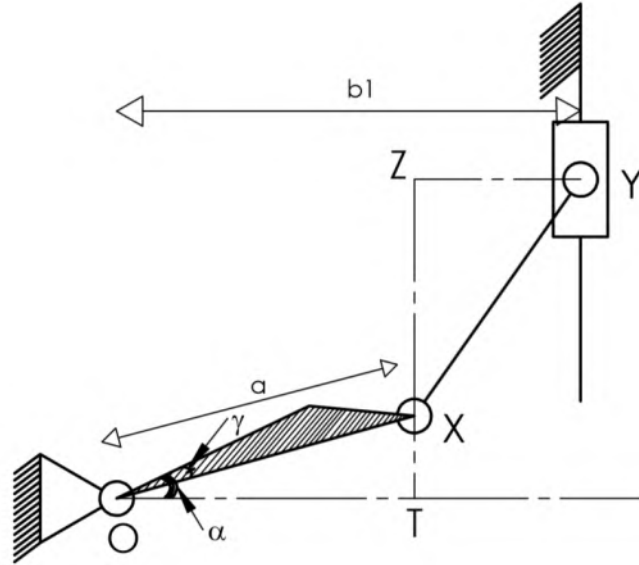


FIGURE 2.9: Reciprocating mechanism:  $a = 33.7\text{mm}$ ,  $XY = 32\text{mm}$ , and  $\gamma =$  degree.

$$\rightarrow x = \frac{b}{\cos \beta} - \frac{b}{\cos \alpha \cos \beta} - e + f \tan \alpha. \quad (2.3)$$

$$\rightarrow b = \frac{\cos \alpha \cos \beta (f \tan \alpha - x - e)}{\cos \alpha - 1}. \quad (2.4)$$

From Figure 2.9:  $y = XZ = \sqrt{XY^2 - YZ^2}$ , where  $YZ = b_1 - OT \Leftrightarrow YZ = b_1 - OX \cos \phi$ ; ( $\phi = \alpha - \gamma$ );

$$\rightarrow y = \sqrt{XY^2 - (b_1 - a \cos \phi)^2}. \quad (2.5)$$

From equation (2.4), ( $b_1 = b - 27$ ) Fig. 2.10 and equation (2.5) we get  $y = f(x)$ :

$$\rightarrow y = \sqrt{XY^2 - \left( \frac{\cos \alpha \cos \beta (f \tan \alpha - x - e)}{\cos \alpha - 1} - a \cos \phi - 27 \right)^2}. \quad (2.6)$$

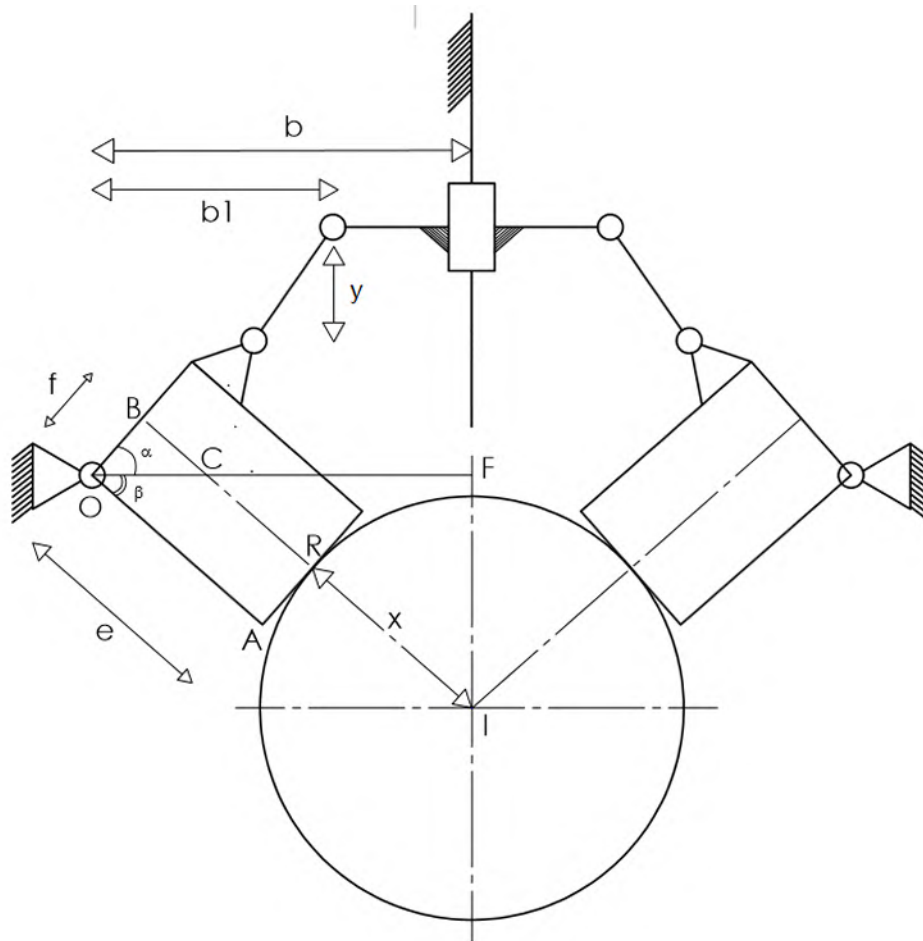


FIGURE 2.10: Kinematics of the robot transforming mechanism:  $b = 72mm$ ,  $b_1 = 45mm$ ,  $f = 11mm$ , and  $e = 55mm$ .

The feed screw mechanism has a gear ratio is 1 : 19 with a screw pitch is  $0.8mm$ .

From equation (2.6) and the designed gear ratio of 1:19, we can calculate the radius  $x$  of the steel cylinder based on the rotations of the transformation motor. The robot is designed to work on steel cylinders having the smallest radius from  $+5cm$  to  $-25cm$  with  $7.5cm$  feed screw movement.

When the robot travels on different contour surfaces, the reciprocating mechanism is driven automatically by the driving motor, which is based on feedback from two IR



distance sensors. A PID controller is applied to maintain the distance between the two sensors and the steel surface equally as illustrated in Figure 2.11. The controller helps keep the approaching area of the permanent magnet with the steel surface consistent.

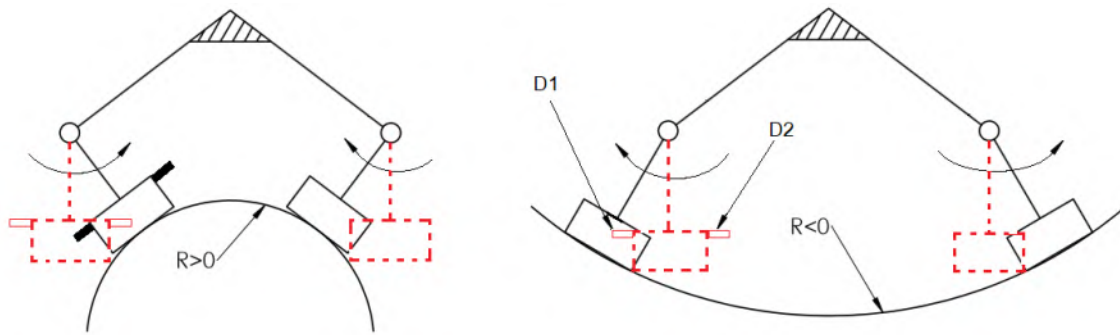


FIGURE 2.11: Examples of different cases when the robot moves from flat to curved steel surface: (Left) positively curved surface; (Right) negative curved surface. A PID controller will be activated to keep the distance of two sensors D1 and D2 equally.

## 2.2.2 Sliding Failure Investigation

To understand the stability of the robot while climbing on steel structures, the sliding and turn-over failures as illustrated in Figure 2.12 (a,b) should be investigated.

In the general case, based on the proposed design, the robot can climb on different shapes of structures (cylinder, cube, or flat) with different inclination levels as shown in Figure 2.13. In this analysis, we focus on the basic working condition-flat surfaces to calculate the needed magnets and motor parameters, then do experiments on different surfaces (curving, cube) in different conditions to find out optimal results.

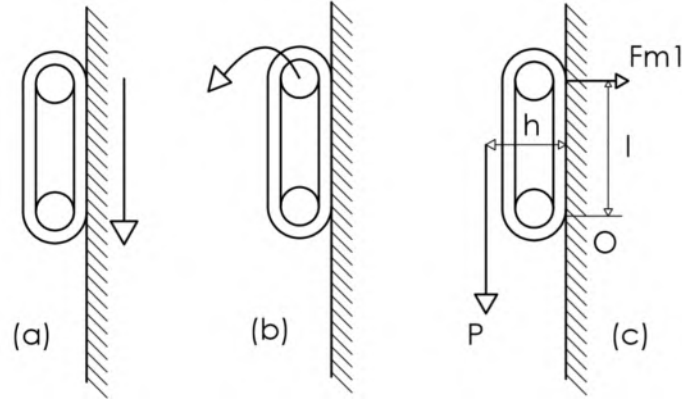


FIGURE 2.12: a) Sliding failure; b) Turn-over failure; (c) Moment calculation at point  $O$ .

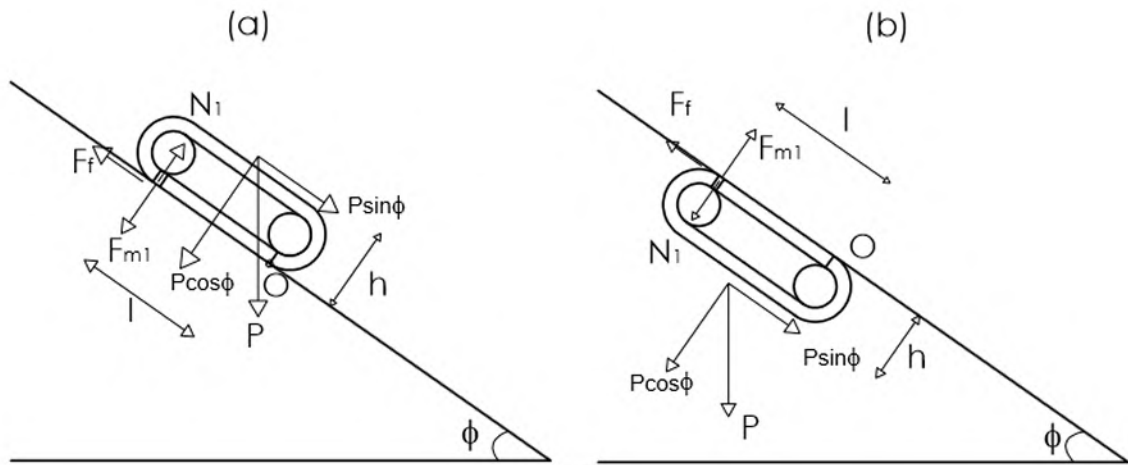


FIGURE 2.13: a) Climbing on top inclined surface; b) Climbing underneath inclined surface.

Let  $P$  be the robot's total weight ( $P = mg$ , where  $m$  is the robot's mass, and  $g$  is the gravitational acceleration). Let  $F_m$  be the magnetic adhesive force,  $N$  be the reaction force,  $\mu$  be the frictional coefficient,  $F_f$  be the frictional force, and  $\phi$  be the degree of inclination. Denote  $\sum F$  as the total force applied to the robot. Based on Newton's second law of motion,  $\sum F = 0$  when the robot stops.

When the robot climbs on top of an inclined surface (Figure 2.13(a)), based on our

previous work [36], we can obtain the magnetic adhesive force:  $F_m = \frac{P \sin \phi}{\mu} - P \cos \phi$ .

Hence, the sliding failure can be avoided if the magnetic force satisfies the following condition:

$$F_m > \frac{P \sin \phi}{\mu} - P \cos \phi. \quad (2.7)$$

When the robot climbs underneath an inclined surface (Figure 2.13(b)), we obtain:

$F_m = \frac{P \sin \phi}{\mu} + P \cos \phi$ . In this case, the magnetic force should be

$$F_m > \frac{P \sin \phi}{\mu} + P \cos \phi. \quad (2.8)$$

When the robot climbs on a vertical surface ( $\phi = 90^\circ$ )

$$F_m > \frac{P}{\mu}. \quad (2.9)$$

From equations (2.7), (5.14) and (2.9), to avoid sliding failure in many cases, the magnetic force should be

$$F_m > \max \left\{ \frac{P \sin \phi}{\mu} - P \cos \phi; \frac{P \sin \phi}{\mu} + P \cos \phi \right\}. \quad (2.10)$$

Since  $0 < \phi \leq 90 \Rightarrow \cos \phi \geq 0$ , the overall condition for avoiding sliding failure is

$$F_m > \frac{P \sin \phi}{\mu} + P \cos \phi. \quad (2.11)$$

Assume that the frictional coefficient  $\mu$  between two roller-chains and steel surface is from  $[0.4 - 0.8]$ , we see that  $\left(\frac{\sin \phi}{\mu} + \cos \phi\right)$  decreases when  $\mu$  increases, or we have:

$$0.4 \leq \mu \leq 0.8; 0 < \phi \leq 90$$

$$\Rightarrow \max\left\{\frac{\sin \phi}{\mu} + \cos \phi\right\} = 2.5 \Rightarrow F_m \geq 2.5P.$$

In summary, the robot's magnetic adhesive force should be greater or equal to 2.5 of the robot's weight. The value of one permanent magnet, where  $n = 8$  is the maximum number of magnet blocks contacting to the steel surface, satisfies the condition (5.16).

$$F_{m_j}(j = 1 : n) \geq \frac{2.5P}{n}. \quad (2.12)$$

### 2.2.3 Turn-over Failure Investigation

Let  $l$  be the distance between the first and last magnet block contacting the surface, and  $h$  be the distance between the center of mass to the surface (Figure 2.12c). The moment at point  $O$  (the point that the first magnet block contacts the steel surface) is calculated as follows:

$$\sum M = P * h - 2F_{m_1} * l = 0 \Leftrightarrow F_{m_1} = \frac{P * h}{2l}.$$

To avoid turn-over failure, the magnetic force of the first contacting magnet block:

$$F_{m_1} > \frac{P * h}{2l}. \quad (2.13)$$

From (2.13), to avoid the failure we can lower  $\frac{h}{l}$ , which means making the robot's center of mass closer to the steel surface. In the proposed design (Figure 2.6),  $h = 4.6\text{cm}$ , and the total robot height  $h_r = h + 9.231\text{cm} = 19.751\text{cm}$ . Therefore, to avoid both sliding and turn-over failures, the robot's magnetic force of each magnet block should satisfy:

$$F_{m_j}(j = 1 : n) > \max\left\{\frac{2.5P}{n}; \frac{P * h_r}{2l}\right\}. \quad (2.14)$$

Following the proposed design,  $P = 30\text{N}$ ,  $n = 16$  magnet blocks (each roller-chain has a maximum of 8 magnet blocks contacting the steel surface),  $l = 9.8\text{cm}$ , or  $F_{m_j}(j = 1 : 16) > \max\left\{\frac{2.5 * 3}{16}; \frac{3 * 19.751}{2 * 9.8}\right\} > 3(N)$ . We conducted some tests as discussed in subsection 2.3.1 to make sure the proposed design satisfied this condition.

## 2.2.4 Magnetic Force Analysis on Curved Surfaces

The previous analysis is only applied when the robot moves on a flat steel surface. However, there are also structures, which have curving surfaces, so the following analysis will help determine the impact of the curving surface on the magnetic force created by the robot.

An experiment conducted on different steel cylinder shapes with real conditions to verify the performance of magnet blocks working on curving surfaces is shown in Table. 2.5.

TABLE 2.5: Average Pull force ( $P^F$ ) over inside and outside steel cylinders of  $15 \times 10 \times 5mm$  magnet block  $N35$ . The experiment was conducted on  $5mm$  thickness steel with  $0.2mm$  paint on the surface.

Diameter (mm)	Pull Force $P^F$ (Newton - N)
100	13.5
200	15.5
300	16.2
400	17.4
500	19.3
600	20.9
700	23.2
800	25.4
900	28
flat	32.5
-900	24.4
-800	21.2
-700	19.7
-600	18.3
-500	17.2

The minimum pull force is  $13.5N$  at  $100mm$  diameter steel cylinder, and this means that it is always greater than  $3N$ , the required force, as shown in equation (2.14).

### 2.2.5 Motor Torque Analysis

Apart from the magnetic force analysis, we have conducted another analysis to determine the appropriate motor to drive the robot. In order to make the robot move,

the force created by the motor should win the adhesive force of the last permanent magnet and the steel surface. As shown in Figure 2.14, denote  $M$  as the torque of one motor,  $Q$  is the rotation fulcrum,  $i$  is the arm from  $F_{m_j}$  to  $Q$ . Assume that the total driving force of the robot is the sum of two motor forces, and the required moment is satisfied:

$$M > h_r * \frac{P \sin \phi}{2} + F_{m_j}(j = 1 : n) * i.$$

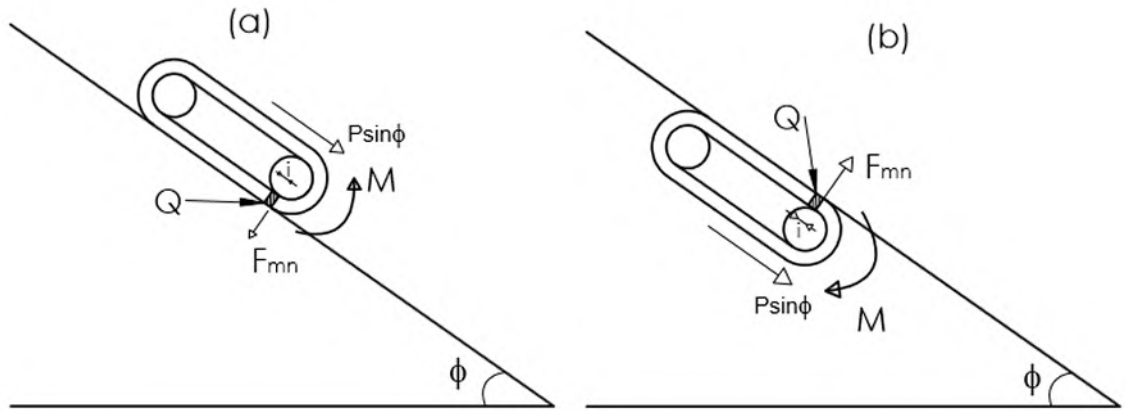


FIGURE 2.14: a) Robot moves on top of inclined surface; b) Robot moves on bottom of inclined surface.

When the robot moves on a vertical surface, maximum  $\phi = 90^0$

$$M > h_r * \frac{P}{2} + F_{m_j}(j = 1 : n) * i. \quad (2.15)$$

$\rightarrow M > 3.16(N.m)$  with  $h_r = 19.751cm$ ,  $P = 30N$ ,  $g = 9.8$ ,  $F_{m_n} = 39.7N$  (obtained this number from the magnet's datasheet),  $i = 5mm = 0.5cm$ . The selected moving motor moment is  $1.2N.m$  and the gear ratio is  $7 : 20$ , hence the moment of a robot roller-chain is  $3.43N.m$ , which satisfies (2.15).

Regarding transformation mechanism as shown in Figure 2.15, when the robot moves from a flat surface to a curved surface or reverses, the transforming mechanism works to make sure that the roller chains contact steel surfaces in the best condition. The

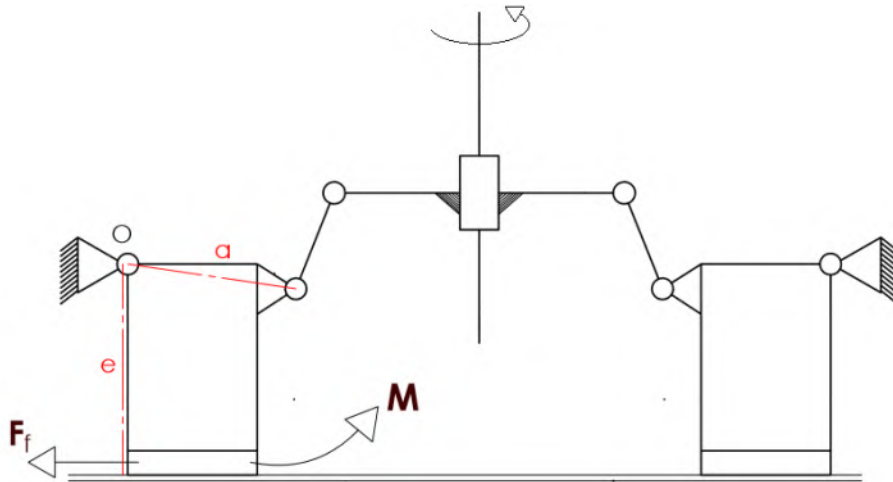


FIGURE 2.15: Transformation mechanism with 7 joints to create climbing flexibility of the robot.

transformation motor through the mechanical system creates moment ( $M$ ) to release magnet blocks from the steel surface. However, the calculation gear ratio of the reciprocating mechanism is not simple due to its non-linearities, as shown in equation (2.5). We choose the special case when friction is strongest to calculate the moment of the transforming motor (powering feed screw mechanism). The moment has to satisfy:  $M > F_f * e \Leftrightarrow M > e * (k.N) \Leftrightarrow M > e * k(P + F_m)$ .

$$\Rightarrow M > e * k(P + nF_{m_j}(j = 1 : n)). \quad (2.16)$$

From equation (2.5) and the kinematics parameter of the reciprocating mechanism, it is straightforward to calculate the gear ratio in this case. The ratio  $\alpha : y$  is



approximately 1 degree: 1 mm. Besides, the ratio of  $a$ :  $e = 1 : 1.7$ , and the gear ratio of the feed screw is  $0.8mm$ : 360 degree. As a result, the total gear ratio of the whole system is  $26.5 : 1$ . From equation (2.16) and the assumption that system efficiency is 80%, the required moment of the motor is  $> 1.375N.m$ . The selected transformation motor with  $3.2N.m$  is satisfied.

When the robot travels on curving surfaces, the reciprocating mechanism is driven automatically by driving the motor based on IR sensor signals. A PID controller is also applied to maintain the distance between the IR sensor and the surface. This is to keep approaching the area of permanent magnets with the steel surface consistent.

## 2.3 Robot Deployment

To evaluate the design and performance of the robot, experiments for evaluating the magnetic force created by roller chains have been conducted. The ability of climbing and failure avoidance were tested. During the test, a Lipo battery (2 cells) 7.4V 900 milliamper-hour ( $mAh$ ) is used to power the robot for about 1 hour of working. One laptop which can connect to a wireless LAN is used as a ground station. The robot's mass  $m = 3kg$ , and if we assume that the gravitational acceleration  $g = 10m/s^2$ , the total weight of the robot is approximately  $P = mg = 30N$ . Since  $15mm \times 10mm \times 5mm$  magnet blocks are used, the total magnetic force is calculated

as

$$\begin{cases} F_{m_j}(j = 1 : 8) = 39.7(N) \\ F_m = 2 * 8 * F_{m_j} = 635.2(N) \end{cases} \quad (2.17)$$

which satisfies the magnetic force condition as presented in equation (2.14).

## 2.3.1 Adhesive Force Measurement

### 2.3.1.1 Static condition

In order to measure the adhesive force created by a permanent magnet, we have set up an environment as shown in Figure 5.21. The robot's body - whose mass is  $m = 3kg$  - is placed on top of a flat steel surface while it is connected to a scale through an inelastic wire. We create a pull force onto the scale trying to lift the robot off the surface. At the time the robot is about to be off the surface, the force applied to the scale is equal to the sum of the robot's weight and the magnetic pull force. Denote  $F_{pull}$  as the force we applied onto the scale,  $M$  is the value shown on the scale while  $P$  is the weight of the robot's body, and  $F_{mag}$  is the magnetic force. With  $g = 10m/s^2$ ,  $P = mg = 30N$  and  $F_{pull} = Mg = 10M$ , we can calculate magnetic adhesive force as follows.

$$\begin{aligned} F_{pull} &= P + F_m \Rightarrow F_m = F_{pull} - P \\ &\Rightarrow F_{mag} = 10M - 3(N). \end{aligned} \quad (2.18)$$

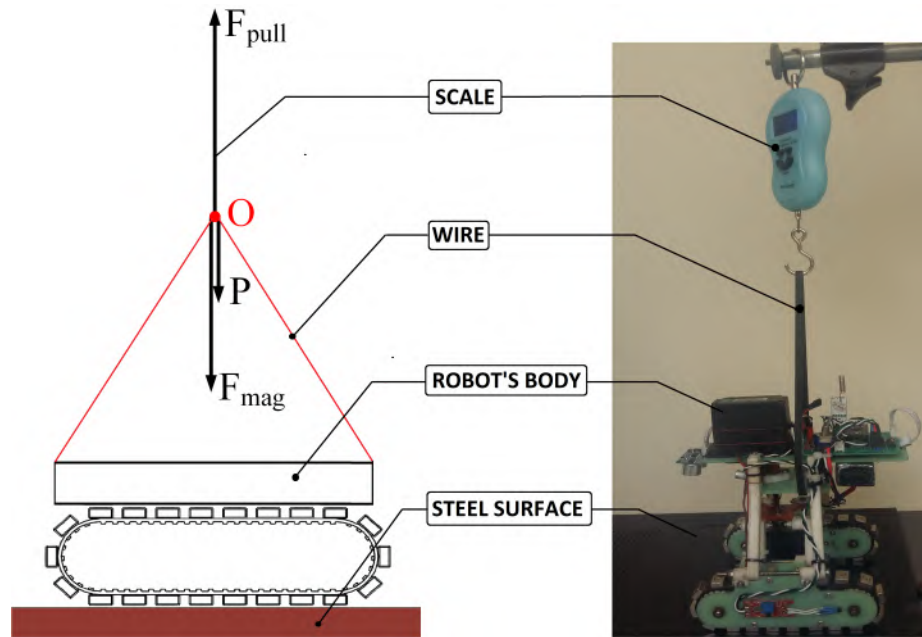


FIGURE 2.16: Experimental setup for magnetic force measurement.

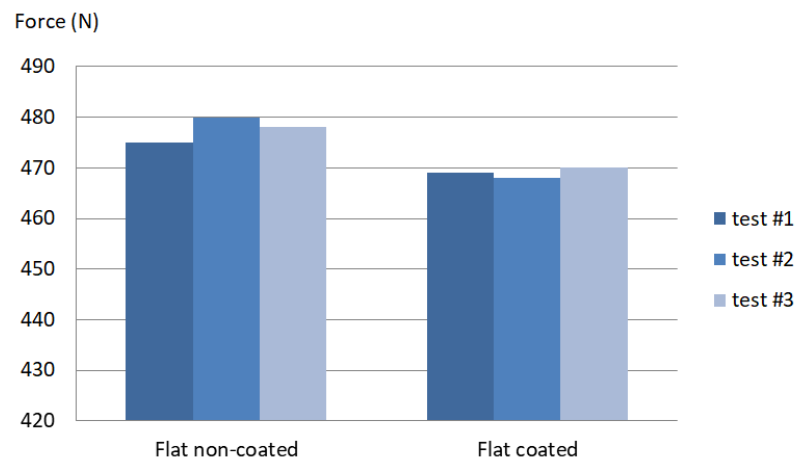


FIGURE 2.17: Magnetic force measurements on coated and non-coated flat steel surface.

### 2.3.1.2 Dynamic condition

We also measure the adhesive force of the robot in a moving state as shown in Fig. 2.19 (robot moves from right to left). Each measurement is conducted three times as

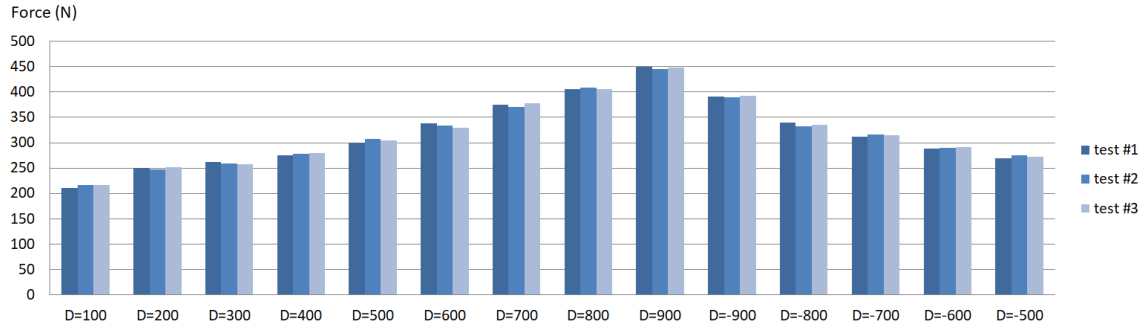


FIGURE 2.18: Magnetic force measurements on a curved steel surface with diameters (D) ranging from 100mm to 900mm.

shown in Fig. 2.20. On average, the adhesive force in dynamic conditions is lower than approximately 10% compared to a static state.

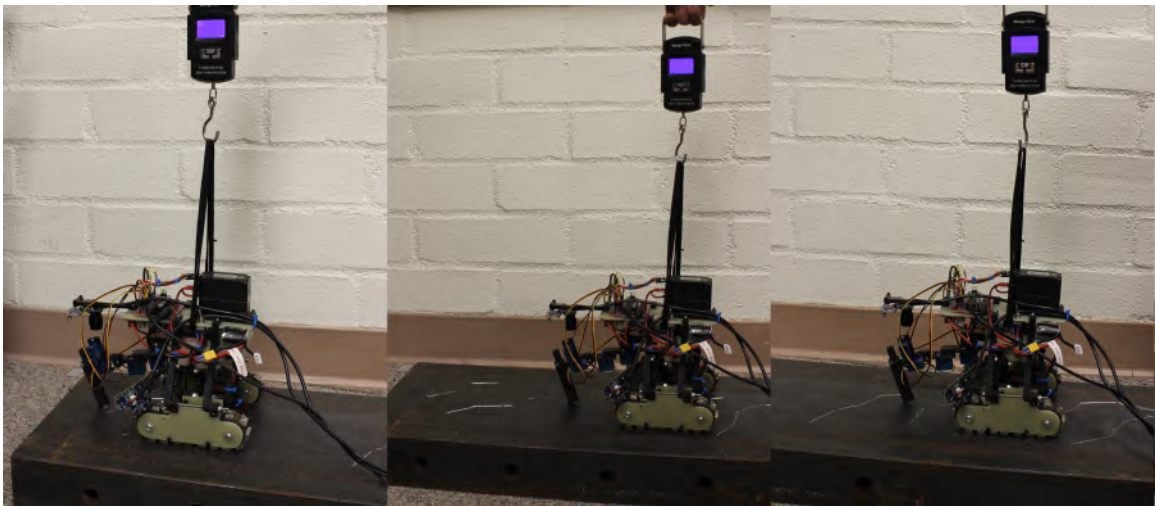


FIGURE 2.19: Adhesive force measurement in dynamic condition on a non-coated flat surface (robot moves from right to left images)

Multiple tests have been conducted to measure the pull force when the robot's body is placed on different surfaces. The first test is on a flat non-coated steel surface, the second one is on a flat coated steel surface and the third test is on curved-coated steel surfaces (positive and negative sides) with diameters (D) ranging from 100mm

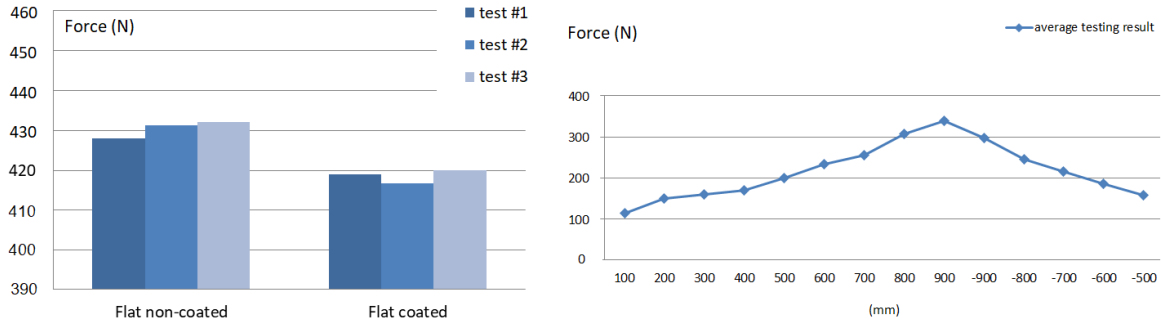


FIGURE 2.20: (Left) testing result on flat surfaces, (right) testing result on coated curving surfaces (cylinder tubes)

to 900mm. All the tests are executed three times, and the results are presented in Figure 6.11 and 6.12.

According to equation (2.14), the magnetic force for each magnet block should be  $F_{m_j}(j = 1 : n) > 3(N)$  to avoid sliding and turn-over failure. Since each time the robot has 16 magnet blocks, which physically contact the steel surface, the total required adhesive force should be greater than  $3 \times 16 = 48(N)$ . We can see that in Figure 6.11 and 6.12 the minimum magnetic force is 115(N), which is much greater than the required one, 48(N) with safety factor is around 2.5. Therefore the robot adheres well on both coated/non-coated flat and curving surfaces.

### 2.3.2 Robot field deployment

The outdoor experiments and robot deployments are conducted on more than 20 steel bridges. Due to limited space, only some typical climbing examples are shown in Figure 2.22-2.25. The steel structures have different thicknesses of paint coated on

TABLE 2.6: Statistical result.

Structrural parameters	Decription
Thinnest steel surface	1 (mm)
Smallest steel cylinder diameter	100 (mm)
Thickest coated paint	4 (mm)
Highest nut or bolt area	12 (mm)



FIGURE 2.21: Adhesive and climbing test on a thick paint-coated steel structure: flat surface.

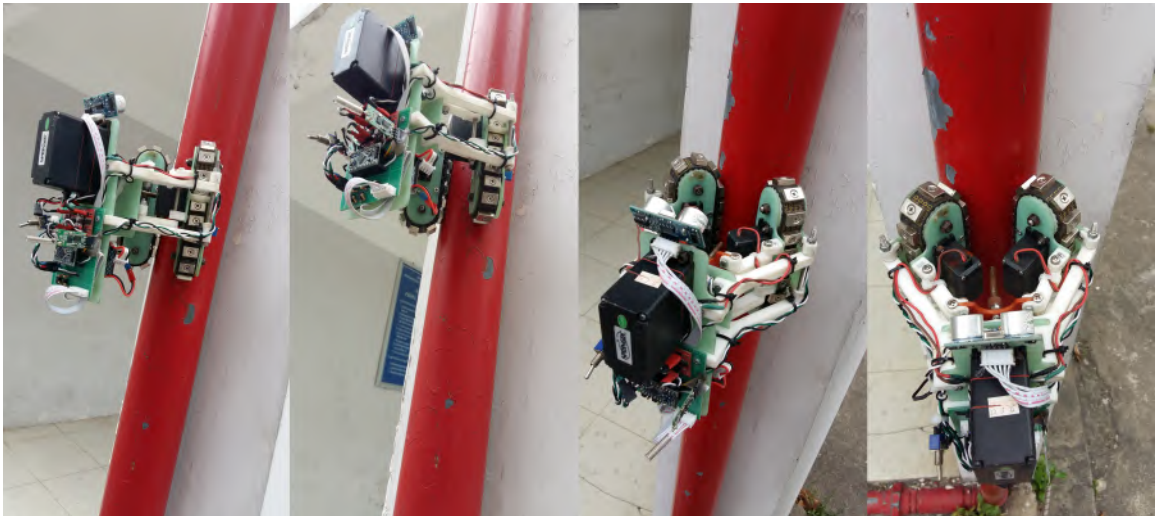
FIGURE 2.22: Adhesive and climbing test on a thin paint-coated steel structure: cylinder shape  $D=100\text{mm}$ .





FIGURE 2.23: Adhesive and climbing test on a thin paint-coated steel structure: cylinder shapes  $D=250\text{mm}$ .



FIGURE 2.24: Adhesive and climbing test on a thick paint-coated steel bridge: a flat surface.



FIGURE 2.25: Adhesive and climbing test on a rusty paint-coated steel bridge: flat structure with bolts/nuts.

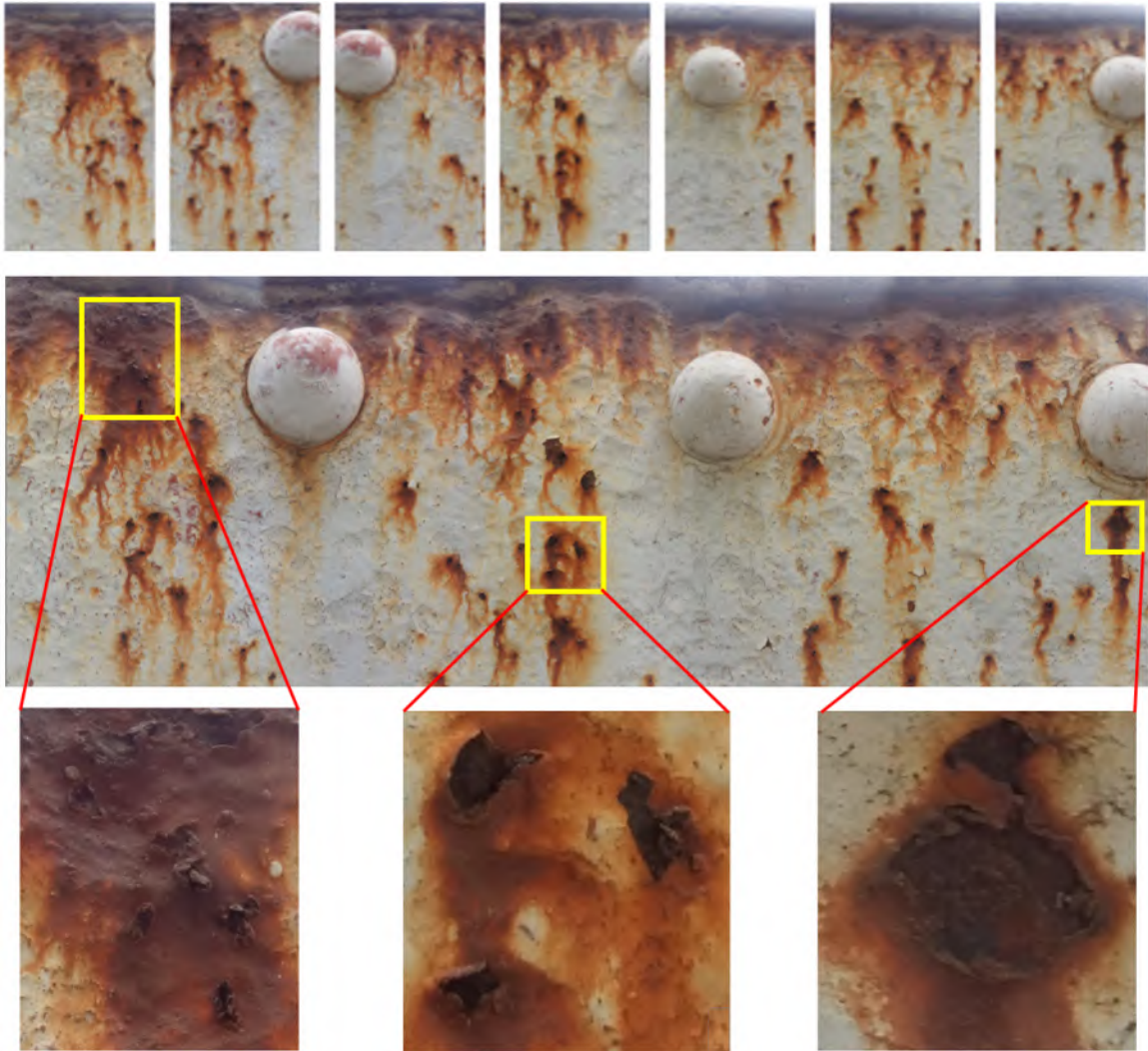


FIGURE 2.26: Images stitching result: (Top) 7 individual images taken by the robot climbing on a bridge in Figure 2.25; (Middle) Stitching image result from those 7 individual images; (Bottom) Closer look (zoom-in) at some areas, which has a serious rusty condition with holes on the surface.

steel surfaces. Some paint-coated steel surfaces are very rusty, some are not clean, and some others are still in fine condition (minor-rusty). Statistical results with a description of specifications that the robot can work with are presented in Table 2.6.

During the experiments, the climbing capability tests are done on steel bridges and steel structures, and on coated or unclean surfaces as seen in Figure 2.21 - 2.25.



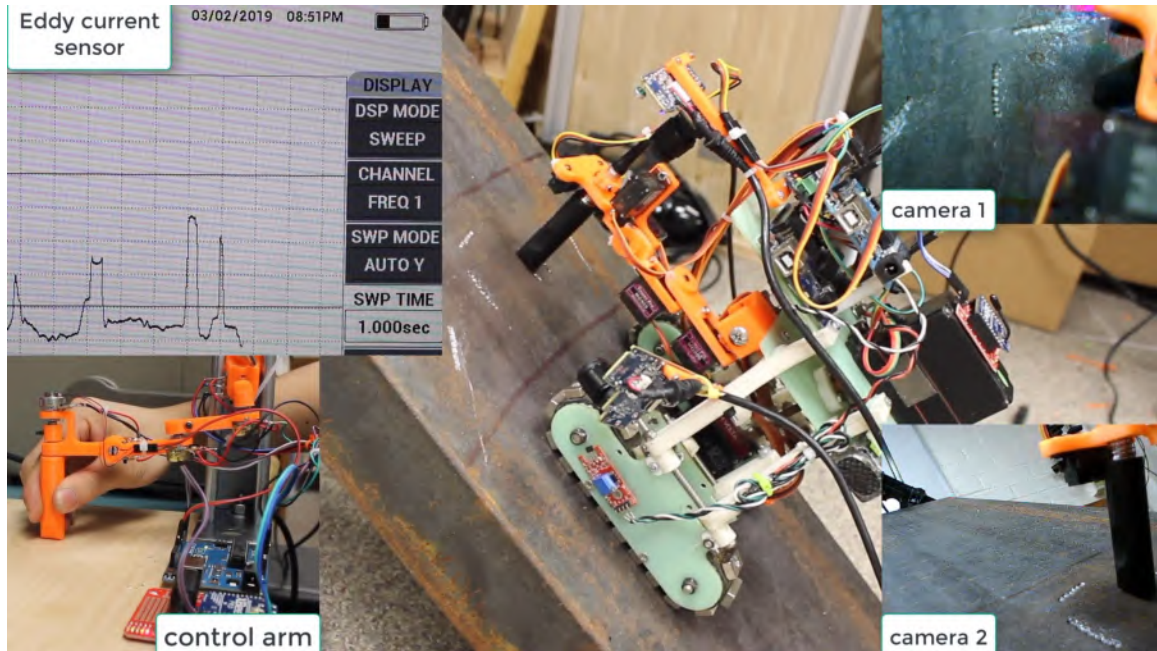


FIGURE 2.27: Crack surveying process. Visual data is acquired by camera 1 (top-right image). The operator controls Eddy current sensor's probe remotely by a haptic system (control arm: bottom-left image) with a closer view from camera 2 (bottom-right image). Eddy current sensor measures the depth of crack (top-left image), more detail in Fig. 2.28

The robot is able to adhere very well to these steel structures while climbing with a maximum speed is 200 mm/s for 1 hour. Even in the case of curved surfaces (Figure 2.22, 2.23), the robot can still adhere tightly to the steel structures while performing the climb. For rusty steel surfaces, it also shows strong climbing capability (Figure 2.25). However, in some very tough conditions, such as bird drops or high nuts, the robot might lose adhesive force and can not pass these areas. Robot deployments can be seen in the submitted video and the ARA lab link: [https://ara.cse.unr.edu/?page\\_id=11](https://ara.cse.unr.edu/?page_id=11) or youtube link: <https://youtu.be/1Wl9Trd3EoM>

The robot is controlled to move and stop at a certain distance (e.g. 12cm) to capture images of steel surfaces and does a closer investigation on potential crack areas, then

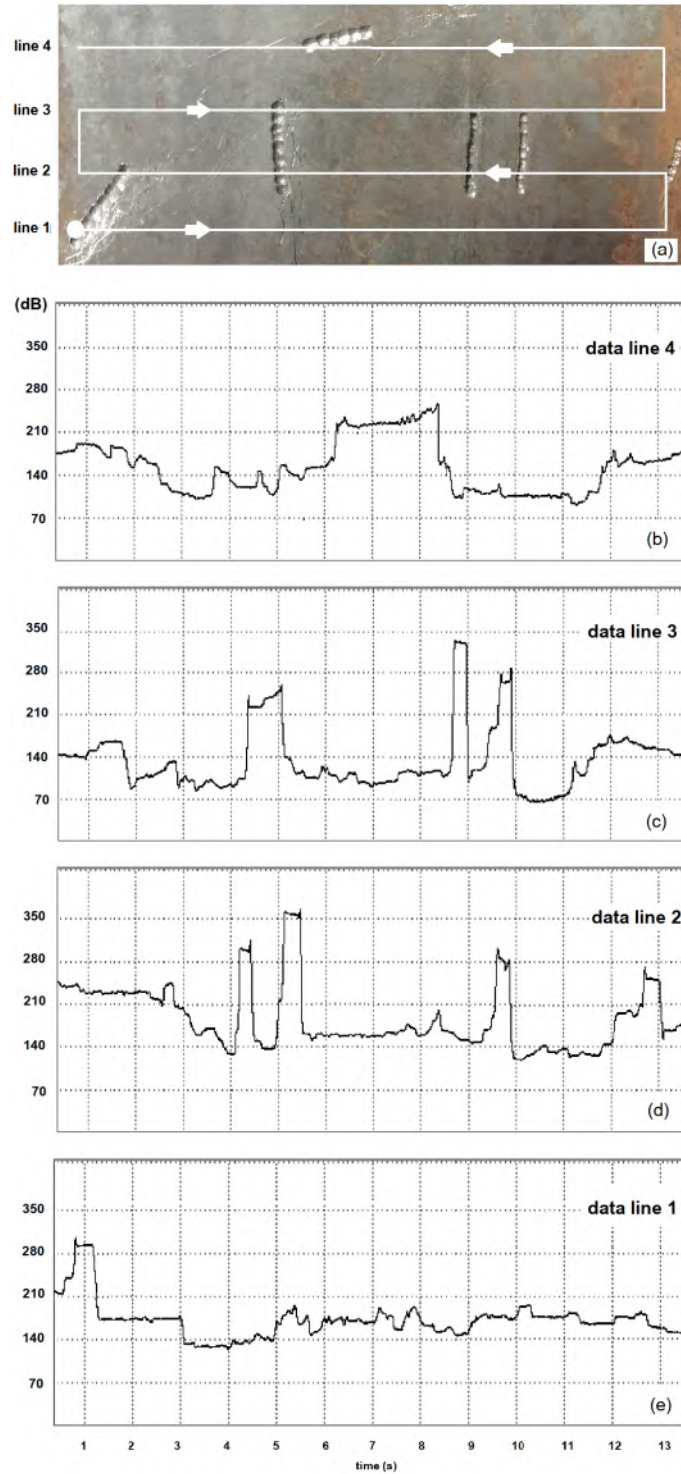


FIGURE 2.28: a) Probe path; b) line 4 data; c) line 3 data; d) line 2 data; e) line 1 data.

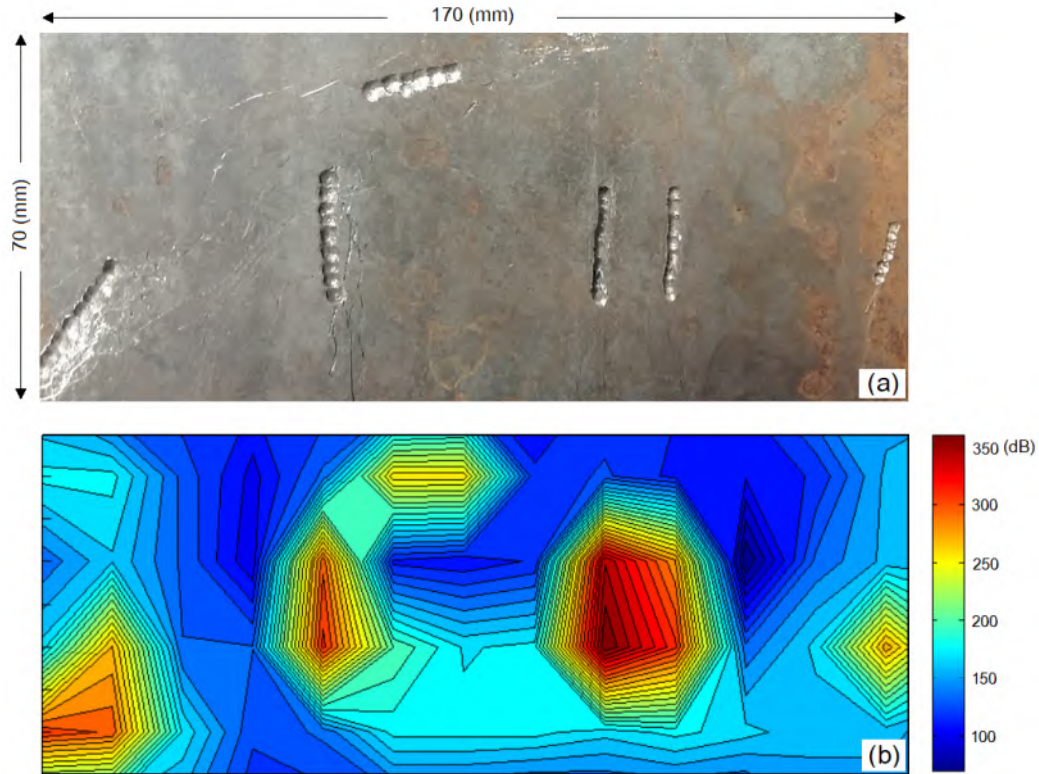


FIGURE 2.29: a) Image of an inspected area with cracks on it; b) Fatigue crack map from Eddy current sensor showing defect areas with red/yellow color, corresponding well with the crack areas on the image.

send to the ground station. To enhance steel surface inspection, acquired images are then stitched together to produce an overall image of steel surfaces as shown in Figure 2.26. The image stitching is followed by our previously developed algorithm [49].

In addition to the visual data collection, the robot also collects Eddy current sensor data. The survey is conducted on a 170 x 70 mm area, which contains some crack areas as shown in Figure 2.28a. The robotic arm holds the Eddy current sensor's probe and performs a zig-zag path consisting of four lines. Figure 2.28b-e shows raw signals collected in a 13-seconds time frame for each line. We can see from these plots that at the crack areas, the signal amplitude is higher. For ease of illustration,

a color-coded map is built as shown in Figure 2.29, and we can see that the Eddy current condition/fatigue crack map has defect areas (red/yellow color) correlating very well with the crack areas on the image.

## 2.4 Conclusion

This chapter presents a new development of a tank-like robot, which is capable of climbing on different steel structural shapes to perform inspection and evaluation. The robot design is implemented and validated on climbing more than twenty different steel bridges. During the tests, the robot is able to firmly adhere to steel structures with various inclination levels. A rigorous analysis of magnetic adhesive force has been performed to confirm that the robot is able to adhere to both flat and curving steel surfaces in various conditions (coated, non-coated, and/or rusty). Moreover, motor torque analysis to make sure the robot can win the magnetic adhesive force to move on a steel surface is presented. Various experiments have been conducted including magnetic force measurement, and indoor and outdoor climbing tests in order to validate the force analysis as well as the climbing capability of the robot. The results show that when the magnetic adhesive force requirement is met, the robot is able to move and transition safely between steel surfaces without any failures. Several sensors are integrated to support the robot's navigation as well as data collection. The rigorous magnetic force analysis can serve as a framework to calculate and design different types of steel inspection robots in the future. Inspection data (Eddy current

and visual) is collected and transferred to a ground station for visualization and processing.

## Chapter 3

# Roller Chain-like Robot

This chapter presents a novel design of the steel bridge/structure inspection robot. Compared to most existing robots designed to work on particular surface contours of steel structures such as flat or curving, the proposed roller chain-like robot can implement and transfer smoothly on many kinds of steel surfaces. The developed robot can be applied to inspection tasks for steel bridges with complicated structures. The robot is able to carry cameras and sensors for visual and specialized examination. A rigorous analysis of robot kinematics, adhesion force, and turn-over failure has been conducted to demonstrate the stability of the proposed design. Mechanical and magnetic force analysis together with turn-over failure investigation can serve as a useful framework for designing various steel climbing robots in the future. Experimental results and field deployments prove the adhesion, climbing, and inspection capability of the developed robot.



### 3.1 Overall Design

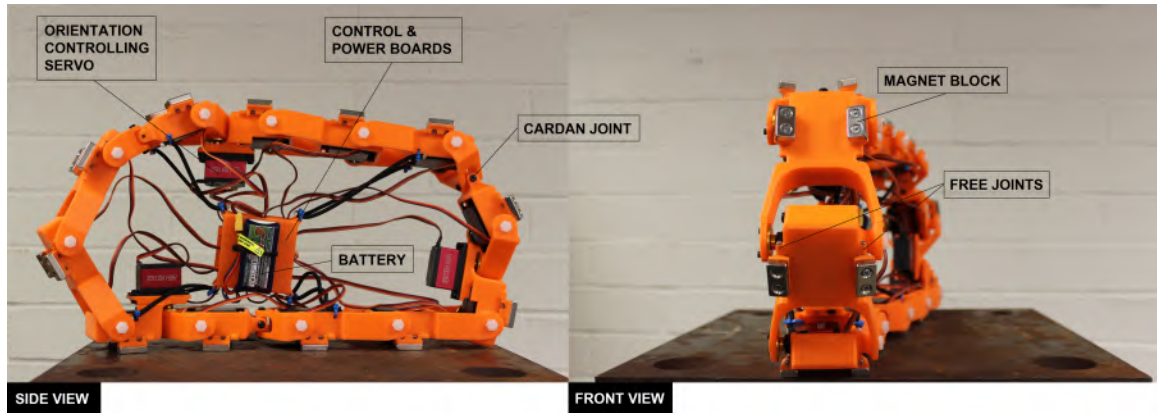


FIGURE 3.1: Overall design of a robot for steel bridge inspection tasks.

The overall design of the roller chain-like robot is depicted in Fig. 3.1. The robot consists of 12 joints for forward and backward moving; and three pairs of joints for controlling the robot's direction. The kinematic structure of the robot is illustrated in Fig. 3.2. The robot moves by the collaboration of 12 joint angles (1 to 12) that are driven via 12 servo motors. For turning, when the robot gets a state like Fig. 3.3,

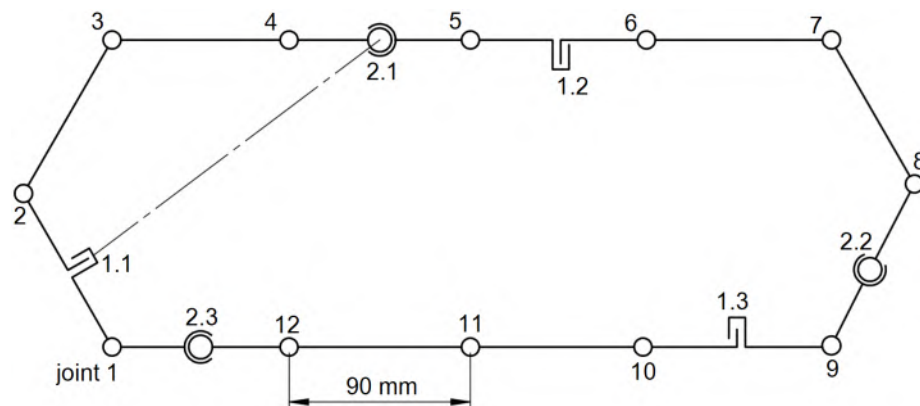


FIGURE 3.2: Robot kinematics.

joint pairs (1.1 and 2.1) drive the robot turning left or right with  $\pm 45$  degrees range,

in which, joints 1.1, 1.2, and 1.3 are active joints while 2.1, 2.2 and 2.3 are passive-cardan joints. Cardan joints are necessary in case the active and passive joints are not coaxial when the robot turns. With three pairs, the robot can turn triple times per moving revolution. On each moving joint, there are two magnet blocks, which

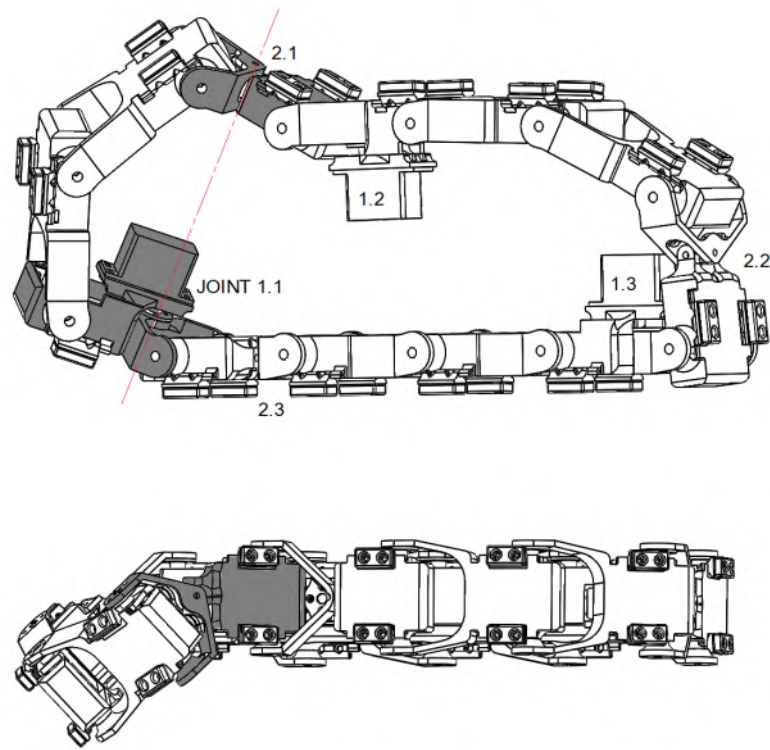


FIGURE 3.3: Robot turns left.

create adhesion force for the robot. The magnet blocks are integrated through the free joints to help the robot approach every surface contour effectively by manipulating the natural characteristic of the magnetic field. The surface with the largest force will expose before approaching magnetic materials as Fig. 3.4. The designed robot can work well on different surface contours as shown in Fig. 3.5.



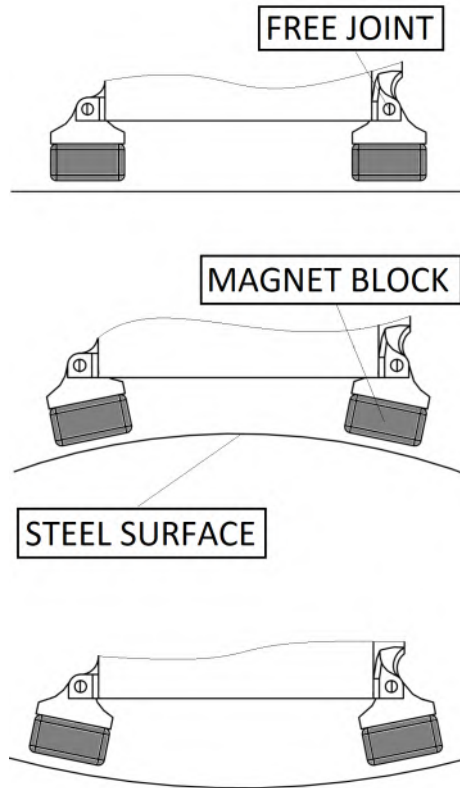


FIGURE 3.4: Magnet states before approaching steel surfaces.

## 3.2 Magnetic Force Analysis

Let  $P$  be the robot's total weight ( $P = mg$ , where  $m$  is the robot's mass, and  $g$  is the gravitational acceleration). Let  $F_m$  be the magnetic adhesion force, and  $N$  be the reaction force. Let  $l_1$  to  $l_4$  be the distance between first to last magnet block contacting the surface to point  $O_1$ , and  $h$  be the distance between the center of mass to the surface (Fig. 3.6(a)). The moment at point  $O_1$  is calculated as follows:

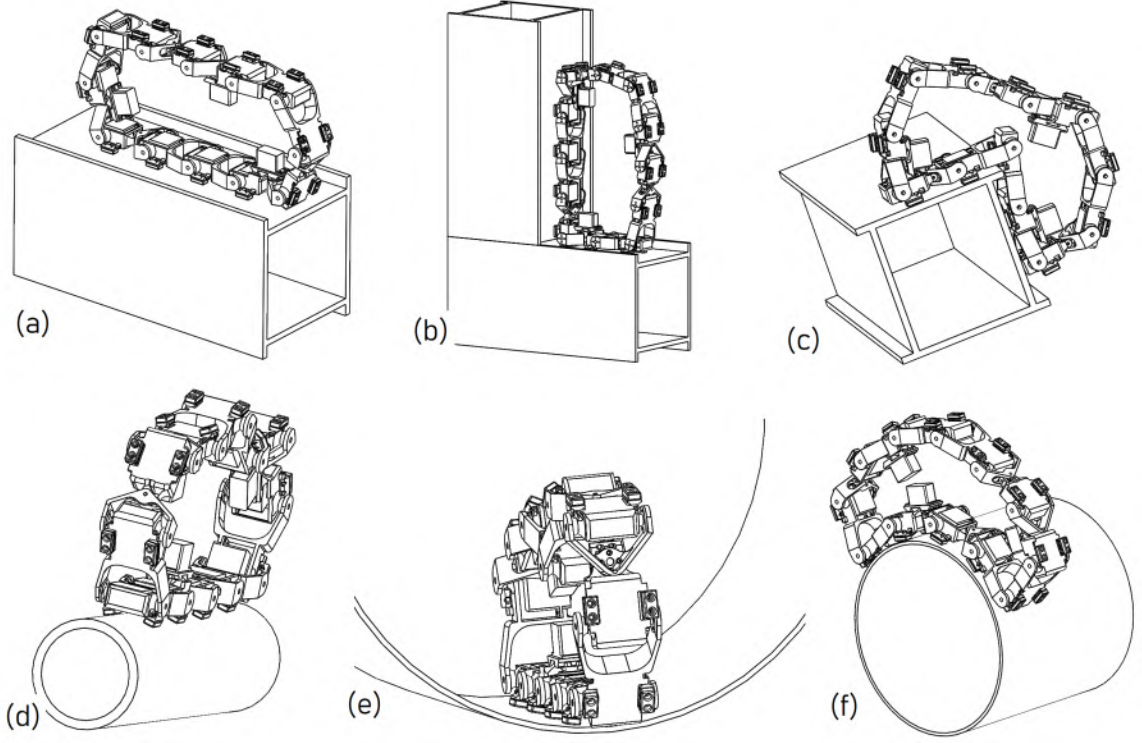


FIGURE 3.5: Robot's locomotion on different surface curvatures.(a) Robot is on flat surface.(b) Robot transfers between two surfaces.(c) Robot transfers to another surface with obstacle.(d) Robot moves on curving surface.(e) Robot moves on cylindrical surface.(f) Robot moves on circumferential direction of cylindrical object

$$\sum M_{O_1} = Ph - (l_1 F_{m1} + l_2 F_{m2} + l_3 F_{m3} + l_4 F_{m4}) = 0 \rightarrow F_{mj} = \frac{Ph}{l_1 + l_2 + l_3 + l_4} \quad (3.1)$$

In case 2, Fig. 3.6b:  $F_{m1a} = F_{m1b} = \frac{F_{m1}}{2}$ . Torque at point  $O_2$  is calculated as follows:

$$\sum M_{O_2} = Ph - (4F_{m1a}a + 4F_{m1b}b) = 0 \rightarrow F_{mj} = \frac{Ph}{2(a+b)} \quad (3.2)$$

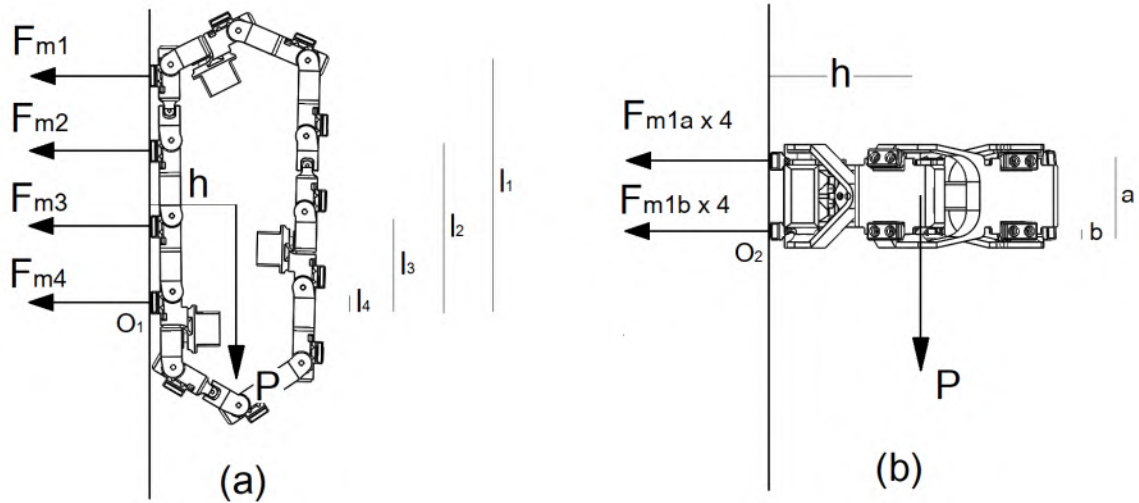


FIGURE 3.6: a) Robot attaches vertically to surface; b) Robot attaches horizontally to surface.

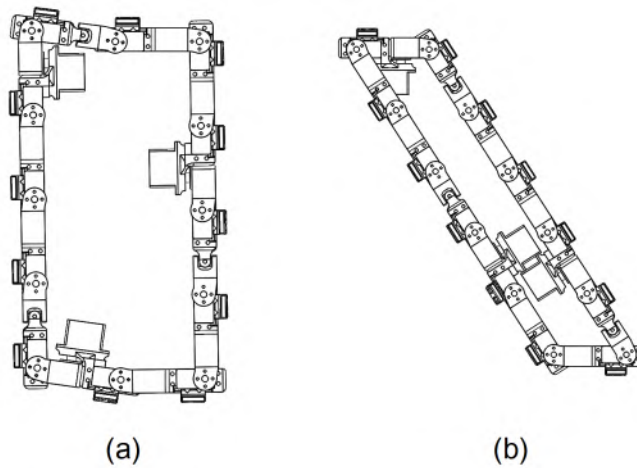


FIGURE 3.7: Robot shape in limitations a)  $h$  max; b)  $h$  min.

Following the proposed design,  $a = 5.2$  cm,  $b = 0.635$  cm, and  $l_1 = 28.75$  cm,  $l_2 = 19.47$  cm,  $l_3 = 9.1$  cm,  $l_4 = 1.27$  cm: 
$$\frac{Ph}{l_1 + l_2 + l_3 + l_4} < \frac{Ph}{2(a + b)}$$

To avoid turn-over failure, the magnetic force of the magnet block:  $F_{mj} > \frac{Ph}{2(a + b)}$

In different locomotions, the robot shape can be changed as illustrated in Fig. 3.7, which led to the change of  $h$  as well.  $F_{mj} > \frac{Ph}{2(a + b)}$  Fig. 3.7(a). Therefore, to avoid

both sliding and turn-over failures, the robot's magnetic force of each magnet block should satisfy:

$$F_{O_1}(j = 1 : n) > \max\left\{\frac{2.5P}{n}; \frac{Ph}{2(a+b)}\right\} \quad (3.3)$$

Following the proposed design,  $P = 30 \text{ N}$ ,  $h_{max} = 13 \text{ cm}$ ,  $n = 4$ .

$$F_{O_1}(j = 1 : n) > \max\left\{\frac{2.5 * 30}{4}; \frac{30 * 13}{2(5.2 + 0.635)}\right\} = 33.24(N) \quad (3.4)$$

### 3.3 Motor Torque Analysis

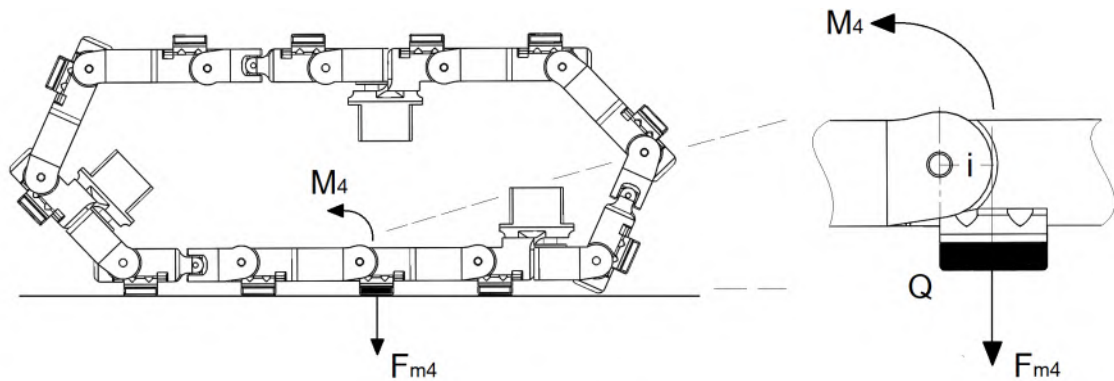


FIGURE 3.8: Magnet block position analysis.

The position of the magnet block is very important. It should be located in the position described in Fig.8. In both cases when  $i_1 \neq i$  (Fig. 3.9 and Fig. 3.10) the servo can not be optimal for the moment.

-  $i > i_1$  we can see  $x < x_1$ , which means servo 4 bears more load from  $F_{m1}, F_{m2}, F_{m3}$  when moving.

-  $i < i_1$ , the arm is longer, which makes a greater torque for the servo.

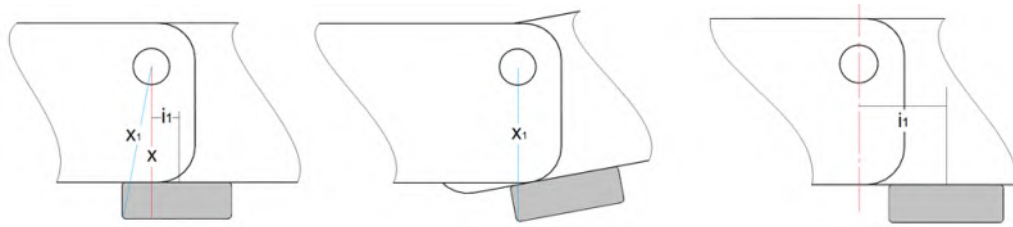


FIGURE 3.9: Magnet block position analysis.

In order to make the robot move, the force created by the servo should win the adhesion force of the last permanent magnet and the steel surface. As shown in Fig. 3.9, denote  $M$  as the torque of one motor,  $Q$  is the rotation fulcrum, and  $i$  is the arm from  $F_{mj}$  to  $Q$ . The required moment is satisfied:  $M_i > i * F_{mj}$ .  $i = 1.27$  cm, selected magnet force  $F_{mj} = 80$  (N) satisfied condition (1).  $M_i > 101.6$  (N.cm).

### 3.4 Experiment results

In order to measure the adhesion force created by the permanent magnet, we have set up an environment as follows. The robot's body - whose mass is  $m = 3$ kg - is placed on top of a flat steel surface while it is connected to a scale through an inelastic wire. We create a pull force onto the scale trying to lift the robot off the surface (similar setup to Fig. 13 in ??). At the time the robot is about to be off the surface, the force applied to the scale is equal to the sum of robot's weight and the magnetic pull force. Denote  $F_{pull}$  as the force we applied onto the scale,  $M$  is the value shown on the scale while  $P$  is the weight of robot's body, and  $F_{mag}$  is the magnetic force.

With  $g = 10m/s^2$ ,  $P = mg = 30N$  and  $F_{pull} = Mg = 10M$ , we can calculate magnetic adhesion force as follows  $F_{pull} = P + F_{mag}$  so  $F_{mag} = 10M - 3$  (N). The adhesion force measurement data is shown in Fig. 3.10 - 3.11.

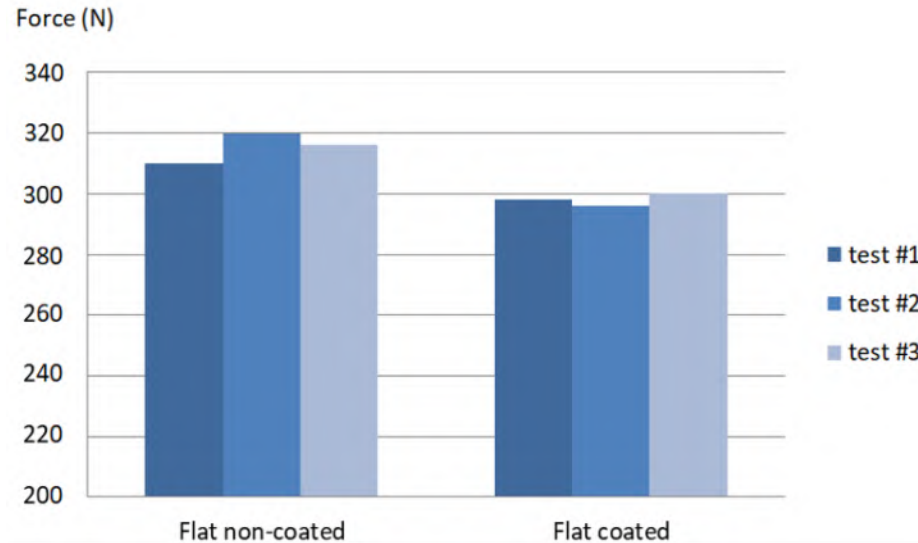


FIGURE 3.10: Adhesion force on flat surfaces.

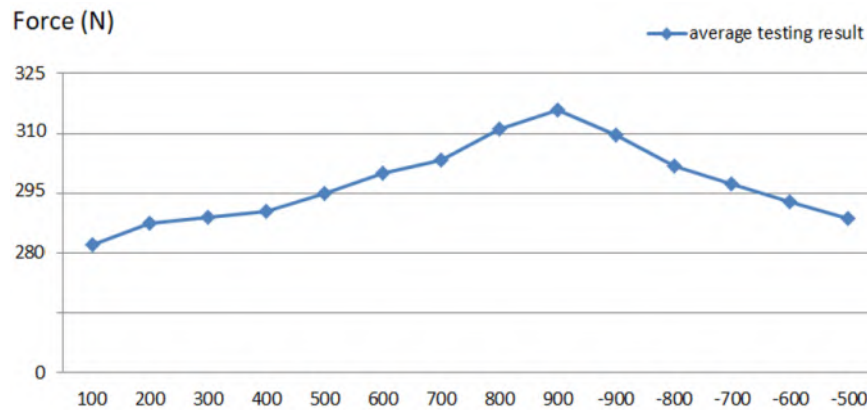


FIGURE 3.11: Adhesion force on curving surfaces with different radius.

From (1), the minimum adhesion force =  $n * F_{mj}$  (theory) =  $4 * 62.9 = 251,6$  (N).

From (3.2), the maximum adhesion force of robot =  $n * F_{mj}$  (selected) =  $4 * 80 = 320$  (N) as shown in Fig.3.10 - 3.11. The climbing tests were performed on both steel

structures and a steel bridge (Fig.3.12 - 3.13 - 3.14). In both cases, the robot was able to adhere strongly to the steel surface during its motion.



FIGURE 3.12: Robot test on an I-shape beam.



FIGURE 3.13: Robot test on a cylindrical beam.





FIGURE 3.14: Robot test on a curved surface.

### 3.5 Conclusion

This chapter discusses a new design of a climbing robot specifically for steel bridge inspection and evaluation. The robot has been designed based on the roller-chain concept to provide flexibility to the robot body, enabling it to climb smoothly on different steel structures and pass joints safely. The chapter provides a detailed description of the mechanical design and analysis of magnetic and motor forces. Experimental results conducted on different steel surfaces (flat, curving, and paint coated) have shown that the robot can adhere well and move safely while passing joints.



## Chapter 4

# Hybrid Mobile-Worming Robot

This chapter presents a practical climbing robotic system, which combines the methods and subsequently the advantages of some of the other steel inspection robots created previously. The robot can adapt to a wide range of different sorts of bridge surfaces (flat, curving, rough). The hybrid approach implemented in the robot in this chapter allows it to have both a mobile mode and a transforming mode (Fig. 4.2). These allow it to adapt to most complex steel bridge surfaces for efficient inspections. This robot utilizes adhesion force generated by permanent magnets in two modes; untouched magnets during mobile mode and touched for transforming mode. The flexible magnet array allows the robot to overcome obstacles including nuts and bolts. To demonstrate the robot's working principle, it has been deployed for climbing on indoor and outdoor steel structures and steel bridges.

## 4.1 Overall Design

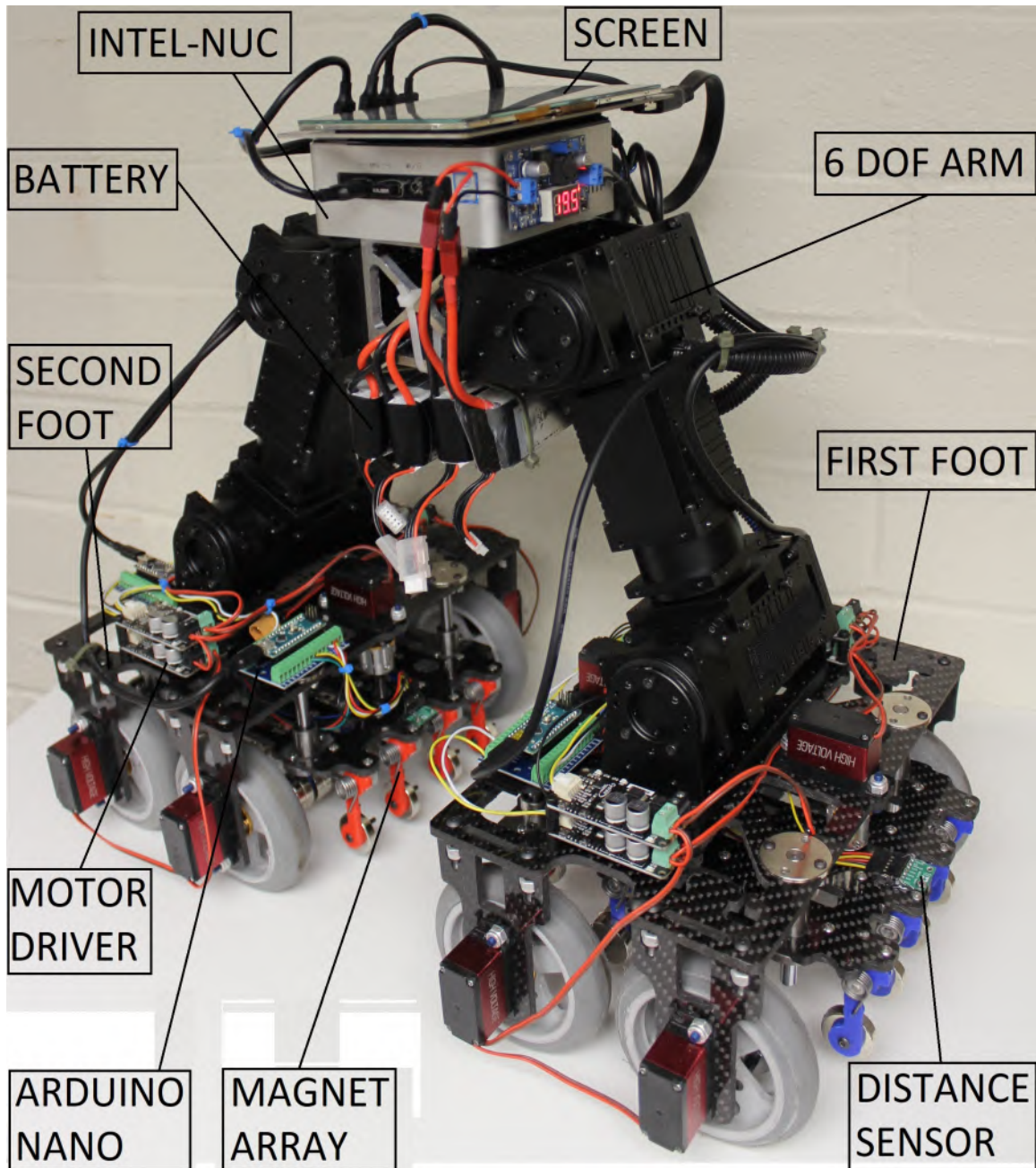


FIGURE 4.1: Overall design of robot.

The design concept of the hybrid climbing robot is illustrated in Fig. 4.1 and its function is described in Fig.4.2. The robot is divided into two main parts: the

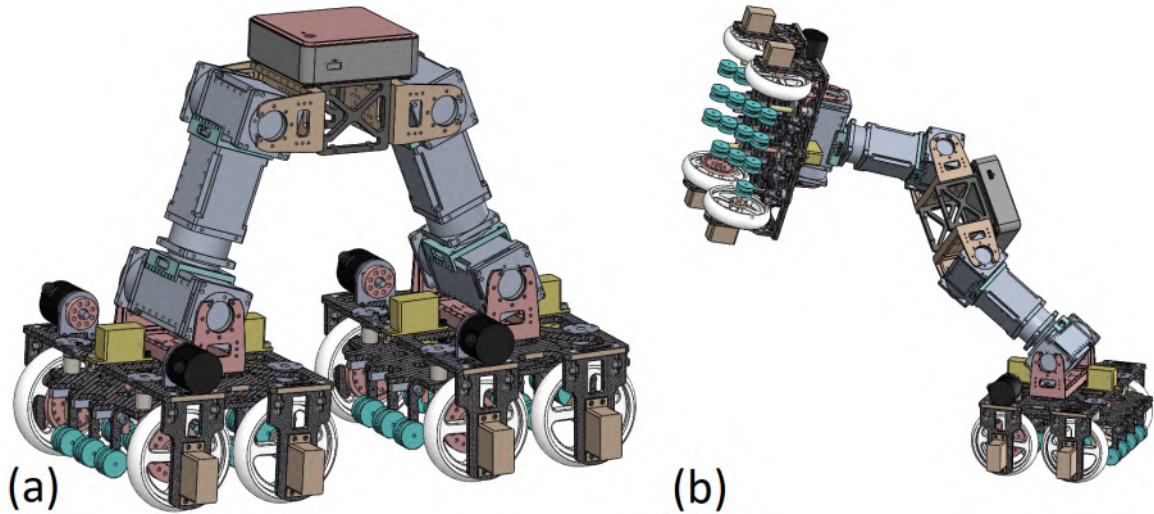


FIGURE 4.2: Robot function (a) Mobile mode; (b) Transforming mode, or worm mode.

feet and the body. Each foot is loaded with permanent magnets for adhesion force, therefore, allowing the robot to expend no energy for its continued attachment to steel surfaces. In mobile mode, the magnets hover in an untouched position with a 1mm distance from the steel surface. The magnets are ring-shaped and arranged in an array, which allows the robot to pass nuts and bolts smoothly while still maintaining a full adhesion force. The torsion spring is instrumental in the design of the feet, they allow every single magnet cell to individually adapt to varying external stimuli and then return to its initial structure. The magnets utilized in the array are magnetized through their diameter as opposed to through their thickness as shown in Fig. 4.3. This allows them to be more suitable for their design purpose.

The distance between the magnet arrays and the surface is controllable, and each foot is able to work in touched or untouched orientations. Two parallel feed screws are utilized with an actuator to enable the control system to modify the distance that

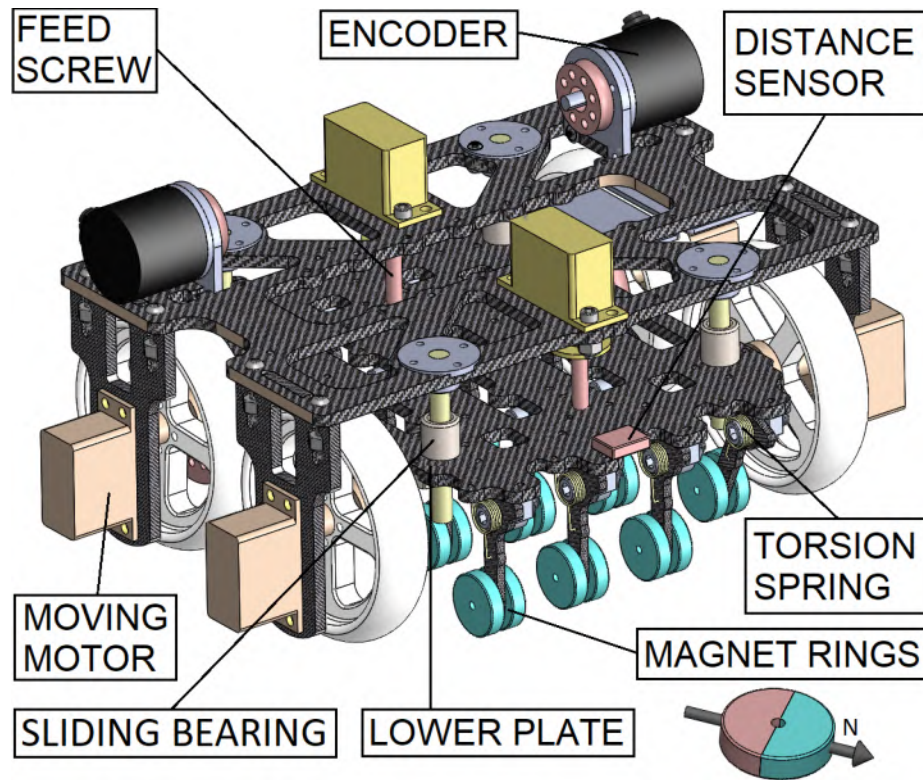


FIGURE 4.3: The robots foot with flexible magnet array.

each foot is kept. Feedback from a distance sensor helps to ensure that the magnet arrays are kept at an optimal distance. The four wheels on each foot keep the robot stable when standing on one foot and support large moments while simultaneously being lightweight. The rubber wheels maximize the friction factor between the robot and the surfaces that each foot adheres to. The foot design allows the ARA robot to function on different surface conditions as described in Fig.4.4. The body has 6 degrees of freedom (DOF) and functions like a robot arm shown in Fig.4.5 when the robot is in transforming mode.

When the robot encounters an area it is having difficulties traversing while in mobile mode, the robot will alter the magnet orientation of one foot to touch so that the



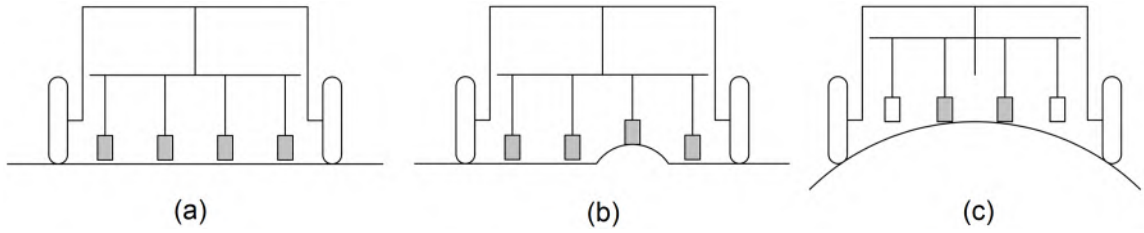


FIGURE 4.4: (a) The robot on flat surface; (b) The robot passing nuts; (c) The robot on a curving surface.

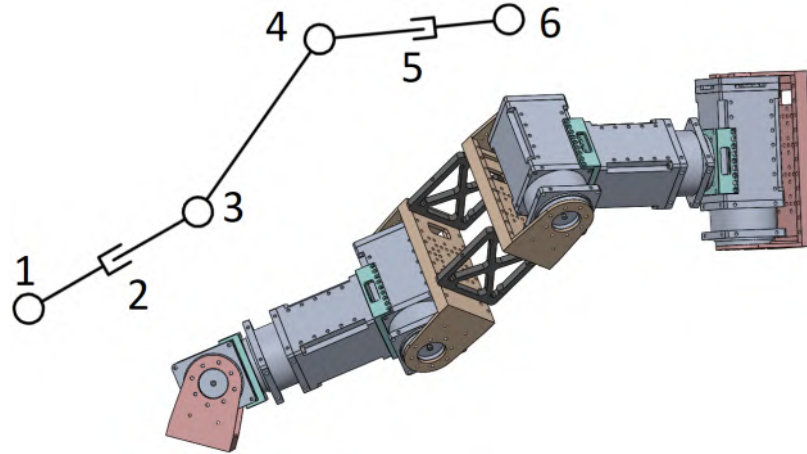


FIGURE 4.5: The robot body - 6 DOF robot arm.

robot may shift into transforming mode to find a new surface to travel along and complete its task. In transforming mode, one foot's magnet array will touch fully to the surface to maximize its adhesion force. Then the magnets on the second foot will move up to release the adhesion force. Now, the robot works as a 6 DOF robot arm. When touching a new surface, the process happens again to the opposite feet. This enables the robot to move the whole robot to a new place. The whole process is shown in Fig. 4.6.

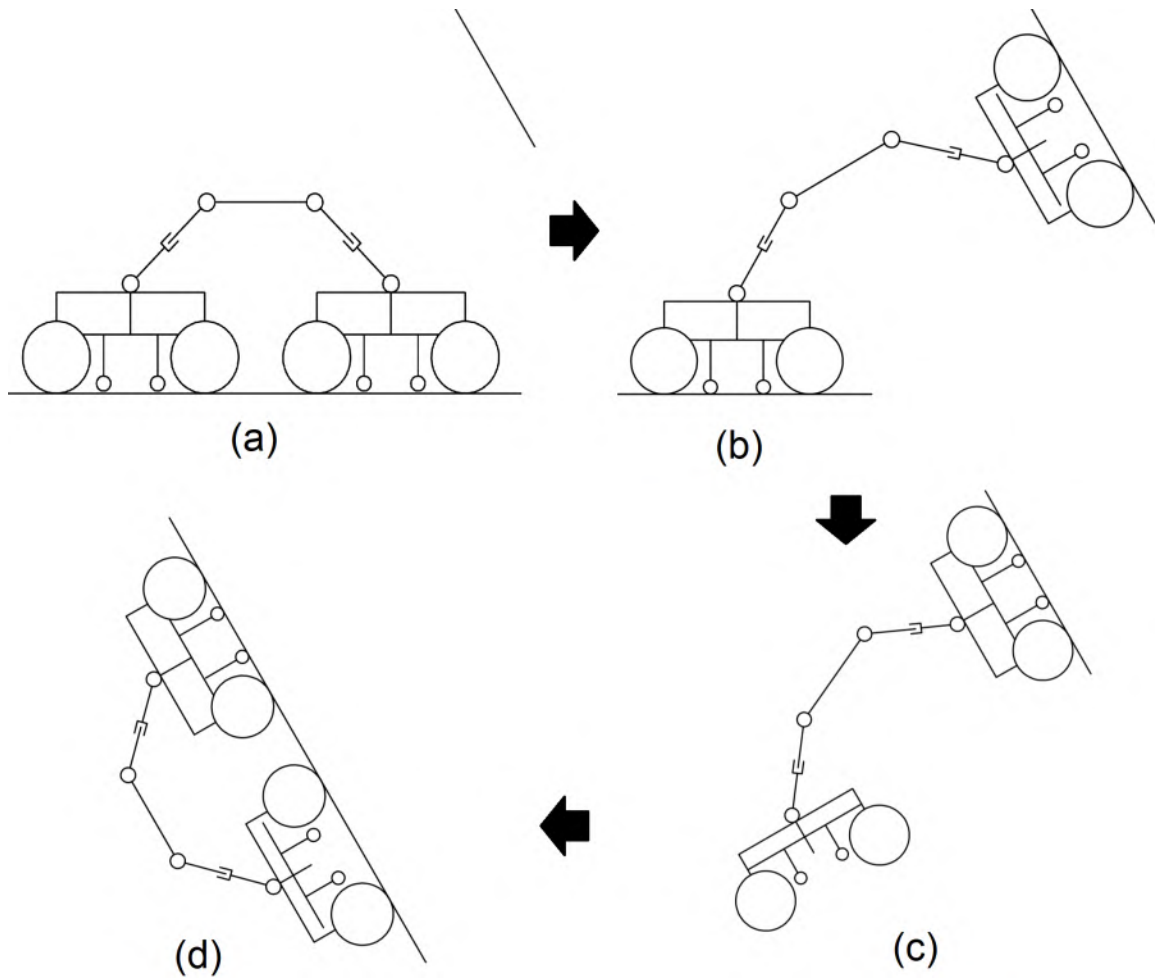


FIGURE 4.6: Transformation process: (a) The robot in mobile mode; (b) The robot makes the magnet array touch on the 1st foot and looks for new a new surface with the other; (c) The 2nd foot touches a new surface and moves the rest of the robot there; (d) The robot switches back to mobile mode on the new surface.

## 4.2 Mechanical Design and Analysis

Throughout the design process of this robot, the ARA team performed an extensive set of statics analyses on the robot. These examinations into the mechanical behaviors behind which this robot has been constructed have allowed the ARA team to design and manufacture a robot, which surpasses the current capacities of other steel bridge

inspection robots that came before it such as CROC [35], the inchworm inspired robot or MINOAS [26].

### 4.2.1 Transformation Analysis

The purpose of the transformation analysis was to determine the maximum moment the robot would experience under static conditions. This evaluation allowed us to determine the moment the robot experiences when transforming and the minimum torque required from our servos to overcome the force of gravity.

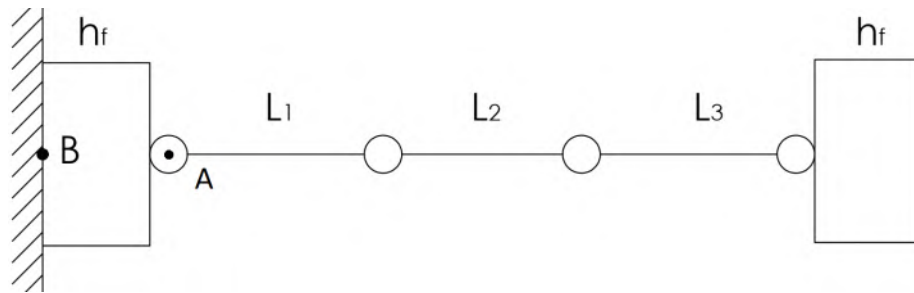


FIGURE 4.7: Extended statics diagram.

Variable  $h_f$  represents the height of the feet, and  $m_f$  is the mass of the foot.  $L_1, L_2, L_3$  are the lengths of links, one through three.  $m_e$  is the mass of equipment that the robot is carrying.  $m_{L1}, m_{L2}, m_{L3}$  are the masses of their respective links.  $g$  is for gravity.

First, the moment acting at point  $A$  in Fig. 4.7 was determined in order to obtain a generic equation Equ. (4.1) to model the torque output required from a servo at point  $A$  as a function of the variables above. After this, the ARA team could decide upon a particular servo to use in the construction of the proposed robot.

$$\begin{aligned}
T_A = & \left(\frac{1}{2}L_1\right)m_{L1}g + \left(L_1 + \frac{1}{2}L_2\right)(m_{L2} + m_e)g \\
& + \left(L_1 + L_2 + \frac{1}{2}L_3\right)m_{L3}g \\
& + \left(L_1 + L_2 + L_3 + \frac{1}{2}h_f\right)m_f g.
\end{aligned} \tag{4.1}$$

The moment the robot experiences when fully extended was determined in this analysis which informed the team about how large the moment acting upon the robot would be through Equ. (4.2). In the Turn Over and Sliding Friction Analysis section later in this chapter, we take the results of this study and use them as input for the external moment that the foot is experiencing in the Turn Over Analysis.

$$\begin{aligned}
M_B = & \left(\frac{1}{2}h_f\right)m_f g + \left(h_f + \frac{1}{2}L_1\right)m_{L1}g \\
& + \left(h_f + L_1 + \frac{1}{2}L_2\right)(m_{L2} - m_e)g \\
& + \left(h_f + L_1 + L_2 + \frac{1}{2}L_3\right)m_{L3}g \\
& + \left(\frac{3}{2}h_f + L_1 + L_2 + L_3\right)m_f g.
\end{aligned} \tag{4.2}$$

In both the Moment and Torque equations (4.1) and (4.2), the mass of the feet plays a very large role in how large the respective acting moment and torque are. When we performed this analysis using aluminum as the material for the structural members of the robot, we found that our robot needed a very significant amount of torque to overcome gravity. From this, we concluded that our servos would have very low factors of safety. One of the ways in which the ARA team addressed this issue



was by changing the material with which the structural members of the robot were manufactured, choosing carbon fiber instead of aluminum.

The reduction of the total mass in the feet gives our robot a much larger factor of safety to subsequently operate in a much more desirable manner. This reduction in mass (-40%) enables our robot to traverse steel structures because its servos can hoist the robot and hold still or overpower the force of the moments acting on them. This means that the ARA robot is able to carry more equipment than it would have been able to if it was manufactured from aluminum.

#### **4.2.2 Turn Over and Sliding Friction Analysis**

At this point in the design process, the ARA team needed to conclude whether our robot would be at risk of toppling over or slipping while in use. To do this, we performed two more statics analyses, one, on an adhered foot with an external moment acting on it and the other as a stationary foot adhered to a steel surface resisting sliding.

Our turnover analysis (Fig. 4.8a) builds off of the transformation analysis by using the proposed moment function Equ. (4.2) as an input to the external moment acting upon the foot in this analysis. In order to determine how much adhesion force was required by each foot, a moment was taken at point  $C$ , this produced equations (4.3) and (4.4).

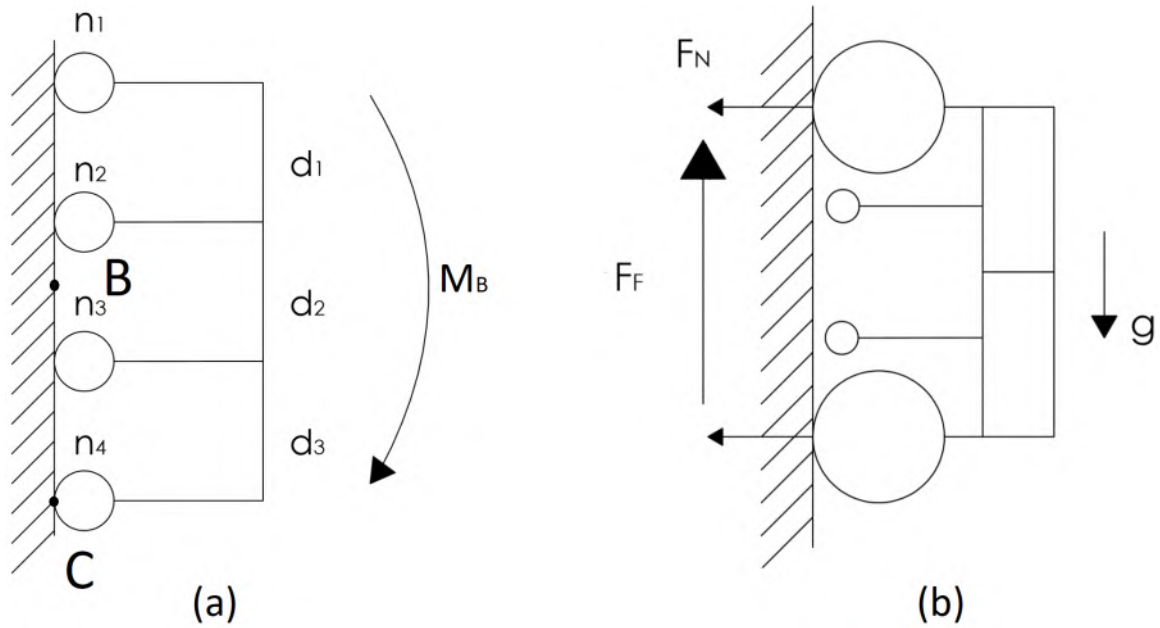


FIGURE 4.8: Turn over/adhesion diagram.

Variables  $n_1, n_2, n_3, n_4$  represent the number of magnets in each row.  $M_C$  is the moment at point  $C$ , and  $F_{mag}$  is the force created by each magnet.  $d_1, d_2, d_3$  all represent distances, where  $M_B = f(h_f, m_f, m_{L1}, m_e, m_{L2}, m_{L3}, L_1, L_2, L_3, g)$ , is solved for in the Transformation Analysis subsection of this chapter.

$$\begin{aligned}
 M_c = -M_B + F_{mag}n_3d_3 + F_{mag}n_2(d_2 + d_3) \\
 + F_{mag}n_1(d_1 + d_2 + d_3).
 \end{aligned}
 \tag{4.3}$$

Equ. (4.3) was then simplified and adjusted to emphasize the role magnet strength and each distance would have upon the net moment,  $M_C$ , giving Equ. (4.4).

$$\begin{aligned}
 M_c = F_{mag}(d_3(n_1 + n_2 + n_3) + d_2(n_1 + n_2) \\
 + d_1 n_1) - M_B = -M_B + F_{mag} n_3 d_3 \\
 + F_{mag} n_2 (d_2 + d_3) + F_{mag} n_1 (d_1 + d_2 + d_3).
 \end{aligned} \tag{4.4}$$

The resulting equation Equ. (4.4) helped develop a better understanding of the importance of foot orientation, the location of magnets, and the power of the magnets in the design. This analysis was also instrumental to the design layout of each of the feet in our robot and helped to ensure that the robot would maintain its position on steel structures.

The sliding friction analysis (Fig. 4.8b) assumes static conditions to determine what the required force of friction acting on the wheels is to prevent sliding. The main purpose of these calculations was to ensure that the robot's feet would not slide down the steel surfaces that they adhered to.

$i$  represents the number of wheels that the normal force ( $F_N$ ) is distributed between, and  $n$  is for the total number of permanent magnets on the foot.  $F_F$  is the friction force, and  $F_{mag}$  is the force generated by one magnet.  $\mu$  represents the friction coefficient between steel and rubber. For the purposes of our study, we used a value of 0.7 [84].

This evaluation begins by defining the equation for the normal force acting perpendicular to the surface that the robot is adhered to; Equ. (4.5).

$$F_N = \frac{nF_{mag}}{i}. \quad (4.5)$$

Then, a base equation is written to solve for the force of friction acting against the motion, Equ. (4.6).

$$F_F = iF_N\mu. \quad (4.6)$$

Which when both combined, yields Equ. (4.7).

$$F_F = nF_{mag}\mu. \quad (4.7)$$

Equ.(4.7) models the force of friction as a function of the total number of magnets on the foot, the friction coefficient based on the materials in contact, and the force generated by one magnet.

### 4.3 Robot Deployment

The purpose of the indoor testing was to evaluate the robot's climbing abilities (Fig. 4.9) and examine how adhesion force varied with distance from the steel surface.

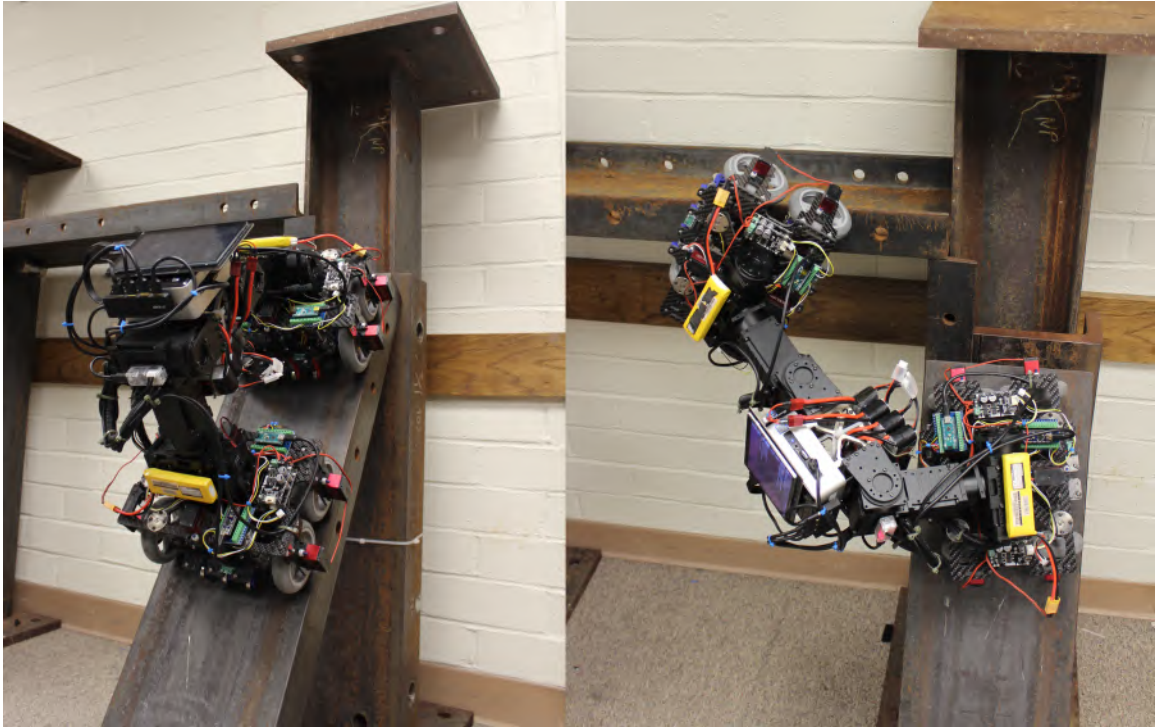


FIGURE 4.9: The robot tests on a steel structure indoors.

The ARA Labs robot was able to successfully climb the lab's steel beams (Fig. 4.9). With the ARA robot's climbing capabilities verified, the robot was then tested outside on more complex structures than what could be found in the lab.

Outdoor testing for the robot began at a local steel art statue on the university campus famous for having every commercial steel link type on it, as showcased in Fig 4.10.

At this art statue, the team was able to examine the robot's physical ability to traverse the complex geometries, which would come across out in the world as shown in Fig. 4.10. The results from this assessment and verification subsection showcase the ARA Lab robot's proposed ability to get around and traverse complex, jagged geometries like those found on the art statue, Fig. 4.10. The testing at this art statue suggests

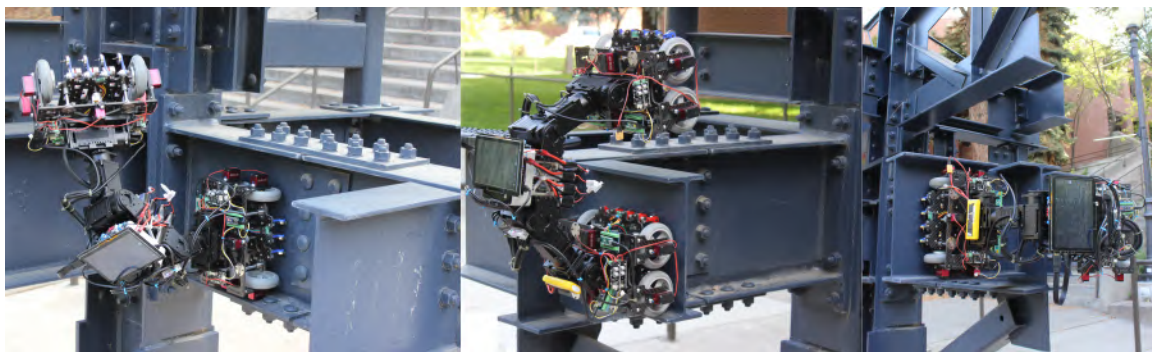


FIGURE 4.10: Deployment of the robot on a steel structure.

that more work should be put into creating friction to resist twisting while the robot is in worming mode. While not entirely crippling, the robot did struggle to maintain its orientation when moving. This issue was also likely exacerbated by a rudimentary controller design, which creates sharp, sudden movements that ended as quickly as they began. Smoothing of the accelerations created by the servos will be imperative in ensuring this robot is capable of meeting commercial demands for steel structure inspection.

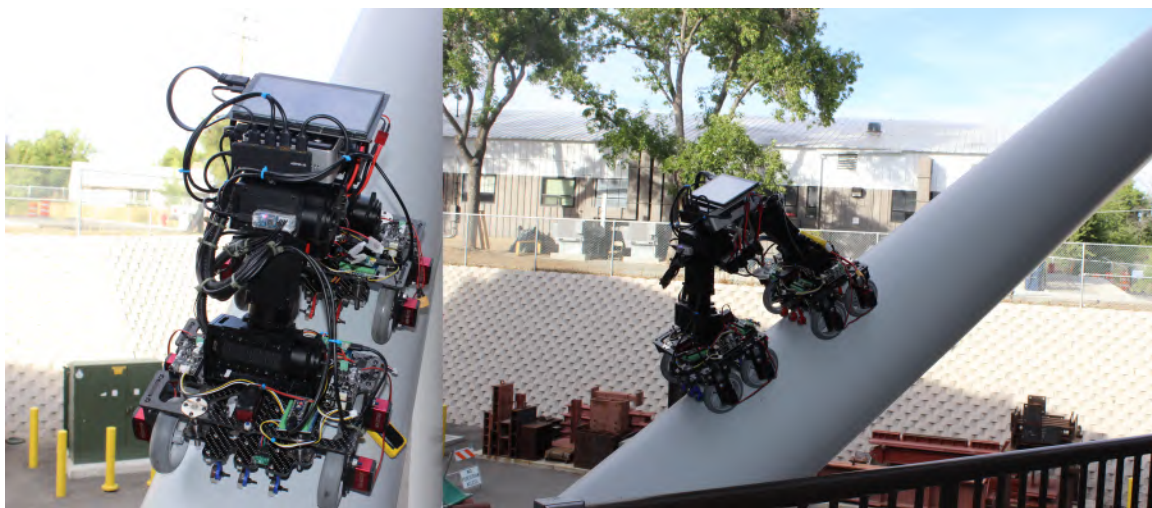


FIGURE 4.11: Mobile mode example on bridge.

Additional evaluations were done at a bridge on campus, which is comprised of long

cylindrical members. As shown in Fig. 4.11, these members were useful for testing the robot's ability to adhere to round surfaces.

Link to the video demonstration of the robot deployments can be seen here: <https://youtu.be/PwDf6h00m3c>

## 4.4 Conclusion

The proposed inch-worm robot described in this chapter proposes a design, which combines the best parts of other modern-day steel inspection robots in order to traverse the complex geometries commonly found on steel structures such as windmills, steel bridges, and buildings. The largest challenge so far in this project has been making sure that the robot will function as intended. Since the team is implementing a design, which draws from a wide range of other designs, the robot needs to be able to accommodate all of the design parameters for each design in order to maintain the intended functionalities of the implemented features. This created a necessity for detailed design analyses to ensure that such an amalgamation of various designs could successfully work together in unison.

## Chapter 5

# Multi-directional Bicycle Robot

This chapter presents a novel two-wheeled climbing robotic system to provide an efficient inspection solution for complex steel structures. We focus on optimizing the climbing capability and the multi-directional locomotion of a bike-like wheeled-climbing robot, making it maneuver on complex ferromagnetic structures. We also developed a transforming mechanism enabling the robot to reconfigure to overcome concave and convex-edged obstacles such as L-, T-, and I-shaped beams or thorny corners/edges. Robot architecture allows us to equip a sensor deploying mechanism for both an ultrasonic-based steel thickness measurement sensor and a camera in the most space-efficient package. This study is a full and upgraded version evolved from our initial prototypes [85] and [86]. This upgraded version has improved robot stability when traversing horizontally on cylindrical structures by generating new a locomotion



mode. Moreover, a simpler but more efficient method of a flexible material in contacting part helps enhance the sensor deploying mechanism function. We demonstrated the robot's working principles and functionalities through laboratory and field tests. Video of this deployment can be seen from the Advanced Robotics and Automation (ARA) Laboratory's website at this link: [https://ara.cse.unr.edu/?page\\_id=11](https://ara.cse.unr.edu/?page_id=11)

The rest of the paper is organized as follows. Section 5.1 describes the overall robot design. Section 5.2 presents a detailed mechanical design and magnetic force analysis of the robot when moving on surfaces with different inclinations. Section 5.3 analyzes magnetic force on different surface curvatures under both static and dynamic conditions. Section 5.4 demonstrates various experiments to verify the proposed robot design and validate the magnetic force analysis, robot locomotion, and transformation. Finally, the conclusion and discussion of future work are presented in Section 6.5.

## 5.1 Overall Design

The front view and the back view of the robot are depicted in Figure. 5.1a. We add a thickness transducer in the space between the two wheels. This location is ideal for protecting the sensor when traveling and allows good contact for measurements, whether the robot is working on flat or curved surfaces. A detailed description is

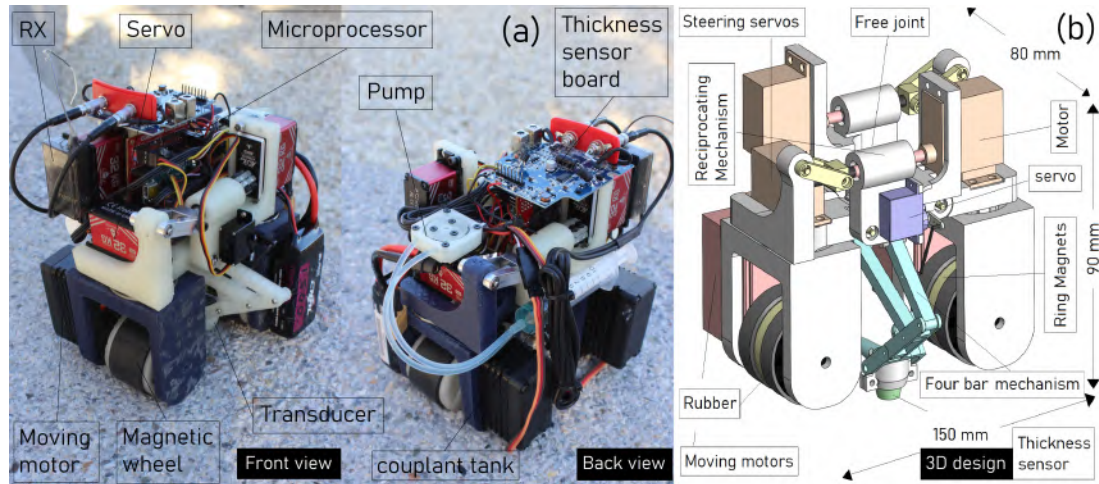


FIGURE 5.1: (Left) The front and back view of the robot. (Right) The 3D design model of the robot.

shown in Figure. 5.6. The robot's mass is 1.2kg, including the sensor. We use 3D-printed ABS plastic to manufacture the frame for a lightweight robot. When powered by a 700mAh LiPo battery, a human operator can remotely control the robot to work for 30 minutes. Figure. 5.1b shows the overall mechanical design of the robot. The robot's dimension is 150mm  $\times$  80mm  $\times$  90mm. We place the ring magnets at the cores of the two rubber-covered wheels, driven by two high-torque gear DC motors (100kg-cm torque each). The steering actuators and transforming mechanisms are controlled by two servos (32kg-cm torque each). The front and the back of the frame are linked by a bearing acting as a dynamic joint.

For high mobility, two revolute joints are installed, making two steering units (Figure. 5.2). These two units allow the robot to work in two modes: bicycle-like and multi-steering modes. The bicycle-like mode is utilized when the robot operates on large surfaces with only one activated steering unit (Figure. 5.2a). On narrow surfaces, the robot can change the direction by activating the rear steering unit instead of the

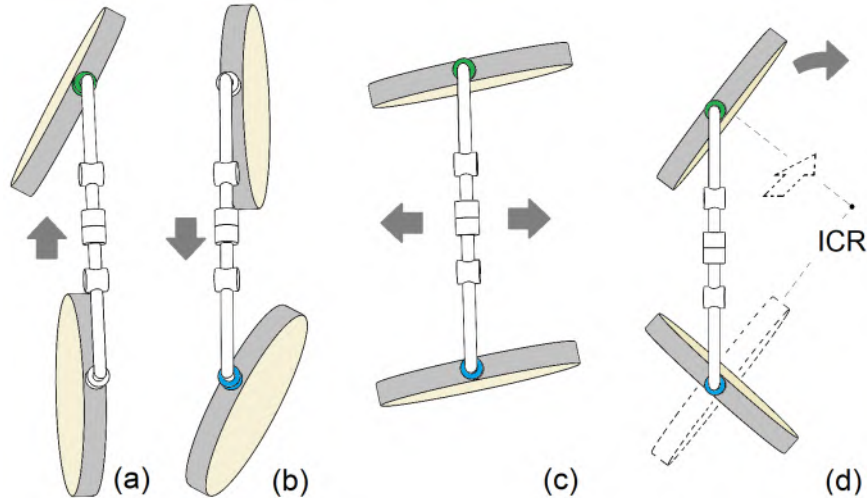


FIGURE 5.2: The design concept shows the maneuverability of our robot with active joints colored green (for the front joint) and blue (for the rear joint). Two independent steering actuators allow the robot to enable bicycle-like moving modes (a) when only the front steering unit is activated and (b) when only the rear steering unit is activated to change direction on narrow surfaces. (c) Two steering units are activated simultaneously; the robot can move sideways. (d) The mix of bicycle and multi-directional modes. On horizontal traversing, the bicycle shape is weak in maintaining adhesive torque. This mode improves this disadvantage with wheel paralleling configuration but is still able to turn.

front one (Figure. 5.2b). In locations that require sideway movements, the multi-directional mode is enabled. In this mode, two steering units are active simultaneously as in Figure. 5.2c. The maximum turning angle is kept at less than 90 degrees to maintain the robot's stabilization in this mode. In an extreme situation when a robot traverses horizontally on cylindrical structures, adhesive torque decrease significantly. The mix of bicycle and multi-directional mode Figure. 5.2d is switched to enhance safety.

In addition, a free joint (orange joint in Figure. 5.3) working as a dynamic connection between two halves of the robot's body allows the two wheels to stick to surfaces effectively, even uneven ones such as two flat curvatures (Figure. 5.3a), positive

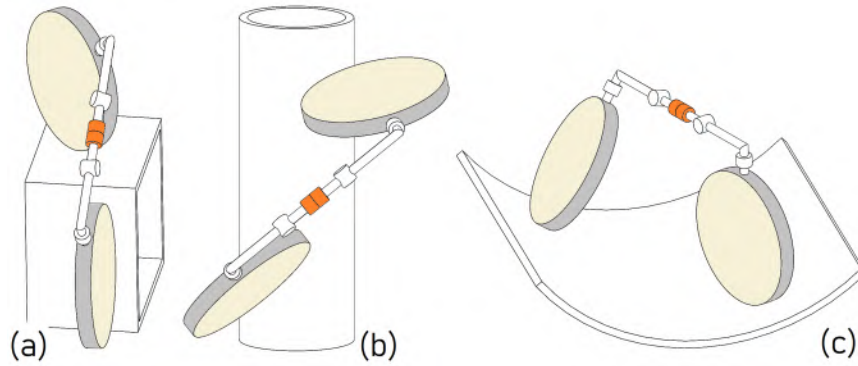


FIGURE 5.3: The free joint (orange) in the middle of the robot's body helps its wheels to better adhere to uneven surfaces, e.g., a) two flat curvatures, b) positive curvatures, c) negative curvatures.

curvatures (Figure. 5.3b), or negative curvatures (Figure. 5.3c). Our design also enables the robot to pass thin edge and acute corners with two other revolute joints shown in Figure. 5.4. These two joints allow the distance between the two wheels to be adjustable based on surfaces as shown in Figure. 5.4c and Figure. 5.4d.

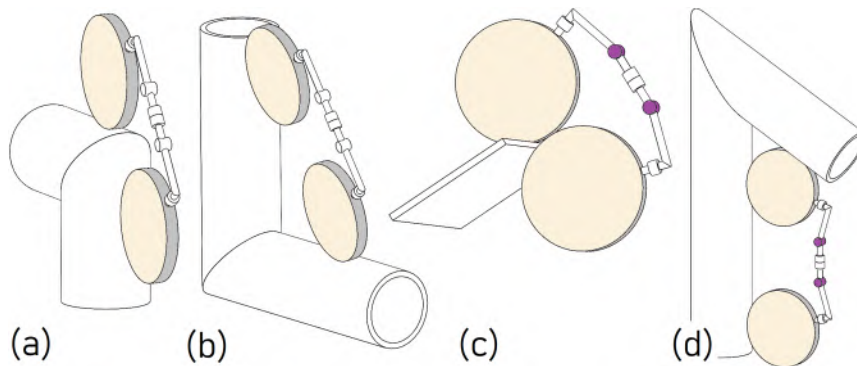


FIGURE 5.4: Our design allows the distance between the two wheels to be adjustable with two revolute joints. The robot can pass corners without activating the two joints in normal conditions (a), and (b). However, the robot can adjust the wheels' distance (the two joints are activated, hence colored purple) to be small to pass a thin edge (c) or big to pass an acute corner (d).

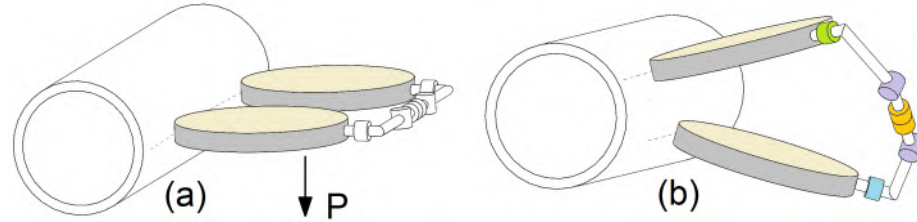


FIGURE 5.5: Robot configuration when traveling in an extreme situation (horizontal traverse on a cylindrical structure). a) the robot in high risk of losing adhesive force in normal bicycle mode, b) the robot is in fourth mode Figure 5.2d that significantly improves adhesive torque to keep the robot safe in this situation.

## 5.2 Mechanical Design and Analysis

This section provides a detailed mechanical analysis of our robot, including the analysis of the robot transformation, the robot maneuverability, and the sensor deployment mechanism.

### 5.2.1 Robot Transformation Analysis

We use reciprocating mechanisms to allow the distance between the two wheels to be adjustable. Due to the high load of attractive force when the two wheels are close, a feed screw is applied for the slider-crank part. The mechanism can transform the robot into three different shapes depending on particular situations, as shown in Figure. 5.6.

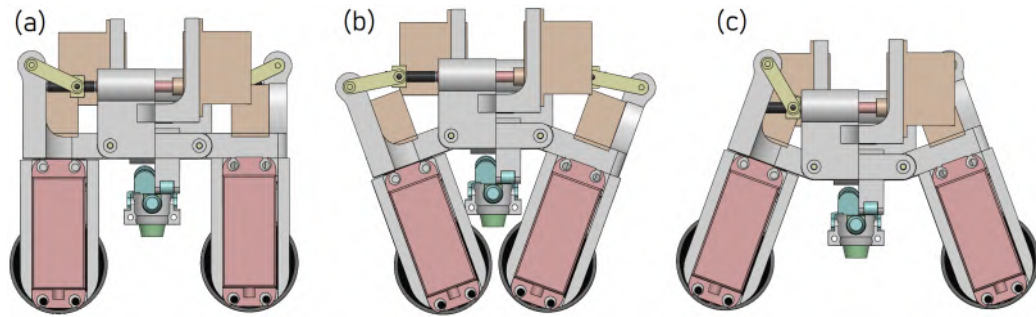


FIGURE 5.6: The robot's shape when applying reciprocating mechanisms. a) in normal conditions, b) when passing thin edges, and c) when passing acute internal corners. The sensor and deploying mechanism position do not affect to transforming function. It also enables the sensor always be perpendicular to measuring surfaces even if they are curved.

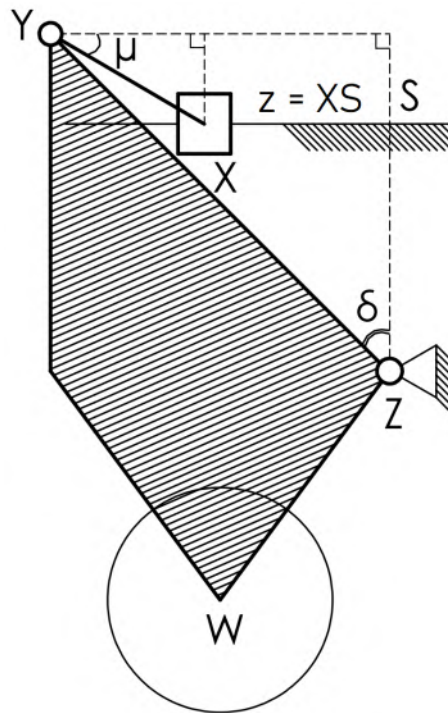


FIGURE 5.7: The reciprocating mechanism's kinematic.

### 5.2.1.1 Kinematic Analysis

The kinematic is analyzed in Figure. 5.7, where W is the wheel center, reciprocating mechanism XYZ, and  $z = XS$ , we have:

$$XY \sin \mu = XY \cos \delta - SZ, \quad (5.1)$$

$$XY \cos \mu = XY \sin \delta - z. \quad (5.2)$$

Square then sum both sides of (5.1) and (5.2), we have:

$$XY^2(\sin^2 \mu + \cos^2 \mu) = (XY \cos \delta - SZ)^2 + (XY \sin \delta - z)^2. \quad (5.3)$$

Simplifying (5.3) produces:

$$SZ \cos \delta + z \sin \delta = \frac{z^2 + YZ^2 + SZ^2 - XY^2}{2XY}, \quad (5.4)$$

resulting in a function  $\delta = f(z)$ .

### 5.2.1.2 Force

The robot's shape transformation is the combination of controlling  $\delta$  in Fig. 5.8 and moving wheels simultaneously. The load (the magnetic force between the two wheels) is shared between the two wheels and the reciprocating mechanism. From Figure. 5.8,

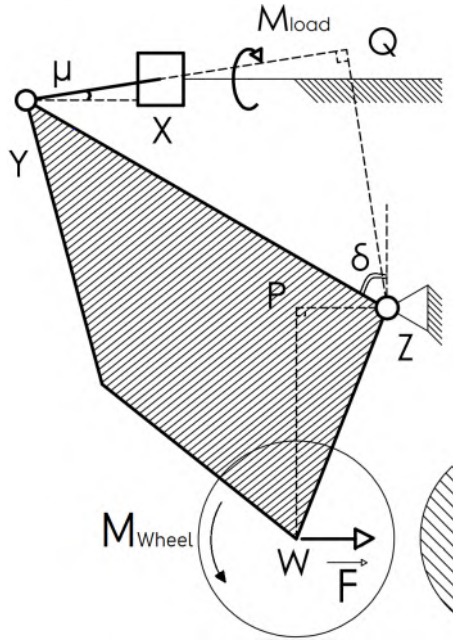


FIGURE 5.8: Force analysis of the reciprocating mechanism.

with  $F$  as the attractive force between the two wheels,  $M_{\text{load}}$  is the torque that feeds screw bears, and  $i$  is the feed screw's transmission ratio, we have:

$$M_{\text{load}} = F \frac{PW}{QZ \cos \mu} i - M_{\text{wheel}}. \quad (5.5)$$

## 5.2.2 Robot Maneuverability Analysis

### 5.2.2.1 Adhesive Force

We analyze the adhesive force that the robot needs to climb reliably in any normal working conditions. We perform the analysis in an extreme situation where the adhesive force between the magnetic wheels and the contacting structures is minimal Figure. 5.9. Here,  $X_1$  and  $X_2$  are two contact points of the back wheel and front



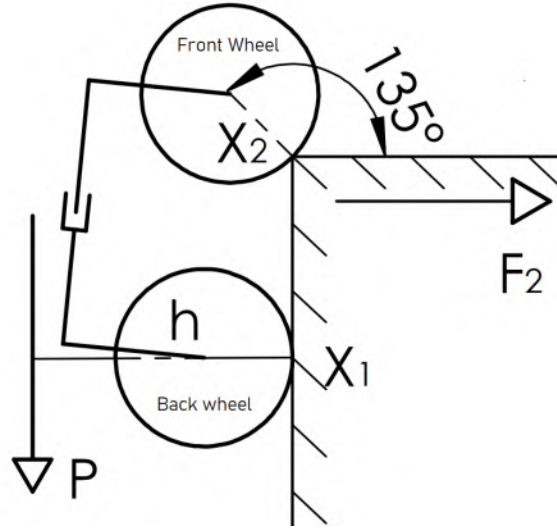


FIGURE 5.9: A situation where the adhesive force is minimal, resulting in a high chance of falling over. In this case, the adhesive force of the front wheel is significantly reduced when the robot hits an edge.

wheel, respectively. We call  $P$  the robot's weight, and  $h$  is the distance from the center of mass of the robot to  $X_1$ . If  $F_2$  is an adhesive force of the front wheel at  $X_2$  then  $F_2$  is at its minimum when the front wheel hits the corner. To keep the robot safe, the following condition needs to be satisfied:

$$F_2 \cdot X_1 X_2 > Ph \rightarrow F_2 > \frac{Ph}{X_1 X_2}. \quad (5.6)$$

According to ISO 3691, [87] for safe weight lifting, a safety factor of 5 was selected. Therefore, the real adhesive force  $F_2$  needs to be at least five times greater than the result from the above theoretical calculation in (6.4).

### 5.2.2.2 Extreme Locomotive Situations

This analysis calculates the necessary motor torque when the robot stands the highest load. The highest load occurs when the robot passes an internal corner between two perpendicular surfaces (Fig. 5.10), the front wheel bears an additional force  $F_{2,2}$ , which is the adhesive force of the front wheel on the surface 2. Similarly,  $F_{2,1}$  is the adhesive forces of the front wheel on surface 1.  $F_{f2}$  is the friction of the front wheel on surface 2,  $r$  is the wheel's radius,  $k$  is the static friction coefficient (between rubber and steel in our design). The minimum force of the front wheel that allows the robot to be able to overcome the corner must satisfy:

$$\frac{M_{\text{moving}}}{r} > F_{2,1} + F_{f2} + \frac{P}{2}. \quad (5.7)$$

Therefore, the moving motor torque needs to satisfy:

$$M_{\text{moving}} > r(F_{2,1} + kF_{2,2} + \frac{P}{2}). \quad (5.8)$$

According to IEC 60034, [88], the actual torque selected is at least double that of theoretical calculation in (5.8).

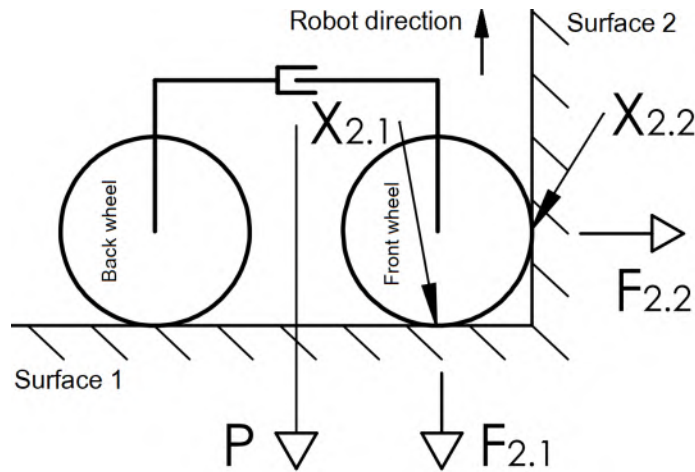


FIGURE 5.10: When the robot passes an internal corner between two perpendicular surfaces, the robot's load increases significantly.

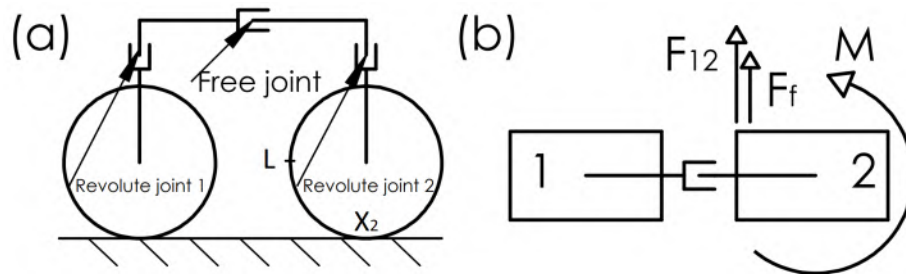


FIGURE 5.11: An experiment is conducted to investigate the load on a steering servo motor. A dynamometer is mounted on one wheel's edge (point  $L$ ) to measure the load. The distance from  $L$  to the rotating point  $X_2$  is  $r$  (the wheel's radius).

a) Side view. b) Top view.

### 5.2.2.3 Steering

An analysis is conducted to investigate the load torque on the revolute joints. Two forces affect each other as illustrated in Figure. 5.11: the static friction and the attractive force at the two magnetic wheels. Let  $F_{12}$  be the adhesive force of wheel 1 affecting wheel 2, and  $F_f$  be the friction at  $X_2$ . The measured load-force at point  $L$  (Figure. 5.11a) has to satisfy the following condition:

$$F_{12} + F_f < \frac{M_{\text{steering}}}{r}. \quad (5.9)$$

Thus, the steering servo torque needs to satisfy:

$$M_{\text{steering}} > r (F_{12} + k (F_2 + P)). \quad (5.10)$$

Based on IEC 60034 [88], the actual servo's torque is chosen to be at least two-fold compared to that of theoretical calculation in (5.10).

#### 5.2.2.4 Horizontal Traversing

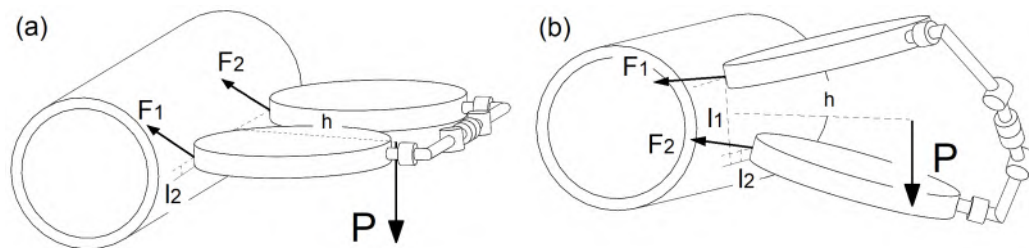


FIGURE 5.12: a) robot shape is in conventional bicycle mode b) robot transforms into the mixed mode to improve safety factor in extreme situations

This analysis provides a solution when fulling torque dramatically reduces when the robot travels horizontally on a cylindrical structure Figure. 5.12a. Because crank  $l_2$  is short, the torque to keep the robot avoid turnover is weak as below:

$$(F_1 + F_2)l_2. \quad (5.11)$$

To improve the safety factor in this situation, the robot should transform to the mixed mode as Figure. 5.2d. Crank  $l_1$  is much longer than  $l_2$ . so the fulling torque becomes:

$$Ph = F_1l_1 + F_2l_2. \quad (5.12)$$

### 5.2.3 Sensor Deployment Mechanism Analysis

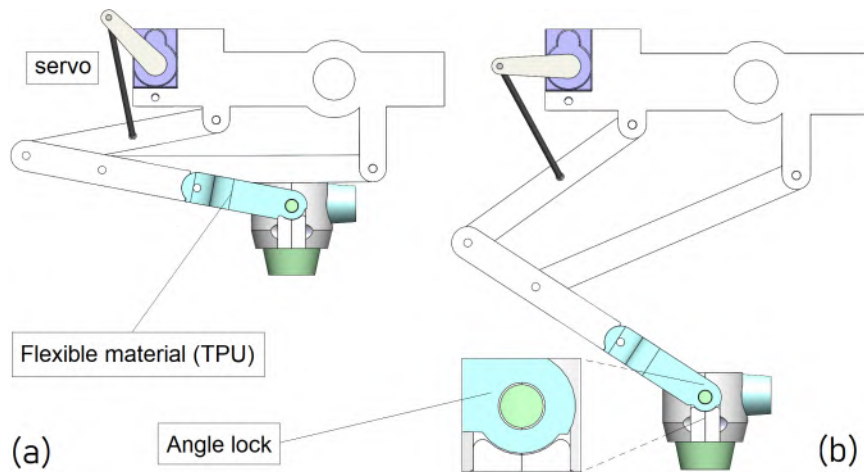


FIGURE 5.13: The four-bar mechanism. A flexible part (TPU) acts as a soft contact between the probe and surfaces. An angle lock is added to create a range of free movement of the probe when approaching uneven surfaces.

A four-bar mechanism is designed for generating vertical movements of the transducer, as shown in Figure. 5.13. A compression spring is added together with an angle lock to avoid the overload of servo motors and enhance contact between the transducer and the working surfaces.

We analyze the mechanism using a simplified model shown in Figure. 5.14. This figure shows that the target four-bar linkage ACDB can be considered a special mix of ACE and BDE reciprocating mechanisms, with the same virtual slider E.

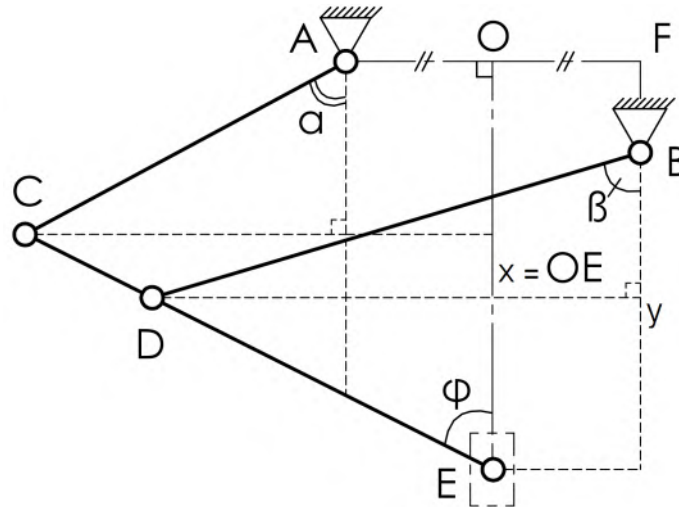


FIGURE 5.14: The four-bar mechanism's kinematic.

### 5.2.3.1 ACE Analysis

From Figure. 5.14, we have:

$$CE \cos \varphi = x - AC \cos \alpha, \quad (5.13)$$

$$CE \sin \varphi = AO + AC \sin \alpha. \quad (5.14)$$

Applying the similar approach as in (5.1) and (5.2) for (5.13) and (5.14), we have:

$$x \cos \alpha - AO \sin \alpha = \frac{x^2 + AO^2 + AC^2 - CE^2}{2AC}. \quad (5.15)$$

We see that (6.7) presents a function  $\alpha = f(x)$ .

### 5.2.3.2 BDE Analysis

From Figure. 5.14:

$$BD \cos \beta = x - BF - DE \cos \varphi, \quad (5.16)$$

$$BD \sin \beta = OF + DE \sin \varphi, \quad (5.17)$$

$$\rightarrow y \cos \varphi - AO \sin \varphi = \frac{y^2 + AO^2 + DE^2 - BD^2}{2DE}, \quad (5.18)$$

where  $y = x - BF$ . Similarly, (5.18) presents a function  $\beta = f(y)$ .

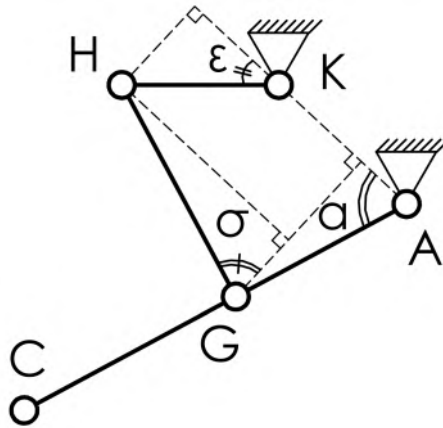


FIGURE 5.15: The kinematic of the four-bar mechanism (AGHK) with HK is the servo arm.

### 5.2.3.3 Servo Crank Analysis

From Figure. 5.15, we have:

$$GH \sin \sigma = AK - AG \cos \alpha + HK \cos \epsilon, \quad (5.19)$$

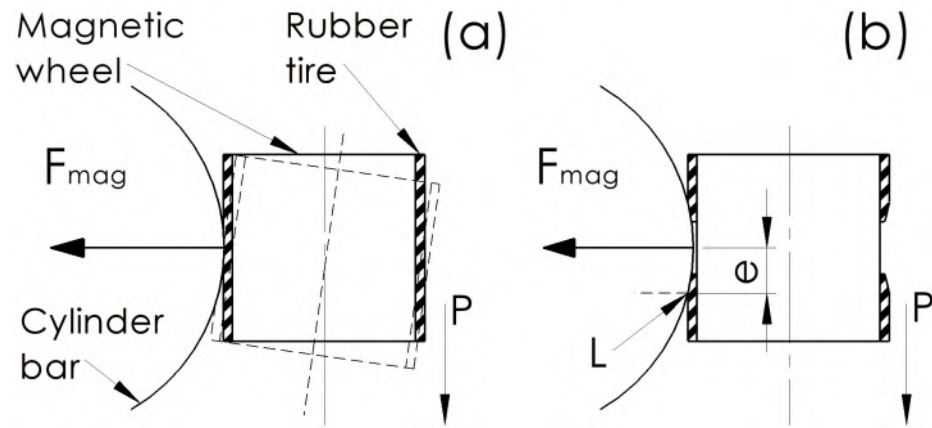


FIGURE 5.16: The design of rubber tires. a) One strip tire, b) Two separated strips tire.

$$GH \cos \sigma = AG \sin \alpha - HK \sin \epsilon. \quad (5.20)$$

Square and sum both sides of (5.19) and (5.20) then simplify, we have:

$$\begin{aligned} 2AGHK \cos(\alpha - \epsilon) + 2AK(AG \cos \alpha - HK \cos \epsilon) \\ = AK^2 + AG^2 + HK^2 - GH^2, \end{aligned} \quad (5.21)$$

presenting a function  $\epsilon = f(\alpha)$ .



## 5.2.4 Wheel Tire and Couplant Pumping

### 5.2.4.1 Wheel Tire Design

Wheel tires require a particular pattern to warranty the robot's stability in extreme situations; particularly, when the robot's body is horizontal as it travels along a cylinder bar. Figure. 5.16 depicts a cross-section in this situation. With one strip of tire for the entire wheel, the robot's body is inclined because of gravity (Figure. 5.16a), causing drifting when the robot turns. To fix the drifting issue, two separated rubber strips are applied to improve the approaching area between the tire and curved surfaces. As shown in Figure. 5.16b, using two strips, the turning point L is created, and the torque  $eF_{\text{mag}}$  is generated to stabilize the robot's body.

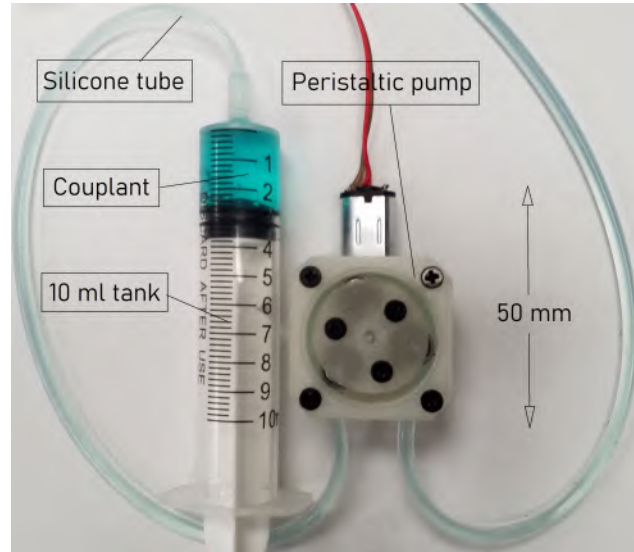


FIGURE 5.17: High viscosity couplant is stored in a syringe tank. A mini peristaltic pump with a silicone tube is utilized to release the couplant.

#### 5.2.4.2 Couplant Pumping

Since we use an ultrasonic sensor for thickness measurement, couplant is necessary to fill the air gap between the transducer and the test specimen [89]. The couplant with high viscosity is utilized to stick well on surfaces, even in upside-down or vertical positions. We selected the peristaltic pump type for high-viscosity gel. We also chose the syringe mechanism for gel storage because it can work on any robot pose. The pump is described in Figure. 5.17.

### 5.3 Magnetic Force Analysis

The previous analysis is only applied when the robot moves on flat steel surfaces. However, there are also structures, which have curved surfaces and extreme cases when magnetic force significantly increases or decreases. So, the following analysis will help determine the impact of the magnetic force created.

We conducted experiments with different steel shapes in real conditions to verify the performance of the magnetic wheel in both static and dynamic conditions.

The wheels tested is N52 neodymium magnet with a dimension of 2.5" od x 1/2" id x 1" thick. In static conditions, the minimum pull force is 205*N* at a 100*mm* diameter steel cylinder. At an edge, the force drops to 145*N*. In the 90-degree internal corner, the force hit 345*N*. In dynamic conditions, with the robot's velocity of 20cm/s, adhesive force falls to around 10 percent.

### 5.3.1 Static condition

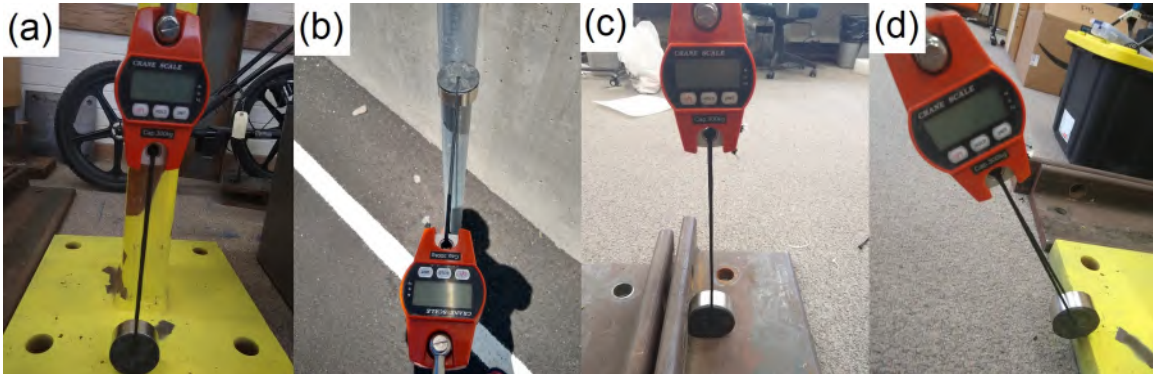


FIGURE 5.18: a) The test on a flat 4cm thick surface b) The test on a 10 cm diameter tube with 5mm thickness. Several tests on cylindrical structures were also conducted with diameters ranging from 20cm to 90 cm c) the test on a 90-degree internal corner, when the wheel bears additional force from a transiting surface d) The test on an edge of an external corner.

To measure the adhesive force created by permanent magnets, we set up different tests as shown in Figure 5.18. The wheel mass is  $m = 0.3kg$  - is placed on top of steel surfaces and corners while it is connected to a scale through an inelastic wire. We create a pull force onto the scale trying to lift the wheel off the surface. At the time the robot is about to be off the surface, the force applied to the scale is equal to the sum of the robot's weight and the magnetic pull force. Denote  $F_{pull}$  as the force we applied onto the scale,  $M$  is the value shown on the scale while  $P$  is the weight of the robot's body, and  $F_{mag}$  is the magnetic force. With  $g = 10m/s^2$ ,  $P = mg = 3N$  and  $F_{pull} = Mg = 10M$ , we can calculate magnetic adhesive force as follows:

$$F_{pull} = P + F_m \Rightarrow F_m = F_{pull} - P$$

$$\Rightarrow F_{mag} = 10M - 3(N). \quad (5.22)$$

Figure 6.11 shows the testing results of a non-coated magnetic wheel on flat and different curved surfaces. On a flat surface magnetic force get a maximum of nearly 300N. With 0.5mm rubber coated, the force decreases by around 9 percent. Figure

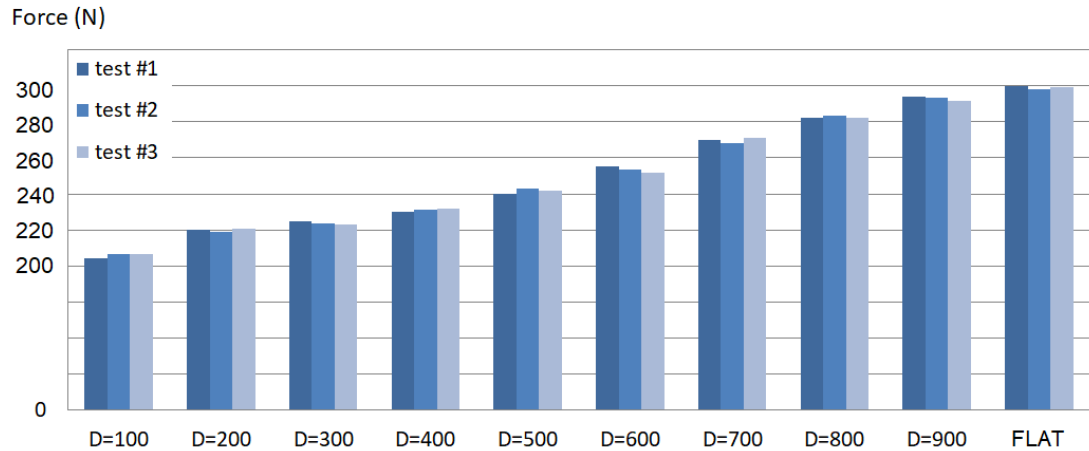


FIGURE 5.19: Adhesive forces measurements of a non-coated magnetic wheel on steel surfaces.

6.12 presents the testing results of a non-coated magnetic wheel on 90-degree internal ( $345N$ ) and external corners ( $145N$ ). These are two extreme cases robot deals with complex steel structures.

### 5.3.2 Dynamic condition

We also measure the adhesive force of the robot in a moving state as shown in Figure. 5.21. Each measurement is conducted three times. On average, the adhesive force in the dynamic condition is lower than approximately 10% compared to the static state.

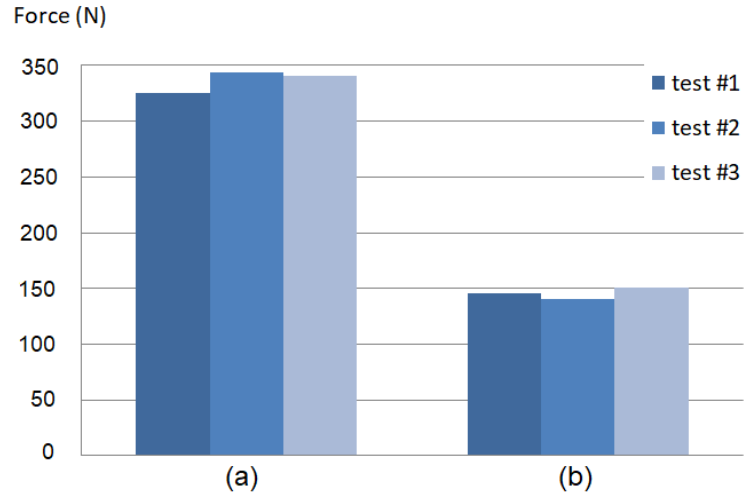


FIGURE 5.20: a) Magnetic force measurement in an internal corner b) Magnetic force measurement in an external corner

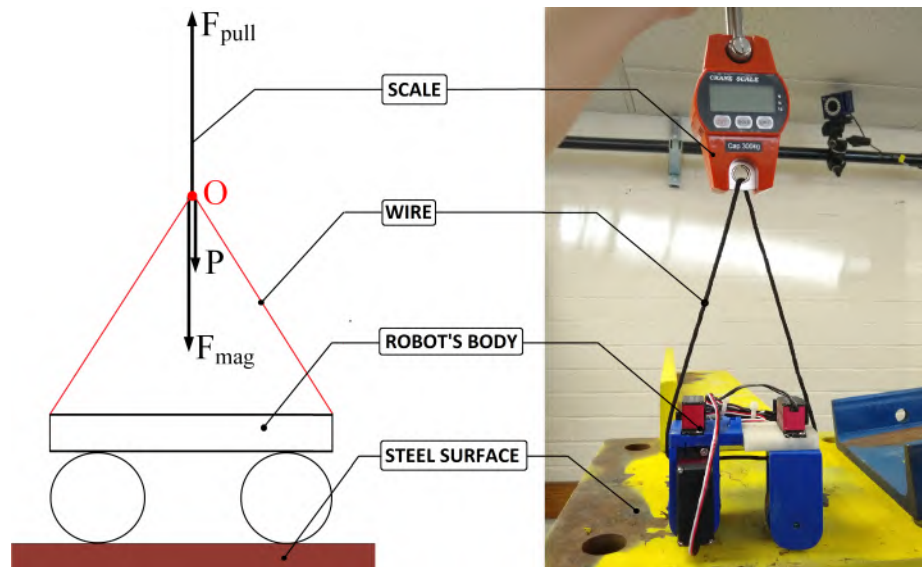


FIGURE 5.21: Experimental setup for magnetic force measurement when robot moving.

In this experiment, the full force of the robot's body is measured. The adhesive force is generated by two wheels and  $P$  in equation (5.22) is robot weight. All the tests are executed three times.

In the worst situation, when a robot passes a thorny edge, two coated wheels contact

least to the structure. The adhesive force of each wheel is lowest by  $145N$  - 9% of coated tire reduction - 10% of force losing in dynamic conditions =  $119N$ . Two wheels generate  $238N$ , robot's weight is  $2kg$ , which still satisfies equation (6.4). Therefore, the robot is safe in surveyed situations.

## 5.4 Robot Deployment

To evaluate the design and performance of the robot, experiments for evaluating the magnetic force created by magnetic wheels have been conducted. The ability of climbing and failure avoidance were tested. During the test, a Lipo battery (2 cells)  $7.4V$   $900$  milliampere-hour ( $mAh$ ) is used to power the robot for about 30 minutes of working. One laptop which can connect to a wireless LAN is used as a ground station. The robot's mass  $m = 2kg$ , and if we assume that the gravitational acceleration  $g = 10m/s^2$ , the total weight of the robot is approximately  $P = mg = 20N$ .

### 5.4.1 Laboratory Tests

We built an indoor structure comprising typical parts of general steel structures (cylinder, L-, I-, U-shaped beams) with structural transition joints to validate the robot's locomotion functionalities. Our robot can traverse smoothly to all locations in the testing structure. Figure. 5.22 shows the verification of robot design in extreme conditions. The robot crosses convex and concave surfaces. The robot makes a 90-degree

turn on internal and external corners. Figure. 5.23 illustrates the robot is working on

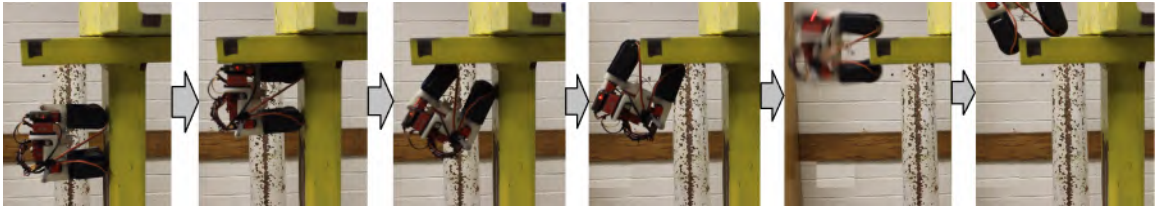


FIGURE 5.22: Robot passes 90 degrees internal and external corners.

a cylindrical shape. The robot in bicycle mode gets sliding when trying to transit between two surfaces. The robot can pass it smoothly in multi-directional mode Figure.

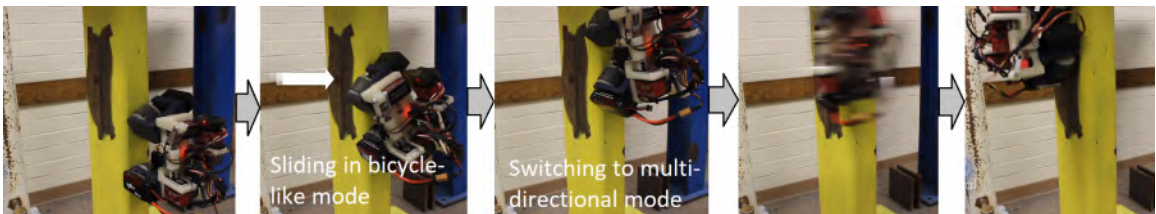


FIGURE 5.23: The robot travels along a rectangular structure. The robot gets sliding failure when transiting to another surface. By switching to multi-directional mode, the robot overcomes this situation easily.

5.24 shows a robot working on a cylindrical structure. Figure. 6.15 illustrates the



FIGURE 5.24: Thanks to free joint Figure. 5.3 makes the robot body flexible. Wheels fully adhere to any surface curvatures. Robot locomotion tests on a cylindrical structure.

process by that a robot passes a thorny edge. A transforming mechanism is utilized in this situation. Figure. 5.26 describe the process by that a robot transforms in



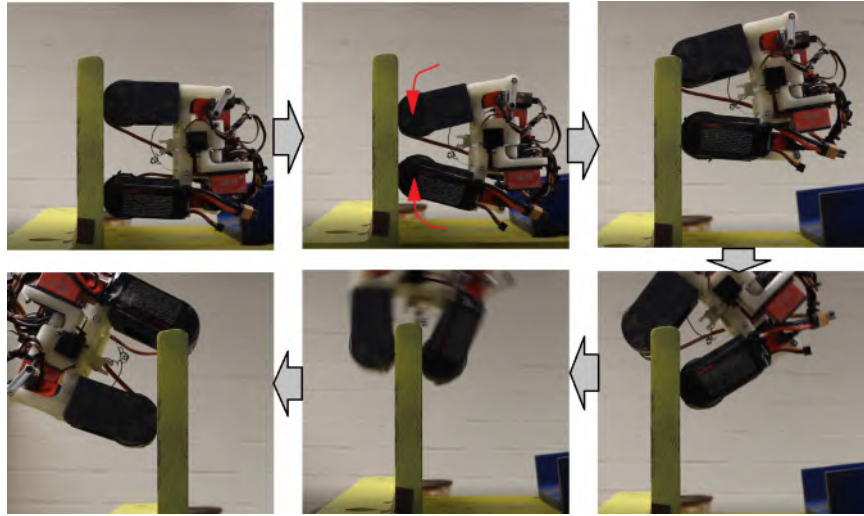


FIGURE 5.25: A 20mm-thick steel plate is used for the thin edge test. The robot's wheel distance (RWD) is 40mm in normal conditions. The transforming mechanism is activated to allow RWD as close as 15mm. So, the robot now can pass the edge.

shape to adapt to an acute corner. Once the front wheel can hit the second surface, the transition conducts easily. Figure. 5.27 is a complete test of robot locomotion

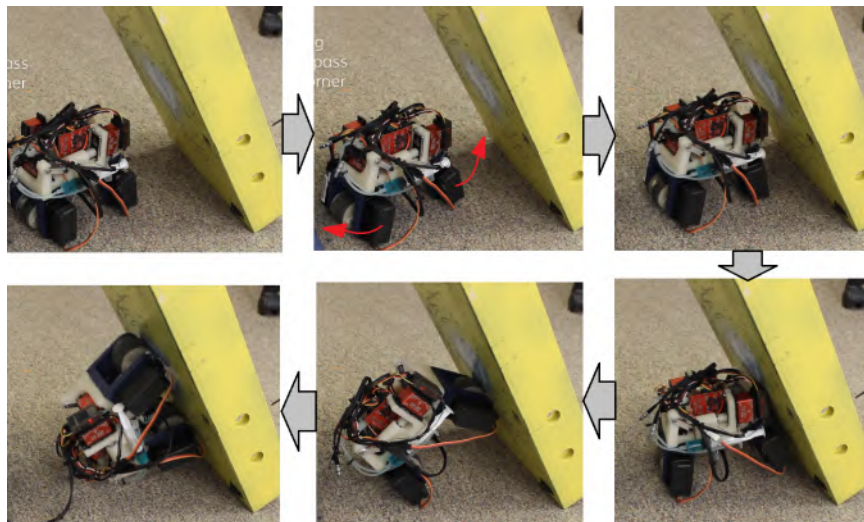


FIGURE 5.26: A 60-degree acute corner is shown in this test. Because of the robot's shape, the front wheel cannot hit the acute corner in normal conditions. The transforming mechanism controls RWD as big as 100mm which enables the front wheel can touch the second surface of the acute corner to smoothly overcome it.

on the entire indoor structure. Sensor deployment is presented in Figure. 5.28. We





FIGURE 5.27: A complex structure setup for indoor experiments. It includes cylindrical, I-shape, U-shape, and rectangular steel frames. The robot can travel to almost any location except for discontinuous transitions and narrow spaces for robot size.

demonstrate a test of thickness measurement in Figure. 5.29. The transducer with a nozzle on one end is controlled to make contact with the target surface. Then couplant is applied to the surface through the pump. Data collected locations and values

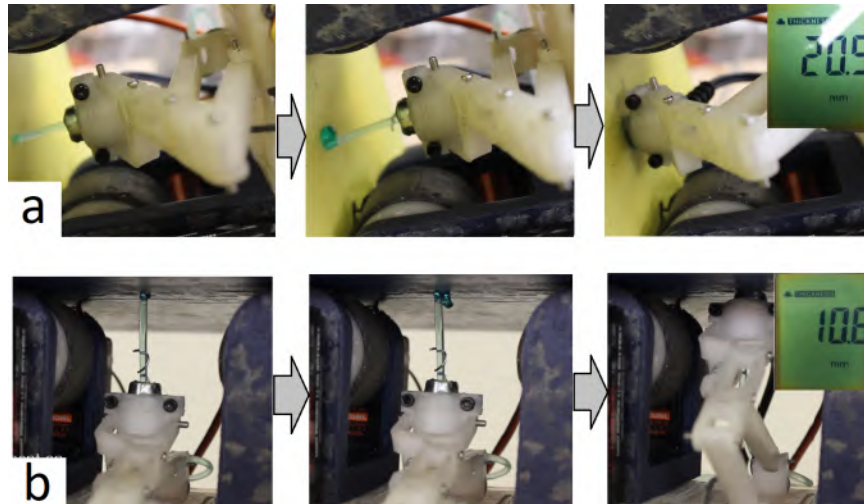


FIGURE 5.28: A demonstration of measuring the thickness of a steel surface. The couplant nozzle is controllable to move up and down. First, the nozzle is adjusted to fully touch the surface to make sure the gel/couplant will stick well without falling off in cases: a) the robot is vertical and b) upside down. Second, the gel is pumped 0.4 milliliters. Next, the nozzle moves up 0.5 cm to give space for the transducer. The transducer deploys 3 times to get an average value. If measurements are not good by giving N/A, the gel is added more to improve the contact with the surface.

synchronization in a 3D environment for live monitoring and saving. The experiment is shown in Figure. 5.29

## 5.4.2 Field Tests

Several implementations of field bridges have been conducted to verify robot performance in real working conditions. The robots deployed on three bridges with two main structures: cylindrical and I-shape beams. The first test is on a cylindrical type

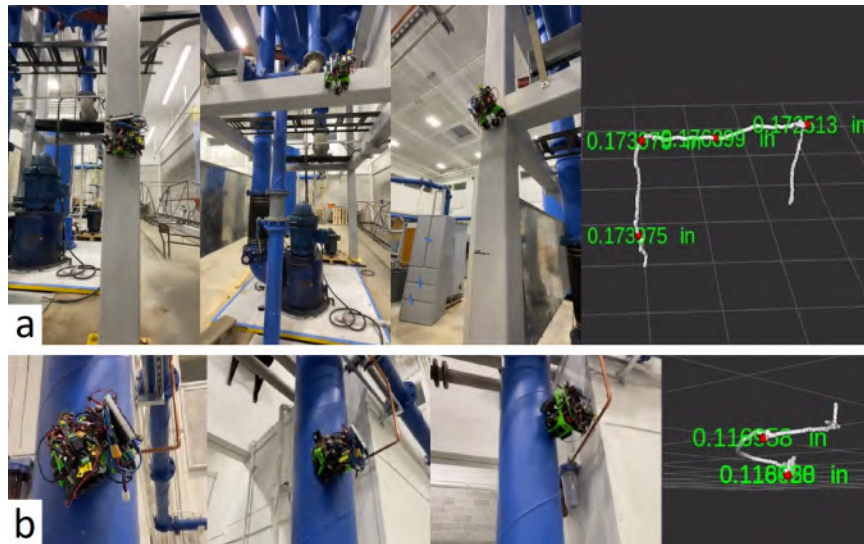


FIGURE 5.29: The tests are on (a) a square tube structure and (b) a cylindrical structure. The robot travels and stops to collect thickness data in interesting areas. Robot positions and data are matched and monitored in real time in a 3D environment. The robot path represents in white color. Steel thickness measuring positions are red dots. Thickness data (numbers in green color) is shown in inch units.

bridge as shown in Figure. 5.30. The bridge's structure includes cylindrical surfaces of 30cm and 22cm diameters. The robot performs thickness measurements in some areas that are rusty to check how severe the corrosion is. However, our sensor deployment mechanism cannot reach the internal angles of some rusted spots due to the vertical height limit of the four-bar mechanism.

We deployed the robot in a field test during an annual Highway inspection in Nevada, USA. The bridge is located on Highway-80 in Lovelock City. Figure. 5.31 shows robot performance in a real application, and the robot was able to traverse stably on the structure and collect data on this bridge. Robot reliably passes extreme cases of I-shape beam structure including internal and external corners. In real conditions, thick dust may reduce the pulling force and friction factor. However high safety factor





FIGURE 5.30: The robot operates on a cylindrical steel bridge on the campus of the University of Nevada, Reno.



FIGURE 5.31: Robot deployment on a bridge on Highway-80 located in Lovelock city, NV, USA. The robot traverses upside down on the main I-shape beam; the Robot passes an edge of the I-shape beam; the Robot moves upside down on a T-shape member, and the robot travels stably on a bridge water draining tube.

helps the robot getting no trouble, Figure 5.32. There is a data synchronization with the robot's pose presented when the robot deploy on a Highway bridge I-75 in Georgia, USA, Figure 5.33 The robot successfully passes all the tests both indoors and outdoors. In real working conditions, dust and rusty particles are further challenges that the robot must deal with. They reduce adhesive force and friction constant.

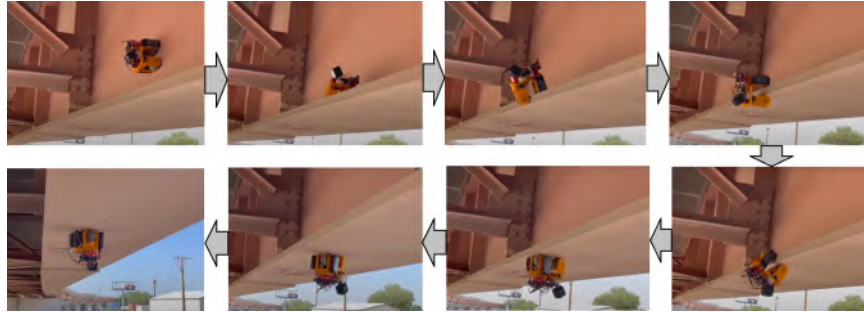


FIGURE 5.32: Robot smoothly traverses an edge of I-shape beam on the deployment on Highway-80



FIGURE 5.33: Robot deployment and data collection on a bridge on Highway I-75 in Georgia, USA. Robot positions and steel thickness data are synchronized in real-time. The robot path represents in white color. Steel thickness measuring positions are red dots. Thickness data (numbers in green color) is shown in inch units.

The robot tests and deployments are demonstrated in this video: [https://youtu.](https://youtu.be/Qdh1oz_oxiQ)

[be/Qdh1oz\\_oxiQ](https://youtu.be/Qdh1oz_oxiQ)

## 5.5 Conclusions

This chapter presents a bicycle-like robot designed for steel structure inspection. The robot carries an ultrasonic-based steel thickness measurement sensor and a camera and is capable of agilely climbing different steel structures. Validation tests were conducted on a laboratory structure, an outdoor bridge, and several highway bridges. The robot was able to adhere firmly to steel structures with various challenging levels. The kinematic and force of mechanisms were rigorously analyzed to confirm reliable performance in challenging real-world situations. The robot was demonstrated to perform thickness measurements on steel structures. In the future, addressing dust and rust issues and integrating additional non-destructive testing (NDT) sensing modules for more in-depth inspections will be a challenge.

## Chapter 6

# Onmi-directional Climbing Robot

This chapter proposes an advanced robotic system that employs a wheeled approach, coupled with a larger adhesion system on board. The unique ring magnet wheels used in this robot design make it capable of carrying large equipment loads and accommodating numerous additional sensing equipment and sensors.

Four independent wheel sub-assemblies are incorporated to provide excellent steering capabilities and maneuverability on steel surfaces. This system allows the robot to efficiently reach specific positions and orientations, maximizing its ability to utilize onboard equipment. Additionally, the proposed robot can travel on curved surfaces, including those with a diameter greater than 90cm, pass 90-degree internal and external corners, and edges with a thickness of 10mm.

The integration of the Ring system for multi-sensing deployment further enhances the robot's capabilities. The combination of these features into one compact robot creates a more capable machine than other recent works, suitable for a broader range of research settings. The robot's omnidirectional maneuverability makes it highly versatile and adaptable to diverse applications.

## 6.1 Overall System

The figures presented in Fig. 6.1 and Fig. 6.2 demonstrate a robot design featuring a dynamic body chassis and four modular wheel sub-assemblies that are independently steerable. The purpose of designing the robot with such features is to enable it to perform inspection tasks with high accuracy when traveling on steel surfaces. This feature is particularly useful when maneuvering in confined spaces or when localizing sensor deployment positions.

Each wheel sub-assembly consists of two steel rims on each side and a large ring magnet. The robot's design allows it to traverse long, continuous steel surfaces commonly found on steel bridges, and its ability to employ different steering configurations significantly enhances its ability to reach precise locations with specific orientations. This feature also enables the robot to make optimal use of its onboard inspection equipment, as it has a high capacity to modify its heading. Additionally, the different steering modes provide the robot's controller with intuitive methods to interact



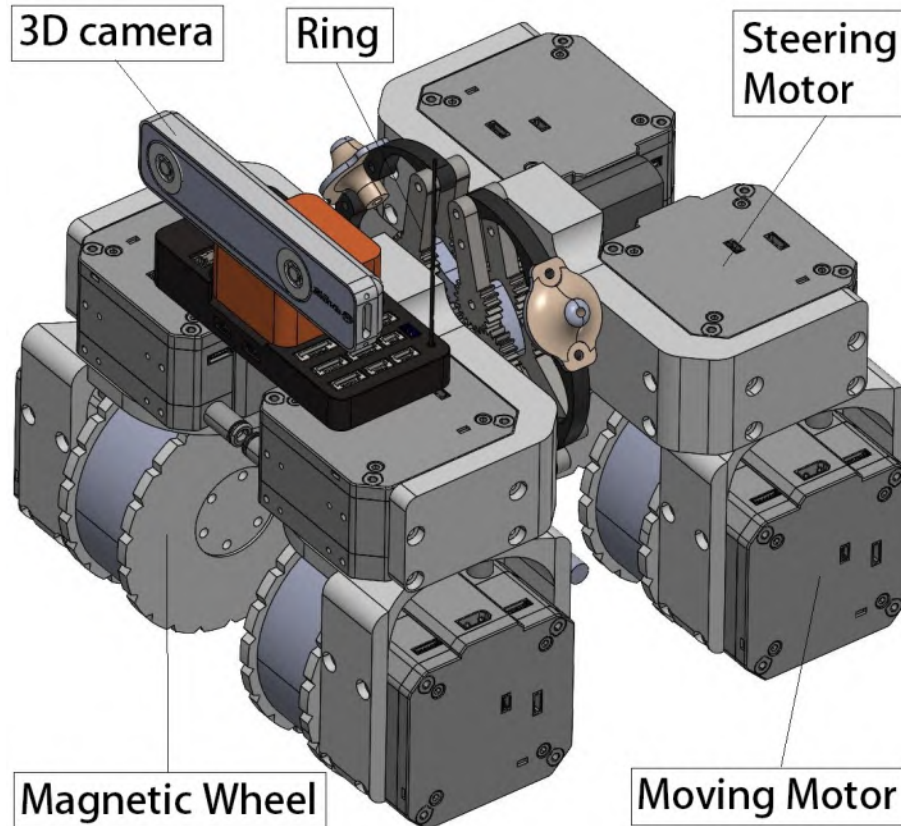


FIGURE 6.1: 3D model of the robot. There are four magnetic wheels driven by four moving motors. The flexibility of omnidirectional function is by four independent steering units. The robot body is flexible to fully adhere to any surface by an agile-free joint that links two half of the robot body. The ring system for sensor/-module deployment is placed in the middle of the robot body. This position is ideal for deployment on any surface even curved contours. This also protects sensors/-modules and is in conflict with locomotion functions. The robot is equipped with an onboard computer and a 3D camera for visual defect detection and mapping. The ultrasonic sensor is integrated for physical exams to measure material and coat thicknesses.

with and move the robot. The robot's locomotion is designed in three modes, as described in Fig. 6.3.

For visual inspection and localization, the robot incorporates a 3D camera (ZED), which provides the robot with poses and visual input for its rust detection module. The ring located in the center of the robot's body is a physical module designed

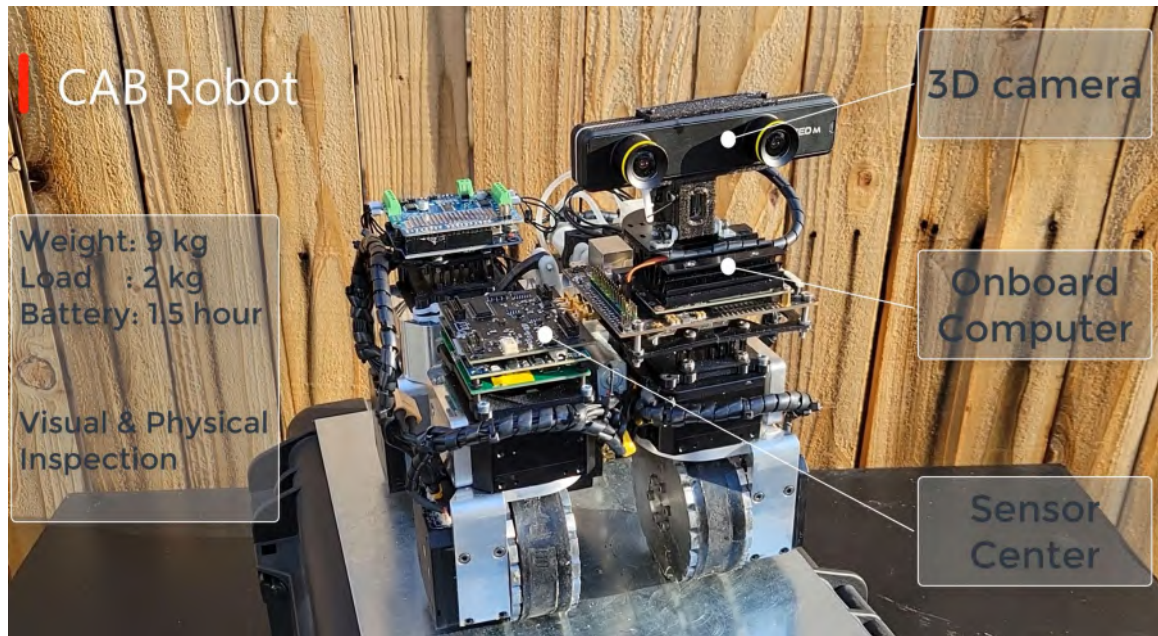


FIGURE 6.2: Robot is named Cab. It is 9 kg weight and an additional 2 kg load. Robots can provide both visual and physical inspections with available space sensors. In this design, the robot is integrated ultrasonic sensor module to measure the material thickness and gel pumping mechanism.

for contact-based examinations. Up to three sensors or modules can be attached to the ring, and in this particular application, a gel pumping module and an ultrasonic sensor for thickness measurement are attached.

## 6.2 Mechanical Design and Analysis

In general, the mechanical analysis for the Cab robot is similar to the multi-directional bicycle robot in the previous chapter in terms of locomotion including sliding analysis, turning over analysis, magnetic force analysis, and extreme locomotive situations.

In this design, due to the four-wheeled configuration, there are new maneuverability robots that can archive will be presented. Besides, the Ring mechanism for sensor

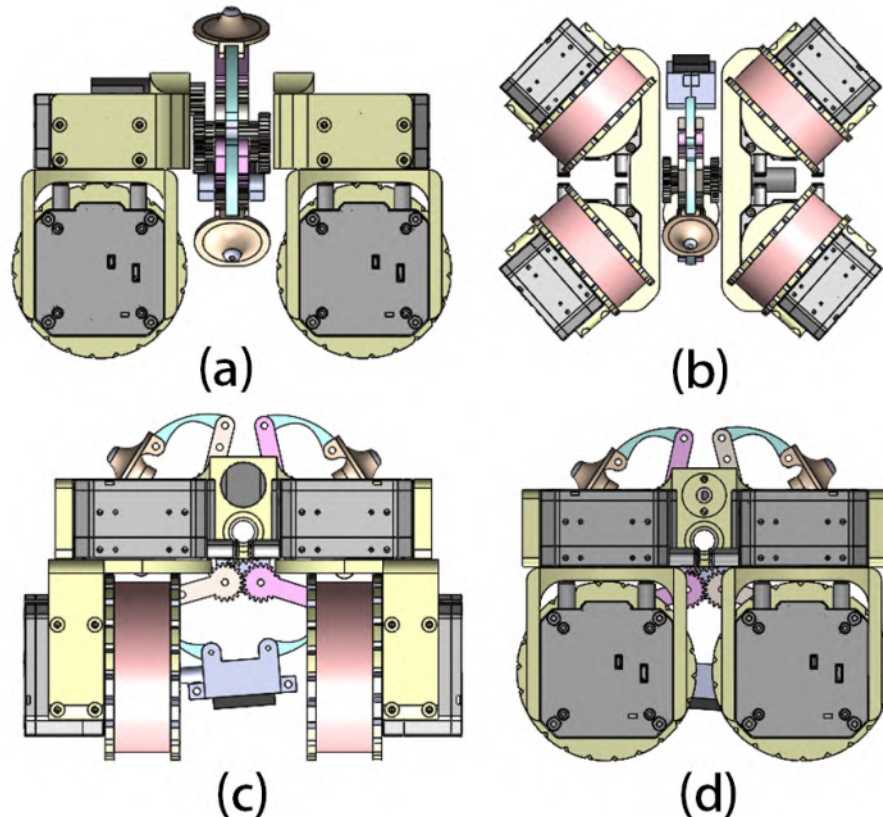


FIGURE 6.3: The advanced locomotion performance of the robot is illustrated. a) and c) the robot is in mode 1. It navigates in Ackerman configuration on simple contours or passing internal corners. b) Mode 2, when the robot needs to spin around, steering units change their shape to allow this motion, it is useful in limited space. d) In mode 3, when passing obstacles such as thin edges (reinforce bar of structures) robot heading transforms 90 degrees compared to mode 1. front and back wheels are close together with an 8mm distance.

deployment is analyzed.

### 6.2.1 Robot Maneuverability Analysis

In general, all maneuverability analysis for this robot is similar to the bicycle robot in the previous chapter. The only difference is the calculation applies to four wheels rather than two.

The proposed robot has been designed using a conventional approach to robotic kinematics, with four magnetic wheels that can be independently steered. This configuration of wheels enables the robot to utilize various advantageous steering configurations, including Ackerman, Synchronous, and Static-Point Steering.

These allow the proposed robot to be particularly adept at navigating awkward and uneven terrain found on steel structures through its ability to utilize each of the steering types shown in Fig. 6.3.

The proposed robot's degree of mobility ( $\delta_m$ ), steerability ( $\delta_s$ ) and maneuverability ( $\delta_M$ ) can be determined.

$$\delta_m = 3 - \text{rank}[C_1(\beta_s)]. \quad (6.1)$$

$$\delta_s = \text{rank}[C_{1s}(\beta_s)]. \quad (6.2)$$

$$\delta_M = \delta_m + \delta_s. \quad (6.3)$$

The robot's constraints are represented by the  $C$  matrix, and the vector  $\beta_s$  describes the steering angles of each of the robot's wheels. By implementing proper control mechanisms, the robot can be configured such that each of the wheel axes intersects at a single point, known as the instantaneous center of rotation (ICR). This point serves as the pivot point around which the robot moves.

When the robot satisfies this condition, it achieves a degree of mobility of one and a degree of steerability of two, resulting in an overall degree of maneuverability of

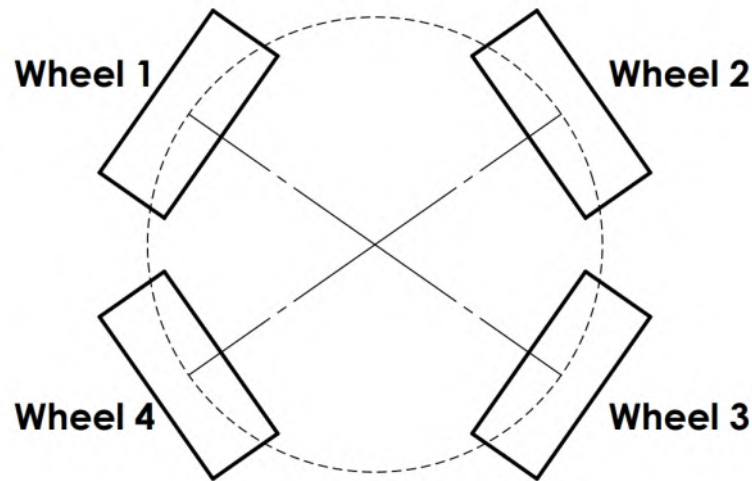


FIGURE 6.4: When the robot is spinning in place, the instantaneous center of rotation (ICR) is located at the center of the robot's body.

three. This means that the ICR of the robot is not constrained to any specific point on the surfaces it navigates.

In the mode 2, ICR is in the center of the robot body. So, the directions of wheels are on tangents of the spinning circle as shown in Fig. 6.4.

To ensure the safety of the robot, we need to analyze the adhesive force required for reliable climbing in all normal working conditions, even in the most extreme situation where the Cab design must pass a 10mm edge. In this scenario, the robot's minimum contact with the structure puts it at the highest risk of falling.

Figure 6.5 illustrates the extreme situation, where the adhesive force between the magnetic wheels and the contacting structures is minimal. Let us denote  $X_1$  and  $X_2$  as the two contacting points of the front and back wheels, respectively. Additionally,

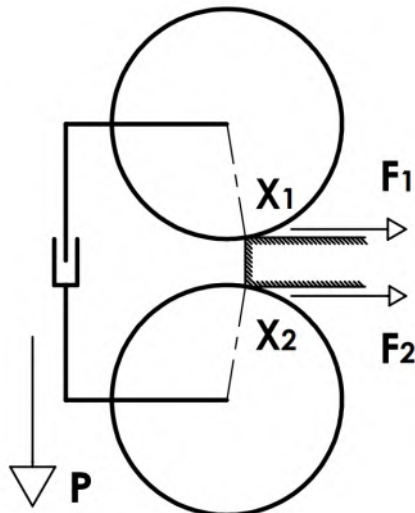


FIGURE 6.5: When the robot is in mode 3 and passes a 10mm edge, it experiences the minimum attractive force to the steel structure.

let  $P$  denote the weight of the robot, and  $h$  denote the distance from the center of mass of the robot to  $X_1$ .

To keep the robot safe, we must ensure that the adhesive force of the front wheel at  $X_1$  (denoted by  $F_1$ ) is at its minimum when the front wheel hits the corner. Therefore, the following condition must be satisfied:

$$F_1 \cdot X_1 X_2 > Ph \rightarrow F_1 > \frac{Ph}{X_1 X_2}. \quad (6.4)$$

### 6.2.2 Ring System Analysis

A twin reciprocating mechanism has been designed for generating vertical movements of the sensor/module, as depicted in Figure 6.6. The final links of the mechanism are



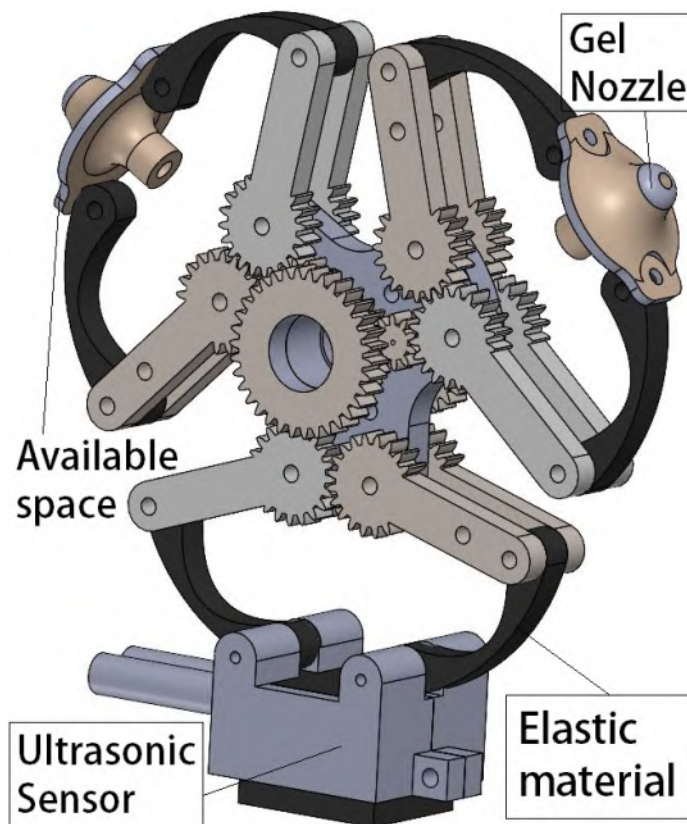


FIGURE 6.6: The Ring mechanism is a hybrid planetary gear system that is specifically designed for selecting sensors/modules and deploying them. made of elastic materials to prevent the overloading of the actuators and to enhance contact between the sensor/module and the working surfaces.

To analyze the mechanism, a simplified model is used, as shown in Figure 6.7. This figure illustrates that the deploying mechanism can be regarded as a special combination of ACE and BDF reciprocating mechanisms that work symmetrically. Specifically, we will analyze the ACE component of the mechanism.

From Figure. 6.7, we have:

$$CE \cos \varphi = x - AC \cos \alpha, \quad (6.5)$$

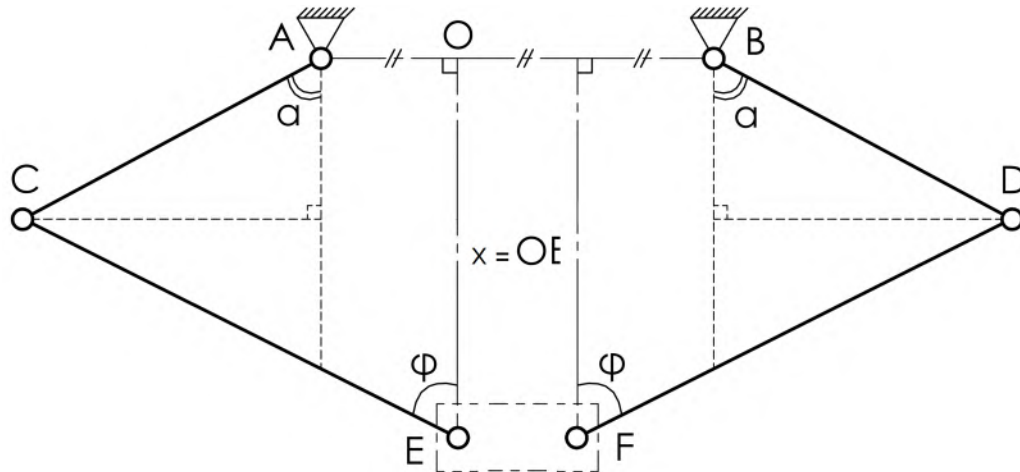


FIGURE 6.7: The symmetrically reciprocating mechanism kinematic.

$$CE \sin \varphi = AO + AC \sin \alpha. \quad (6.6)$$

Applying the similar approach as in (5.1) and (5.2) for (6.5) and (6.6), we have:

$$x \cos \alpha - AO \sin \alpha = \frac{x^2 + AO^2 + AC^2 - CE^2}{2AC}. \quad (6.7)$$

We observe that equation (6.7) represents a function  $\alpha = f(x)$ .

The working principle of the Ring mechanism is illustrated in Figures 6.8, 6.9, and 6.10. The gear arrangement is depicted in Figure 6.8, which shows the planetary gears starting from Gear 1 and 2 (Sun) to the Moon gears and finally to the Planet gears.

Figure 6.9 illustrates the Ring mechanism in selecting mode, in which the entire system rotates when Gear 1 and Gear 2 are rotating in the same direction.

Figure 6.10 illustrates how the deploying mode works when Gear 1 and Gear 2 are



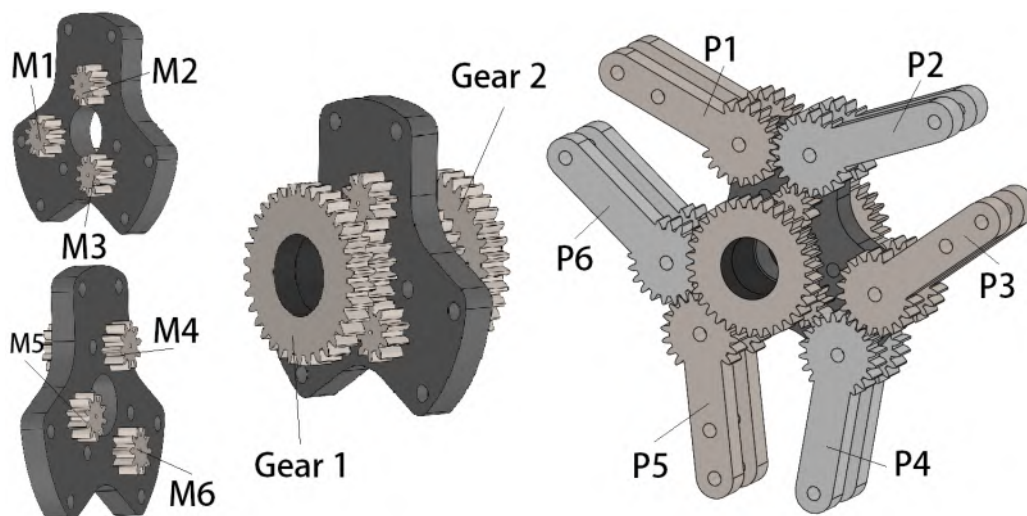


FIGURE 6.8: The center gears of the Ring mechanism, Gear 1 and 2, are placed on opposite sides and are driven by two actuators. The next round of gears consists of six Moon gears, named M1, M2, M3 on one side, and M4, M5, M6 on the other side. The Moon gears on each side rotate in the same direction. The Moon gears are connected to planetary gears or arms named P1 to P6. The P1-2, P3-4, and P5-6 gear pairs control the deployment of sensors or modules.

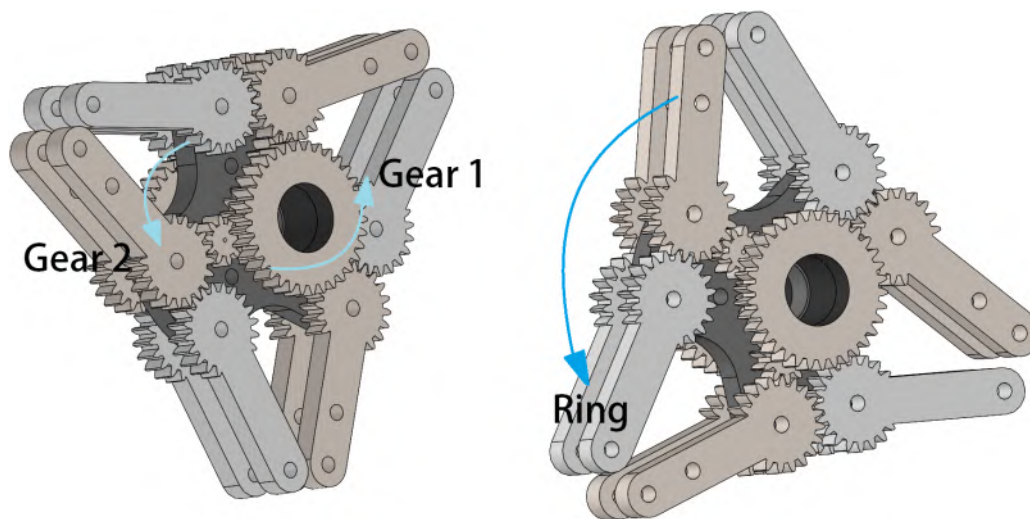


FIGURE 6.9: When Gear 1 and Gear 2 are rotating in the same direction, the whole Ring mechanism will rotate and allow for the selection of which module/sensor to deploy. In this design, three options are provided, as shown in Figure 6.9.

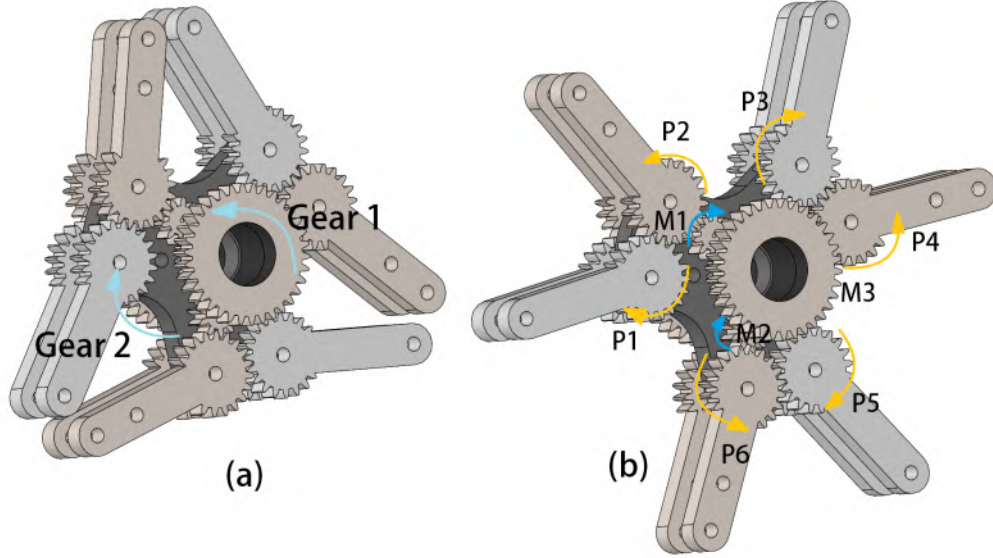


FIGURE 6.10: When gears 1 and 2 spin in opposite directions to each other, their moon gears M1, M2, and M3 rotate in one direction while M4, M5, and M6 rotate in the opposite direction. Planetary gear pairs P1-2, P3-4, and P5-6 act as reciprocating links to control the positions of the module/sensor for deployment or standby. To achieve soft contact with the surface, the sub-links are made with elastic materials, as shown in Figure 6.6.

rotating in different directions. In this mode, the Moon gears are forced to rotate in opposite directions, which causes the planetary gears to rotate around the stationary Sun gears. As a result, the arms attached to the planetary gears move in a reciprocating motion, which is used for deploying the selected module/sensor.

The ratio of the Ring system is the multiplication of the gear ratios from the actuators to the planetary arms. It can be calculated as follows:

$$T_{ring} = T\left(\frac{Motor}{Sun}\right) * T\left(\frac{Sun}{Moon}\right) * T\left(\frac{Moon}{Planet}\right) * T\left(\frac{Planet}{arm}\right) \quad (6.8)$$

where  $T_{motor}$  is the number of teeth on the gears of the actuators, and  $T_{Sun}$ ,  $T_{Moon}$  and  $T_{Planet}$  are the number of teeth on the gears of the planetary gears. The gear

ratio of each stage is the ratio of the number of teeth on the input gear to the number of teeth on the output gear while  $T(\frac{Planet}{arm})$  is the ratio of planetary gear radius divided to the arm length.

For the transducer to make good contact during deployment, it requires a minimum force of 20N. Each arm of the planet gear mechanism needs to provide a force of 10N. Let the length of each arm be denoted by  $l$  (m). Therefore, the torque (load) required is given by  $10l$  (Nm).

As a result, the actuator torque requirement is the load multiplied by the transmission ratio of the Ring mechanism, denoted by  $T_{ring}$  (Nm). Thus, the actuator torque requirement can be expressed as:

$$\text{Actuator torque requirement} = \text{Load} \times T_{ring} \text{ (Nm)} = 10l \cdot T_{ring} \text{ (Nm)}$$

### 6.3 Magnetic Force Analysis

Figure 6.12 presents the testing results of a non-coated magnetic wheel on 90-degree internal (345N) and external corners (145N). These are two extreme cases robot deals with complex steel structures.

Continuing from the previous chapter, this section aims to explore the magnetic force under different scenarios, including flat and curved surfaces as well as transitions. The analysis will provide insights into the impact of the magnetic force generated. To

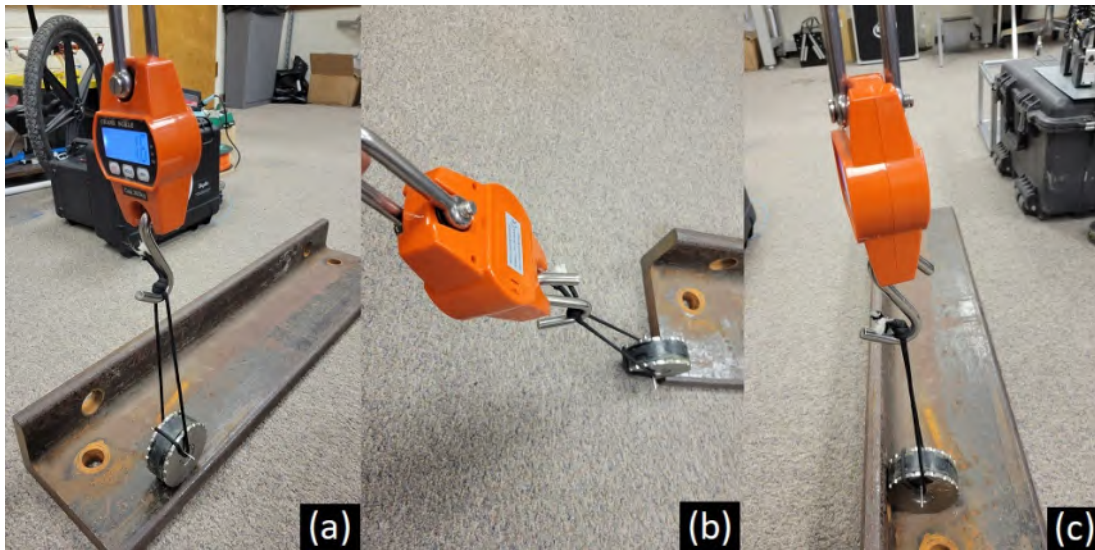


FIGURE 6.11: Magnetic force measurement in different working conditions. a) flat surface b) external corner c) internal corner

verify the effectiveness of the magnetic wheel in both static and dynamic conditions, we conducted experiments with various steel shapes in real-life situations. The wheels we tested were N52 neodymium magnets with dimensions of 3" od x 2" id x 1" thick and 2mm rubber tires. Our findings showed that in static conditions, the minimum pull force at the edge (90 degrees external corner) was  $110N$ , while in the 90-degree internal corner, the force reached  $305N$ . On a flat surface, the adhesive force was  $285N$ , but it dropped to  $265N$  when tested on a 90-degree curved surface. In dynamic conditions with a robot velocity of  $10\text{cm/s}$ , the adhesive force decreased to approximately 10 percent.

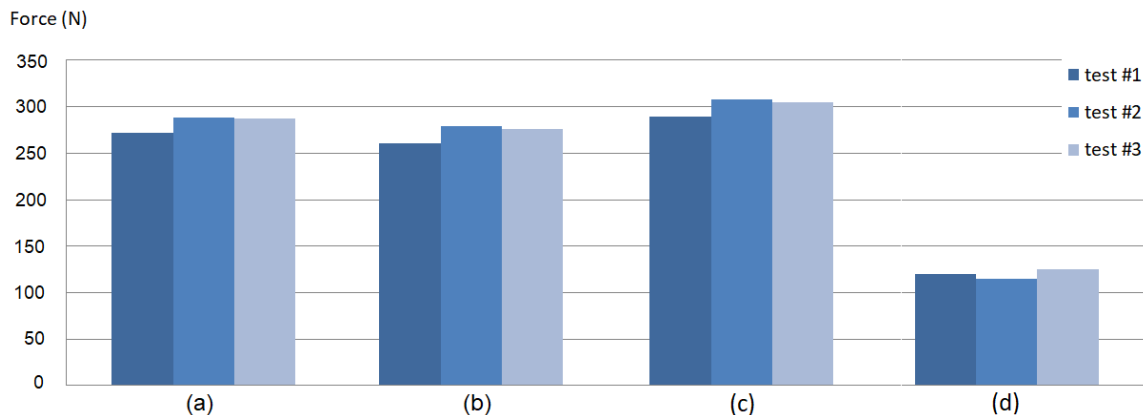


FIGURE 6.12: a) Magnetic force measurement in a flat surface b) Magnetic force measurement in a 90cm diameter curved surface c) Magnetic force measurement in an internal corner d) Magnetic force measurement in an external corner

## 6.4 Experimental Evaluation

To evaluate the design and performance of the robot, experiments for evaluating the magnetic force created by magnetic wheels have been conducted. The ability of climbing, maneuverability, and failure avoidance were tested as well as the Ring system for thickness measurement. The robot's mass  $m = 9kg$ , and if we assume that the gravitational acceleration  $g = 10m/s^2$ , the total weight of the robot is approximately  $P = mg = 90N$ .

Overall, the experiments showed that the robot is capable of achieving different modes of locomotion, allowing it to move effectively and efficiently in various environments. The Ackerman mechanism in Mode 1 provided the robot with a stable and precise method of movement, while Mode 2 allowed for quick and efficient changes in direction. Mode 3 provided the robot with the ability to traverse obstacles and thin edges with ease.



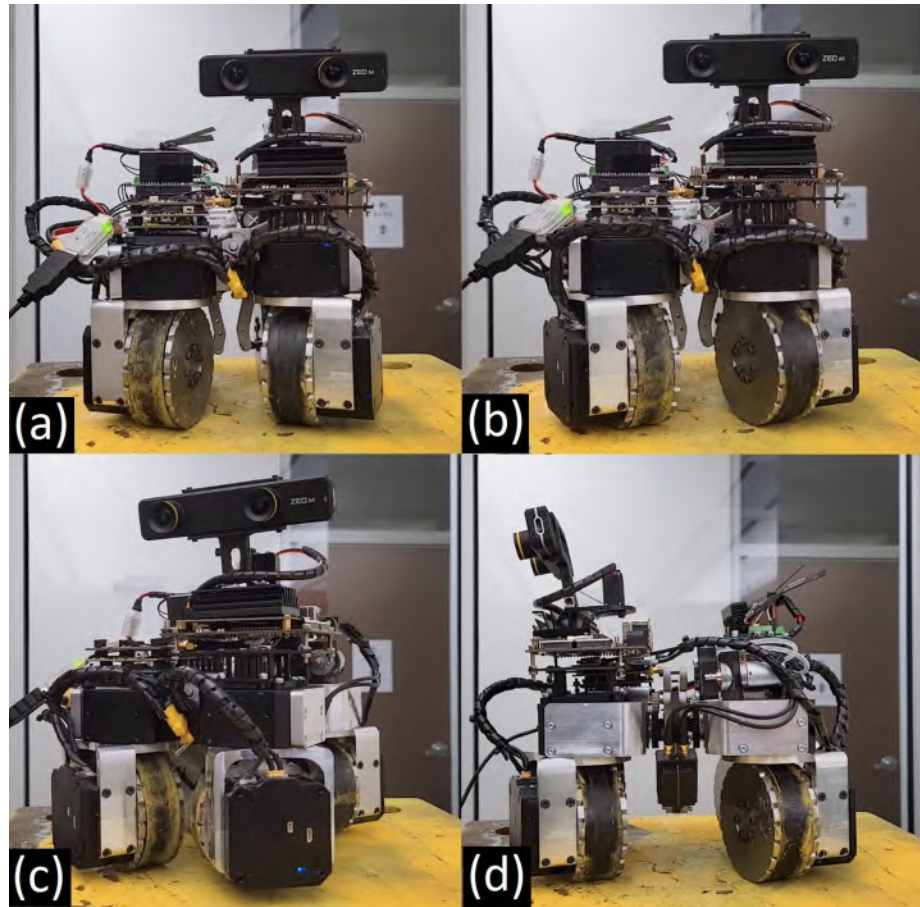


FIGURE 6.13: Robot locomotion, a) b) Mode 1: Robot mobility is Ackerman (car-like) mechanism. c) Mode 2: The robot turns around the spot. It is useful to change direction in a narrow space. d) Mode 3: The robot changes its head to move sideways. In this mode, the front and back wheels' distance is close to 8mm which function to pass obstacles and thin edges.

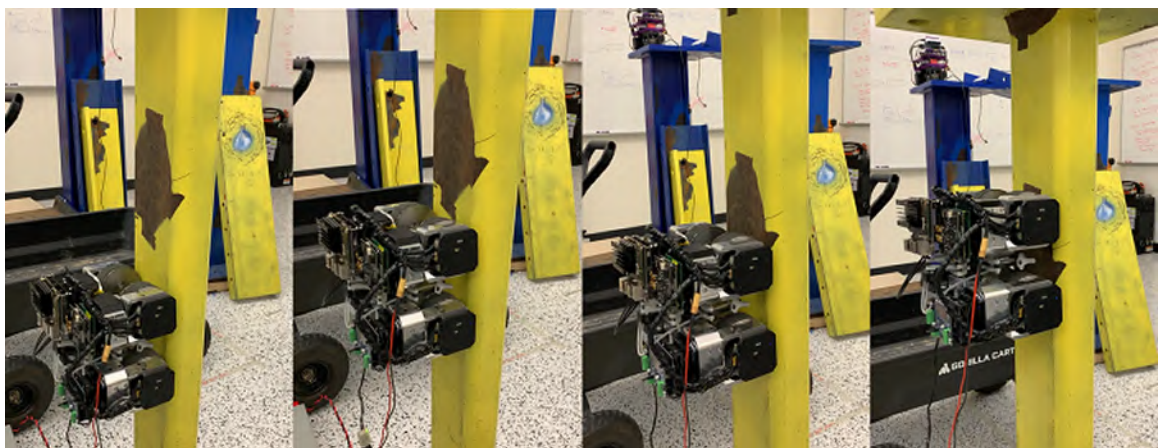


FIGURE 6.14: Robot traverses on mode 1.

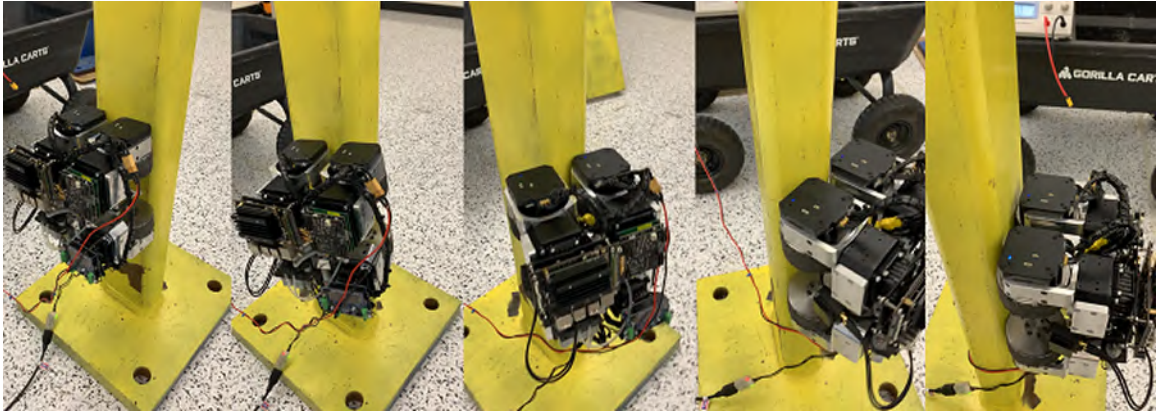


FIGURE 6.15: Robot does side-way movement in mode 3.

a) In Mode 1, Figure 6.14, robot mobility is achieved through the use of an Ackerman mechanism, which is similar to the movement of a car. This mode allows the robot to move in a forward direction while maintaining its stability and maneuverability. The experiment showed that the robot could move smoothly and accurately in different directions while maintaining its balance.

b) In Mode 2, the robot is capable of turning around a spot, which is particularly useful in changing direction in narrow spaces. This mode was found to be effective in allowing the robot to navigate tight corners and move in confined areas.

c) In Mode 3, Figure 6.15, the robot changes its head to move sideways. This mode was found to be particularly useful in allowing the robot to pass over obstacles and thin edges. The front and back wheels of the robot are placed closer together in this mode, with a distance of only 8mm, which allows the robot to maintain its stability while traversing uneven surfaces.

Experimental results show that the Ring system can smoothly change modules and deploy them with high precision. To measure material thickness, gel pumping is

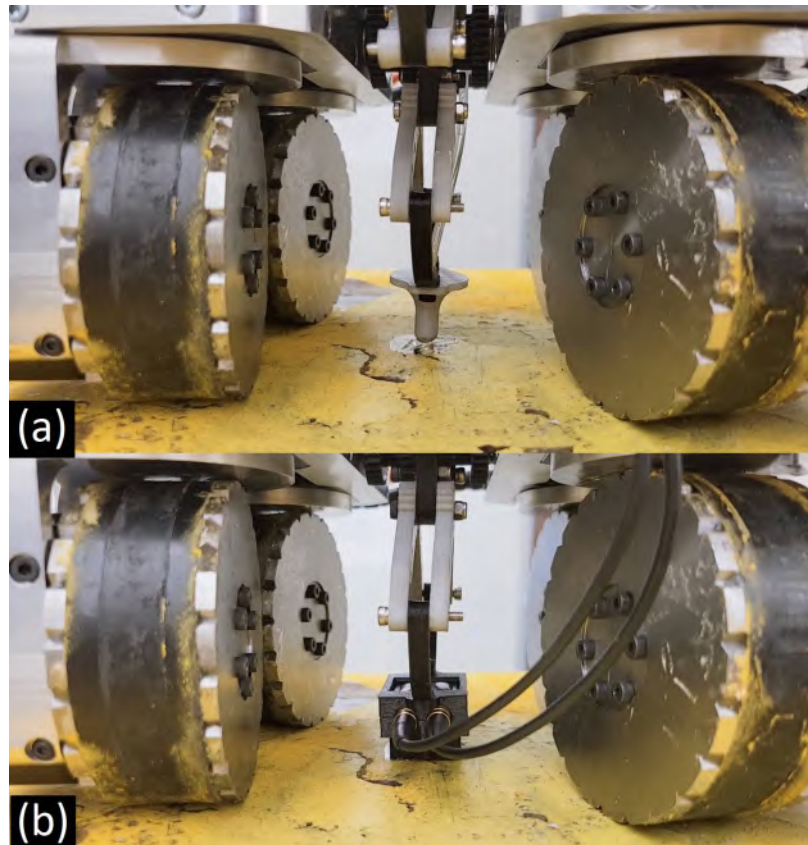


FIGURE 6.16: Ring system operation to measure material thickness. a) Gel pumping is deployed to enhance contact between the transducer and the surface. b) Ultrasonic transducer is deployed.

deployed to enhance the contact between the ultrasonic transducer and the surface being measured. The ultrasonic transducer successfully measures the thickness of the material with high accuracy.

The ultrasonic transducer was able to accurately measure the thickness of a variety of materials, including metals, plastics, and composites. The Ring system was able to select the appropriate transducer module and deploy it to the surface, ensuring that the measurements were taken at the correct location.



The gel pumping system helped to reduce the effects of surface roughness and unevenness, resulting in more accurate and consistent measurements. Additionally, the ability of the Ring system to deploy the transducer in a controlled and precise manner allowed for measurements to be taken in areas that would be difficult or impossible to access with traditional measurement tools.

Overall, the Ring system proved to be a reliable and effective tool for measuring material thickness, with the combination of the ultrasonic transducer and gel pumping providing accurate and consistent results.

## **6.5 Conclusions**

In conclusion, the proposed advanced robotic system named Cab incorporating the Ring system and wheeled approach provides a highly maneuverable and versatile platform for a wide range of research settings. The unique ring magnet wheels enable the robot to carry large equipment loads and accommodate additional sensing equipment and sensors. The four independent wheel sub-assemblies provide excellent steering capabilities. The robot can travel on curved surfaces, and pass corners and edges with a thickness of 10mm. The integration of the Ring system for multi-sensing deployment further enhances the robot's capabilities, allowing for smooth and precise deployment of multiple sensors. Overall, the proposed robot design offers a more capable machine than other recent works, with excellent potential for diverse applications.

# Chapter 7

## Conclusion & Future Work

### 7.1 Conclusion

This dissertation explores several innovative approaches to climbing robots for inspecting steel structures. The first design is a transformable tank-like robot that can navigate flat and curved surfaces, conduct crack detection via an Eddy current sensor and collect visual data remotely from a haptic device. The second design is a roller-chain-like robot with a unique shape and design that adapts well to various terrains and includes a detailed kinematic description and force analysis. The third design is a hybrid worming-mobile robot that combines the functions of a worm-moving type and a wheeled-mobile robot to handle complex structures, with a comprehensive physical analysis documented for reference and improvement. The fourth design is a multi-directional bicycle robot with high maneuverability and a simple mechanic and

control system, well suited for complicated steel structures such as bridges, and includes a sensor deployment mechanism that fits the robot's structure. All designs have been tested on laboratory structures and a cylindrical steel outdoor bridge, demonstrating firm adherence to steel structures of various challenging levels. A theoretical analysis of the kinematics and force of mechanisms confirms the robot's reliability in challenging real-world situations. Finally, the Cab robot is introduced as the most promising candidate for industrial applications, equipped with a large adhesion system and unique ring magnet wheels, and capable of carrying heavy loads and various sensing equipment. The integration of the Ring system enhances the robot's multi-sensing deployment capabilities, making it more versatile and adaptable to diverse applications than other recent works.

## 7.2 Future Work

In addition to the current innovations presented in this dissertation, there are several promising directions for future research in climbing robots for steel structure inspection. One important area is the development of autonomous navigation systems that can operate the robot without requiring human intervention. This could be achieved by integrating advanced sensor technologies, such as lidar and radar, which would allow the robot to accurately detect its surroundings and navigate through complex steel structures.

Another area of interest is using image processing techniques to enable the robot to perform automated inspection and mapping of steel structures. This would involve equipping the robot with high-resolution cameras and advanced software algorithms that can analyze the images and identify potential areas of concern. The information gathered could then be used to generate detailed reports and maps, which could be used to inform maintenance decisions and improve safety.

To enable autonomous navigation, accurate localization is a critical requirement. A combination of GPS and Visual Internal Odometry (VIO) can be used for this purpose in field applications. GPS provides the robot with a global position while VIO uses a camera or a set of cameras to track the robot's movements relative to its surroundings. This real-time pose information is useful for navigation on google earth-based maps and can be updated on this platform for easy management of collected data.

In conclusion, there are many exciting opportunities for further research in the area of climbing robots for steel structure inspection. By exploring these promising directions, researchers can continue to develop innovative solutions that improve the safety and efficiency of steel structure inspection, maintenance, and management.

# Publication

[1] S. T. Nguyen, and H. M. La. Development of a Steel Bridge Climbing Robot. In Proceedings of the 2019 IEEE/RSJ International Conference on Intelligent Robots and Systems (IROS), Macau, China, November 3 – 8, 2019 (Finalist of the ABB Best Student Paper Award, and the Best Paper Award on Safety, Security, and Rescue Robotics).

[2] S. T. Nguyen, and H. M. La. Roller Chain-Like Robot For Steel Bridge Inspection. In Proceedings of the 9th International Conference on Structural Health Monitoring of Intelligent Infrastructure (SHMII-9), August 4-7, St. Louis, Missouri, 2019.

[3] S. T. Nguyen, A. Q. Pham, C. Motley, and H. M. La. A Practical Climbing Robot for Steel Bridge Inspection. In Proceedings of the 2020 IEEE International Conference on Robotics and Automation (ICRA), May 31-June 4, 2020, Paris, France.

- [4] S. Nguyen, and H. M. La. A Climbing Robot for Steel Bridge Inspection. *Journal of Intelligent Robotic Systems*, Springer Publisher, 102, 75 (2021).  
<https://doi.org/10.1007/s10846-020-01266-1>
- [5] S. T. Nguyen, H. Nguyen, S. T. Bui, V. A. Ho, and H. M. La. An Agile Bicycle-like Robot for Complex Steel Structure Inspection, the 2022 IEEE International Conference on Robotics and Automation (ICRA), May 23-May 27, 2022, Philadelphia, USA.
- [6] S. T. Nguyen, and H. M. La. A Bicycle-like Robot for Automated Inspection of Complex Steel Structures. *Journal of Field Robotics*. (Under review).
- [7] H-D. Bui, S. T. Nguyen, U-H. Billah, C. Le, A. Tavakkoli, H. M. La. Control Framework for a Hybrid-steel Bridge Inspection Robot. In *Proceedings of the 2020 IEEE/RSJ International Conference on Intelligent Robots and Systems (IROS)*, Las Vegas, Nevada, USA, October 25 – 29, 2020.
- [8] Pham Anh, Cadence Motley, Son Nguyen, Hung La, A Robust and Reliable Climbing Robot for Steel Structure Inspection, Conference: 2022 IEEE/SICE International Symposium on System Integration (SII). Jan. 9-12, 2022. (Best paper finalist).
- [9] Cadence Motley, Son Nguyen, Hung La, Design of A High Strength Multi-Steering Climbing Robot for Steel Bridge Inspection, Conference: 2022 IEEE/SICE International Symposium on System Integration (SII). Jan. 9-12, 2022.
- [10] H. Ahmed, S. T. Nguyen, Duc La, Chuong P. Le and H. M. La. Multi-directional Bicycle Robot for Bridge Inspection with Steel Defect Detection System. 2022 IEEE/RSJ

International Conference on Intelligent Robots and Systems (IROS), October 23-27, 2022, Kyoto, Japan (Best paper finalist).

[11] Yu Otsuki, Son Thanh Nguyen, Hung Manh La, and Yang Wang. Autonomous Ultrasonic Thickness Measurement using a Steel Climbing Mobile Robot Integrated with Martlet Wireless Sensing. The 30th ASNT Research Symposium, June 20, 2022 – June 23, 2022, St. Louis, MO.

[12] Yu Otsuki, Son Thanh Nguyen, Hung Manh La, and Yang Wang. Autonomous Ultrasonic Thickness Measurement of Steel Bridge Members using a Climbing Bicycle Robot. *Journal of Engineering Mechanics*.



# Bibliography

- [1] FHWA. U.S Department of transportation highway administration, national bridge inventory data. <http://www.fhwa.dot.gov/bridge/nbi.cfm>, July 2019.
- [2] Washington bridge collapse, 2013. <https://www.cnn.com/2013/05/24/us/gallery/skagit-river-bridge/index.html>.
- [3] Golden-Gate-Bridge-Inspection. Crews inspect condition of golden gate bridge's towers, April 30, 2018. [https://www.nbcbayarea.com/on-air/as-seen-on/Crews-Inspect-Condition-of-Golden-Gate-Bridge\\_s-Towers\\_Bay-Area-481315951.html](https://www.nbcbayarea.com/on-air/as-seen-on/Crews-Inspect-Condition-of-Golden-Gate-Bridge_s-Towers_Bay-Area-481315951.html), 2018.
- [4] B. Purna Chandra Rao. *Non-destructive Testing and Damage Detection*, pages 209–228. Springer Singapore, Singapore, 2017. ISBN 978-981-10-2143-5. doi: 10.1007/978-981-10-2143-5\_11. URL [https://doi.org/10.1007/978-981-10-2143-5\\_11](https://doi.org/10.1007/978-981-10-2143-5_11).
- [5] A. McCrea, D. Chamberlain, and R. Navon. Automated inspection and restoration of steel bridges – a critical review of methods and enabling technologies.

- Automation in Construction*, 11(4):351 – 373, 2002. ISSN 0926-5805. doi: [https://doi.org/10.1016/S0926-5805\(01\)00079-6](https://doi.org/10.1016/S0926-5805(01)00079-6). URL <http://www.sciencedirect.com/science/article/pii/S0926580501000796>.
- [6] Anh Q. Pham, Anh T. La, Ethan Chang, and Hung M. La. Flying-climbing mobile robot for steel bridge inspection. In *2021 IEEE International Symposium on Safety, Security, and Rescue Robotics (SSRR)*, pages 230–235, 2021. doi: 10.1109/SSRR53300.2021.9597676.
- [7] Anh Q. Pham, Hung M. La, Kien T. La, and Minh T. Nguyen. A magnetic wheeled robot for steel bridge inspection. In *In: Sattler KU., Nguyen D., Vu N., Tien Long B., Puta H. (eds) Advances in Engineering Research and Application. ICERA 2019. Lecture Notes in Networks and Systems, Springer, Cham., volume 104, pages 11–17, 2020.* doi: DOI:10.1007/978-3-030-37497-6\_2.
- [8] Hung La. Steel climbing robot with magnetic wheels, March 26 2020. US Patent App. 16/464,874.
- [9] Hung Manh La, Tran Hiep Dinh, Nhan Huu Pham, Quang Phuc Ha, and Anh Quyen Pham. Automated robotic monitoring and inspection of steel structures and bridges. *Robotica*, 37(5):947–967, 2019. doi: 10.1017/S0263574717000601.
- [10] W. Fischer, F. Tâche, and R. Siegwart. *Magnetic Wall Climbing Robot for Thin Surfaces with Specific Obstacles*, pages 551–561. Springer Berlin Heidelberg, Berlin, Heidelberg, 2008. ISBN 978-3-540-75404-6. doi: 10.1007/

- 978-3-540-75404-6\_53. URL [https://doi.org/10.1007/978-3-540-75404-6\\_53](https://doi.org/10.1007/978-3-540-75404-6_53).
- [11] W. Fischer, G. Caprari, R. Siegwart, and R. Moser. Locomotion system for a mobile robot on magnetic wheels with both axial and circumferential mobility and with only an 8-mm height for generator inspection with the rotor still installed. *IEEE Transactions on Industrial Electronics*, 58(12):5296–5303, Dec 2011. ISSN 0278-0046. doi: 10.1109/TIE.2010.2051396.
- [12] P. Ratsamee, P. Kriengkamol, T. Arai, K. Kamiyama, Y. Mae, K. Kiyokawa, T. Mashita, Y. Uranishi, and H. Takemura. A hybrid flying and walking robot for steel bridge inspection. In *IEEE Inter. Symp. on Safety, Security, and Res. Robo.*, pages 62–67, Oct 2016. doi: 10.1109/SSRR.2016.7784278.
- [13] H. Wang and A. Yamamoto. Analyses and solutions for the buckling of thin and flexible electrostatic inchworm climbing robots. *IEEE Transactions on Robotics*, 33(4):889–900, Aug 2017. ISSN 1552-3098. doi: 10.1109/TRO.2017.2690302.
- [14] Bike, 2019. GE Inspection robot, December 01, 2019. Available at <https://inspection-robotics.com/bike>.
- [15] Weimin Shen, J Gu, and Yanjun Shen. Permanent magnetic system design for the wall-climbing robot. In *IEEE International Conference Mechatronics and Automation, 2005*, volume 4, pages 2078–2083 Vol. 4, July 2005. doi: 10.1109/ICMA.2005.1626883.

- [16] A. Mazumdar and H. H. Asada. Mag-foot: A steel bridge inspection robot. In *Intelligent Robots and Systems, 2009. IROS 2009. IEEE/RSJ International Conference on*, pages 1691–1696, Oct 2009.
- [17] R. Wang and Y. Kawamura. A magnetic climbing robot for steel bridge inspection. In *Intelligent Control and Automation (WCICA), 2014 11th World Congress on*, pages 3303–3308, June 2014.
- [18] F. Tâche, W. Fischer, G. Caprari, R. Siegwart, R. Moser, and F. Mondada. Magnebike: A magnetic wheeled robot with high mobility for inspecting complex-shaped structures. *Journal of Field Robotics*, 26(5):453–476, 2009. doi: 10.1002/rob.20296. URL <https://onlinelibrary.wiley.com/doi/abs/10.1002/rob.20296>.
- [19] R.T. Pack, Jr. Christopher, J.L., and K. Kawamura. A rubbertuator-based structure-climbing inspection robot. In *Robotics and Automation, 1997. Proceedings., 1997 IEEE International Conference on*, volume 3, pages 1869–1874 vol.3, Apr 1997.
- [20] M. Abderrahim, C. Balaguer, A. Gimenez, J. M. Pastor, and V. M. Padron. Roma: a climbing robot for inspection operations. In *Robotics and Automation, 1999. Proceedings. 1999 IEEE International Conference on*, volume 3, pages 2303–2308 vol.3, 1999.
- [21] A. Leibbrandt, G. Caprari, U. Angst, R. Y. Siegwart, R.J. Flatt, and B. Elsener. Climbing robot for corrosion monitoring of reinforced concrete structures. In

- Applied Robotics for the Power Industry (CARPI), the 2nd Intern. Conf. on*, pages 10–15, Sept 2012.
- [22] H. Leon-Rodriguez, S. Hussain, and T. Sattar. A compact wall-climbing and surface adaptation robot for non-destructive testing. In *Control, Automation and Systems (ICCAS), 2012 12th International Conference on*, pages 404–409, Oct 2012.
- [23] A. San-Millan. Design of a teleoperated wall climbing robot for oil tank inspection. In *Control and Automation (MED), 2015 23th Mediterranean Conference on*, pages 255–261, June 2015.
- [24] W. Shen, J. Gu, and Y. Shen. Proposed wall climbing robot with permanent magnetic tracks for inspecting oil tanks. In *IEEE International Conference Mechatronics and Automation, 2005*, volume 4, pages 2072–2077 Vol. 4, July 2005.
- [25] M. Tavakoli, C. Viegas, L. Marques, J. N. Pires, and A. T. de Almeida. Omniclimbers: Omni-directional magnetic wheeled climbing robots for inspection of ferromagnetic structures. *Robotics and Autonomous Systems*, 61(9): 997 – 1007, 2013. ISSN 0921-8890. doi: <https://doi.org/10.1016/j.robot.2013.05.005>. URL <http://www.sciencedirect.com/science/article/pii/S0921889013001024>.
- [26] M. Eich and T. Vögele. Design and control of a lightweight magnetic climbing robot for vessel inspection. In *the 19th Mediterranean Conf. on Control Automation*, pages 1200–1205, June 2011. doi: 10.1109/MED.2011.5983075.

- [27] G. Caprari, A. Breitenmoser, W. Fischer, C. Hurzeler, F. Tache, R. Siegwart, O. Nguyen, R. Moser, P. Schoeneich, and F. Mondada. Highly compact robots for inspection of power plants. *Journal of Field Robotics*, 29(1):47–68, 2012. doi: 10.1002/rob.21411. URL <https://onlinelibrary.wiley.com/doi/abs/10.1002/rob.21411>.
- [28] K. H. Cho, H. M. Kim, Y. H. Jin, F. Liu, H. Moon, J. C. Koo, and H. R. Choi. Inspection robot for hanger cable of suspension bridge: Mechanism design and analysis. *IEEE/ASME Transactions on Mechatronics*, 18(6):1665–1674, Dec 2013. ISSN 1083-4435. doi: 10.1109/TMECH.2013.2280653.
- [29] D. Zhu, J. Guo, C. Cho, Y. Wang, and K. Lee. Wireless mobile sensor network for the system identification of a space frame bridge. *IEEE/ASME Trans. on Mechatronics*, 17(3):499–507, June 2012. ISSN 1083-4435. doi: 10.1109/TMECH.2012.2187915.
- [30] G. Lee, G. Wu, J. Kim, and T. Seo. High-payload climbing and transitioning by compliant locomotion with magnetic adhesion. *Robotics and Autonomous Systems*, 60(10):1308 – 1316, 2012. ISSN 0921-8890. doi: <https://doi.org/10.1016/j.robot.2012.06.003>. URL <http://www.sciencedirect.com/science/article/pii/S0921889012000930>.
- [31] T. Seo and M. Sitti. Tank-like module-based climbing robot using passive compliant joints. *IEEE/ASME Transactions on Mechatronics*, 18(1):397–408, Feb 2013. ISSN 1083-4435. doi: 10.1109/TMECH.2011.2182617.

- [32] R. Wang and Y. Kawamura. A magnetic climbing robot for steel bridge inspection. In *Proceeding of the 11th World Congress on Intelligent Control and Automation*, pages 3303–3308, June 2014. doi: 10.1109/WCICA.2014.7053262.
- [33] J. Guo, W. Liu, and K. M. Lee. Design of flexonic mobile node using 3d compliant beam for smooth manipulation and structural obstacle avoidance. In *2014 IEEE International Conference on Robotics and Automation (ICRA)*, pages 5127–5132, May 2014. doi: 10.1109/ICRA.2014.6907611.
- [34] S. Kamdar. Design and manufacturing of a mecanum sheel for the magnetic climbing robot. *Master Thesis, Embry-Riddle Aeronautical University*, May 2015.
- [35] P. Ward, P. Manamperi, P. R. Brooks, P. Mann, W. Kaluarachchi, L. Matkovic, G. Paul, C. H. Yang, P. Quin, D. Pagano, D. Liu, K. Waldron, and G. Disanayake. Climbing robot for steel bridge inspection: Design challenges. In *Austroads Publications Online, ARRB Group*, 2015.
- [36] N. H. Pham and H. M. La. Design and implementation of an autonomous robot for steel bridge inspection. In *54th Allerton Conf. on Comm., Con., and Comp.*, pages 556–562, Sept 2016. doi: 10.1109/ALLERTON.2016.7852280.
- [37] R. Wang and Y. Kawamura. Development of climbing robot for steel bridge inspection. *Industrial Robot: An International Journal*, 43(4):429–447, 2016. doi: 10.1108/IR-09-2015-0186. URL <https://doi.org/10.1108/IR-09-2015-0186>.

- [38] N. H. Pham, H. M. La, Q. P. Ha, S. N. Dang, A. H. Vo, and Q. H. Dinh.
- [39] Y. Takada, S. Ito, and N. Imajo. Development of a bridge inspection robot capable of traveling on splicing parts. *Inventions*, 2, 2017. ISSN 2411-5134. doi: 10.3390/inventions2030022. URL <http://www.mdpi.com/2411-5134/2/3/22>.
- [40] Habib Ahmed and Hung Manh La. Steel defect detection in bridges using deep encoder-decoder networks. *Structural Health Monitoring 2021*, 2021.
- [41] Prateek Prasanna, Kristin J Dana, Nenad Gucunski, Basily B Basily, Hung M La, Ronny Salim Lim, and Hooman Parvardeh. Automated crack detection on concrete bridges. *IEEE Transactions on automation science and engineering*, 13(2):591–599, 2014.
- [42] Versatrax. Versatrax 150<sup>TM</sup>. <http://inuktun.com/en/products/>, 2019.
- [43] Genki Sato, Yasushi Mae, Masaru Kojima, and Tatsuo Arai. Transfer motion on planar structure of limb-mechanism robot in anti-gravity environment. In *Proceedings of 2018 ISFA International Symposium on Flexible Automation*, pages 467–472, 2018.
- [44] L. Van Nguyen, S. Gibb, H. X. Pham, and H. M. La. A mobile robot for automated civil infrastructure inspection and evaluation. In *2018 IEEE International Symposium on Safety, Security, and Rescue Robotics (SSRR)*, pages 1–6, Aug 2018. doi: 10.1109/SSRR.2018.8468642.



- [45] H. M. La, N. Gucunski, K. Dana, and S.-H. Kee. Development of an autonomous bridge deck inspection robotic system. *Journal of Field Robotics*, 34(8):1489–1504, 2017. doi: 10.1002/rob.21725. URL <https://onlinelibrary.wiley.com/doi/abs/10.1002/rob.21725>.
- [46] S. Gibb, T. Le, H. M. La, R. Schmid, and T. Berendsen. A multi-functional inspection robot for civil infrastructure evaluation and maintenance. In *2017 IEEE/RSJ International Conference on Intelligent Robots and Systems (IROS)*, pages 2672–2677, Sep. 2017. doi: 10.1109/IROS.2017.8206091.
- [47] T. Le, S. Gibb, N. Pham, H. M. La, L. Falk, and T. Berendsen. Autonomous robotic system using non-destructive evaluation methods for bridge deck inspection. In *2017 IEEE International Conference on Robotics and Automation (ICRA)*, pages 3672–3677, May 2017. doi: 10.1109/ICRA.2017.7989421.
- [48] H. M. La, R. S. Lim, B. B. Basily, N. Gucunski, J. Yi, A. Maher, F. A. Romero, and H. Parvardeh. Mechatronic systems design for an autonomous robotic system for high-efficiency bridge deck inspection and evaluation. *Mechatronics, IEEE/ASME Transactions on*, 18(6):1655–1664, Dec 2013.
- [49] H. M. La, N. Gucunski, S.-H. Kee, and L.V. Nguyen. Data analysis and visualization for the bridge deck inspection and evaluation robotic system. *Visualization in Engineering*, 3(1):1–16, 2015.
- [50] H. M. La, N. Gucunski, S.H. Kee, and L.V. Nguyen. Visual and acoustic data analysis for the bridge deck inspection robotic system. In *The 31st International*

*Symposium on Automation and Robotics in Construction and Mining (ISARC)*, pages 50–57, July 2014.

- [51] R. S Lim, H. M. La, Z. Shan, and W. Sheng. Developing a crack inspection robot for bridge maintenance. In *Robotics and Automation (ICRA), 2011 IEEE Intern. Conf. on*, pages 6288–6293, May 2011.
- [52] R. S. Lim, H. M. La, and W. Sheng. A robotic crack inspection and mapping system for bridge deck maintenance. *IEEE Transactions on Automation Science and Engineering*, 11(2):367–378, 2014.
- [53] S. Gibb, H. M. La, T. Le, L. Nguyen, R. Schmid, and H. Pham. Nondestructive evaluation sensor fusion with autonomous robotic system for civil infrastructure inspection. *Journal of Field Robotics*, 0(0), 2018. doi: 10.1002/rob.21791. URL <https://onlinelibrary.wiley.com/doi/abs/10.1002/rob.21791>.
- [54] B. Sutter, A. Lelevé, M. T. Pham, O. Gouin, N. Jupille, M. Kuhn, P. Lulé, P. Michaud, and P. Rémy. A semi-autonomous mobile robot for bridge inspection. *Automation in Construction*, 91:111 – 119, 2018. ISSN 0926-5805. doi: <https://doi.org/10.1016/j.autcon.2018.02.013>. URL <http://www.sciencedirect.com/science/article/pii/S0926580517304739>.
- [55] Habib Ahmed, Hung Manh La, and Nenad Gucunski. Review of non-destructive civil infrastructure evaluation for bridges: State-of-the-art robotic platforms, sensors and algorithms. *Sensors*, 20(14), 2020. ISSN 1424-8220. doi: 10.3390/s20143954. URL <https://www.mdpi.com/1424-8220/20/14/3954>.

- [56] Habib Ahmed, Hung Manh La, and Khiem Tran. Rebar detection and localization for bridge deck inspection and evaluation using deep residual networks. *Automation in Construction*, 120:103393, 2020. ISSN 0926-5805. doi: <https://doi.org/10.1016/j.autcon.2020.103393>. URL <https://www.sciencedirect.com/science/article/pii/S0926580520309730>.
- [57] Umme Hafsa Billah, Hung Manh La, and Alireza Tavakkoli. Deep learning-based feature silencing for accurate concrete crack detection. *Sensors*, 20(16), 2020. ISSN 1424-8220. doi: 10.3390/s20164403. URL <https://www.mdpi.com/1424-8220/20/16/4403>.
- [58] Habib Ahmed, Hung Manh La, and Alireza Tavakkoli. Use of deep encoder-decoder network for sub-surface inspection and evaluation of bridge decks. *Structural Health Monitoring 2021*, 2021.
- [59] Habib Ahmed, Hung Manh La, and Nenad Gucunski. Rebar detection using ground penetrating radar with state-of-the-art convolutional neural networks. In *Proceedings of the 9th International Conference on Structural Health Monitoring of Intelligent Infrastructure, St. Louis, MI, USA*, pages 4–7, 2019.
- [60] Habib Ahmed, Hung Manh La, and Gokhan Pekcan. Rebar detection and localization for non-destructive infrastructure evaluation of bridges using deep residual networks. In *Advances in Visual Computing: 14th International Symposium on Visual Computing, ISVC 2019, Lake Tahoe, NV, USA, October 7–9, 2019, Proceedings, Part I 14*, pages 631–643. Springer, 2019.

- [61] Umme Hafsa Billah, Alireza Tavakkoli, and Hung Manh La. Concrete crack pixel classification using an encoder decoder based deep learning architecture. In *Advances in Visual Computing: 14th International Symposium on Visual Computing, ISVC 2019, Lake Tahoe, NV, USA, October 7–9, 2019, Proceedings, Part I 14*, pages 593–604. Springer, 2019.
- [62] Spencer Gibb, Hung Manh La, and Sushil Louis. A genetic algorithm for convolutional network structure optimization for concrete crack detection. In *2018 IEEE congress on evolutionary computation (CEC)*, pages 1–8. IEEE, 2018.
- [63] Tran Hiep Dinh, Quang Phuc Ha, and Hung M La. Computer vision-based method for concrete crack detection. In *2016 14th international conference on control, automation, robotics and vision (ICARCV)*, pages 1–6. IEEE, 2016.
- [64] Spencer Gibb and Hung Manh La. Automated rebar detection for ground-penetrating radar. In *Advances in Visual Computing: 12th International Symposium, ISVC 2016, Las Vegas, NV, USA, December 12-14, 2016, Proceedings, Part I 12*, pages 815–824. Springer, 2016.
- [65] Kien Dinh, Nenad Gucunski, Jinyoung Kim, Trung H Duong, and Hung M La. Attenuation-based methodology for condition assessment of concrete bridge decks using gpr. In *ISARC. Proceedings of the International Symposium on Automation and Robotics in Construction*, volume 32, page 1. IAARC Publications, 2015.

- [66] Nenad Gucunski, S-H Kee, H La, B Basily, A Maher, and H Ghasemi. Implementation of a fully autonomous platform for assessment of concrete bridge decks rabbit. In *Structures Congress 2015*, pages 367–378, 2015.
- [67] Nenad Gucunski, S Kee, Hung La, Basily Basily, and Ali Maher. Delamination and concrete quality assessment of concrete bridge decks using a fully autonomous rabbit platform. *Structural Monitoring and Maintenance*, 2(1):19–34, 2015.
- [68] N Gucunski, B Basily, S-H Kee, H La, H Parvardeh, A Maher, and H Ghasemi. Multi nde technology condition assessment of concrete bridge decks by rabbitm platform. In *NDE/NDT for Structural Materials Technology for Highway & Bridges*, pages 161–168, 2014.
- [69] Hung Manh La, Nenad Gucunski, Seong-Hoon Kee, and Luan Nguyen. Visual and acoustic data analysis for the bridge deck inspection robotic system. In *ISARC. Proceedings of the International Symposium on Automation and Robotics in Construction*, volume 31, page 1. IAARC Publications, 2014.
- [70] Nenad Gucunski, A Maher, B Basily, H La, R Lim, H Parvardeh, and SH Kee. Robotic platform rabbit for condition assessment of concrete bridge decks using multiple nde technologies. *HDKBR INFO Magazin*, 3(4):5–12, 2013.
- [71] H. M. La, N. Gucunski, Seong-Hoon Kee, J. Yi, T. Senlet, and Luan Nguyen. Autonomous robotic system for bridge deck data collection and analysis. In

- 2014 IEEE/RSJ International Conference on Intelligent Robots and Systems*, pages 1950–1955, Sep. 2014. doi: 10.1109/IROS.2014.6942821.
- [72] Spencer Gibb, Hung Manh La, Tuan Le, Luan Nguyen, Ryan Schmid, and Huy Pham. Nondestructive evaluation sensor fusion with autonomous robotic system for civil infrastructure inspection. *Journal of Field Robotics*, 35(6):988–1004, 2018.
- [73] Luan Van Nguyen, Spencer Gibb, Huy Xuan Pham, and Hung Manh La. A mobile robot for automated civil infrastructure inspection and evaluation. In *2018 IEEE International Symposium on Safety, Security, and Rescue Robotics (SSRR)*, pages 1–6. IEEE, 2018.
- [74] Spencer Gibb, Tuan Le, Hung Manh La, Ryan Schmid, and Tony Berendsen. A multi-functional inspection robot for civil infrastructure evaluation and maintenance. In *2017 IEEE/RSJ International Conference on Intelligent Robots and Systems (IROS)*, pages 2672–2677. IEEE, 2017.
- [75] Tuan Le, Spencer Gibb, Nhan Pham, Hung Manh La, Logan Falk, and Tony Berendsen. Autonomous robotic system using non-destructive evaluation methods for bridge deck inspection. In *2017 IEEE International Conference on Robotics and Automation (ICRA)*, pages 3672–3677. IEEE, 2017.
- [76] Ronny Salim Lim, Hung Manh La, and Weihua Sheng. A robotic crack inspection and mapping system for bridge deck maintenance. *IEEE Transactions on Automation Science and Engineering*, 11(2):367–378, 2014.

- [77] Ronny Salim Lim, Hung Manh La, Zeyong Shan, and Weihua Sheng. Developing a crack inspection robot for bridge maintenance. In *2011 IEEE International Conference on Robotics and Automation*, pages 6288–6293. IEEE, 2011.
- [78] T. Bandyopadhyay, R. Steindl, F. Talbot, N. Kottege, R. Dungavell, B. Wood, J. Barker, K. Hoehn, and A. Elfes. Magneto: A versatile multi-limbed inspection robot. In *2018 IEEE/RSJ Inter. Conf. on Intelligent Robots and Systems (IROS)*, pages 2253–2260, Oct 2018. doi: 10.1109/IROS.2018.8593891.
- [79] Elios2. <https://www.youtube.com/watch?v=hW1Fn32JB1s/>.
- [80] Case study: Advancing bridge inspections with intel’s drone solutions, accessed on September 15, 2019. <https://www.intel.com/content/www/us/en/products/docs/drones/advancing-bridge-inspections-case-study.html>.
- [81] skydio, 2021. skyido 2, June, 2021. Available at <https://www.youtube.com/watch?v=1L8vtKaR77o>.
- [82] Birds. <https://inspire-utc.mst.edu/researchprojects/as-4/>.
- [83] Inc K&J Magnetics. Original magnet calculator. <https://www.kjmagnetics.com/>, 2019.
- [84] Coefficients of friction for steel. <https://hypertextbook.com/facts/2005/steel.shtml>.
- [85] Son Thanh Nguyen, Hai Nguyen, Son Tien Bui, Van Anh Ho, Trung Dung Ngo, and Hung Manh La. An agile bicycle-like robot for complex steel structure

- inspection. In *2022 IEEE International Conference on Robotics and Automation (ICRA)*, pages 157–163. IEEE, 2022.
- [86] Habib Ahmed, Son Thanh Nguyen, Duc La, Chuong Phuoc Le, and Hung Manh La. Multi-directional bicycle robot for bridge inspection with steel defect detection system. In *2022 IEEE/RSJ International Conference on Intelligent Robots and Systems (IROS)*. IEEE, 2022.
- [87] Iso3691. <https://www.iso.org/obp/ui/#iso:std:iso:3691:-4:ed-1:v1:en/>.
- [88] Iec60034. [https://global.ihs.com/doc\\_detail.cfm?document\\_name=IEC%2060034%2D1](https://global.ihs.com/doc_detail.cfm?document_name=IEC%2060034%2D1).
- [89] Yu Otsuki, Son Thanh Nguyen, Hung Manh La, and Yang Wang. Autonomous ultrasonic thickness measurement using a steel climbing mobile robot integrated with martlet wireless sensing. In *The 30th ASNT Research Symposium, St. Louis, MO, USA*. ASNT, 2022.